A Review of Characterization and Modelling Approaches for Sheet Metal Forming of Lightweight Metallic Materials

Yong Hou [1,†], Dongjoon Myung [1,†], Jong Kyu Park [2], Junying Min [3], Hyung-Rim Lee [1], Ali Abd El-Aty [4,*] and Myoung-Gyu Lee [1,*]

[1] Department of Materials Science and Engineering & RIAM, Seoul National University, Seoul 08826, Republic of Korea

[2] Hwashin Co. Ltd., Yeongcheon 770-280, Republic of Korea

[3] School of Mechanical Engineering, Tongji University, Shanghai 201804, China

[4] Mechanical Engineering Department, College of Engineering at Al Kharj, Prince Sattam Bin Abdulaziz University, Al Kharj 16273, Saudi Arabia

* Correspondence: aliabdelaty@snu.ac.kr (A.A.E.-A.); myounglee@snu.ac.kr (M.-G.L.)

† These authors contributed equally to this work.

Abstract: Lightweight sheet metals are attractive for aerospace and automotive applications due to their exceptional properties, such as low density and high strength. Sheet metal forming (SMF) is a key technology to manufacturing lightweight thin-walled complex-shaped components. With the development of SMF, numerical simulation and theoretical modelling are promoted to enhance the performance of new SMF technologies. Thus, it is extraordinarily valuable to present a comprehensive review of historical development in SMF followed by state-of-the-art advanced characterization and modelling approaches for lightweight metallic materials. First, the importance of lightweight materials and their relationship with SMF followed by the historical development of SMF are reviewed. Then, the progress of advanced finite element technologies for simulating metal forming with lightweight alloys is covered. The constitutive modelling of lightweight alloys with an explanation of state-of-the-art advanced characterization to identify the constitutive parameters are presented. Then, the formability of sheet metals with major influencing factors, the techniques for measuring surface strains in SMF and the experimental and modelling approaches for determining the formability limits are clarified. Finally, the review is concluded by affording discussion of the present and future trends which may be used in SMF for lightweight metallic materials.

Keywords: lightweight metallic materials; sheet metal forming; constitutive modelling; numerical simulation; formability

1. Introduction

Lightweight metallic materials such as aluminium (Al), magnesium (Mg) and titanium (Ti) alloys have gained significant attention and are at the cutting edge of research and development activities in the automotive and aerospace industries for enhancing fuel economy and thus reducing gas emissions (Figure 1) [1–10]. Therefore, it is crucial to develop new lightweight materials and propose new manufacturing processes to produce high-quality lightweight components and simultaneously fulfil safety requirements. Figure 2 and Table 1 summarize the applications of lightweight materials in the automotive industry and Figure 3 presents the applications of Al alloys in the aircraft industry.
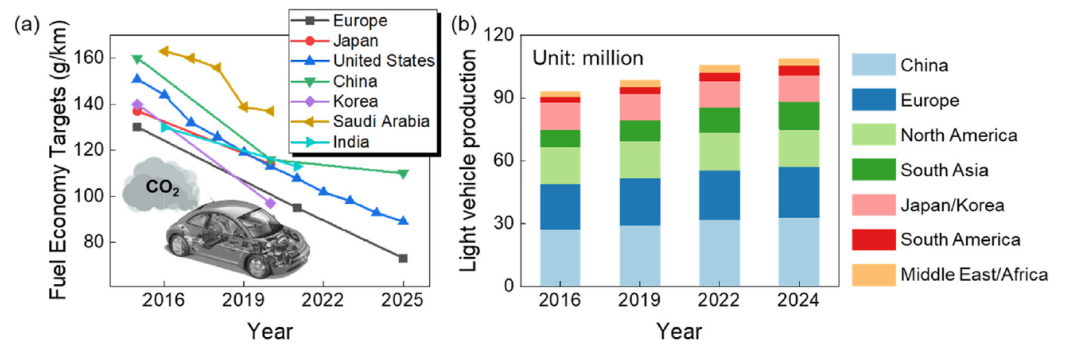
Figure 1. The current and future impact of lightweight materials in the automotive industry on (**a**) fuel economy and (**b**) production for the major markets. Reprinted from Ref. [9], open access.
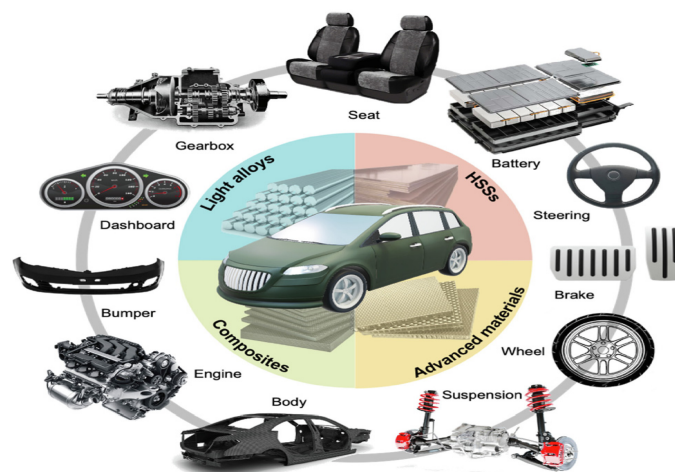
Figure 2. A schematic representation of the applications of lightweight materials in the automotive industry. Reprinted from Ref. [9], open access.


Figure 3. The application of Al alloys in aircraft. Reprinted from Ref. [10] with permission. Copyright 2018, Elsevier.

Table 1. Summary of representative lightweight materials for automobiles. Reused from Ref. [9], open access.

Lightweight Materials	Typical Components	Examples	
		Model	**Application**
Al alloys	Shock absorber, brake, piston, tank, wheel rim, fender, roof, door, bumper, heat insulator, handle, piping, steering component, conrod, rotor, suspension component, bonnet, chassis, spoke, valve, gas cylinder, seat frame.	Audi A8 Jaguar XE Mercedes AMG GT Ford F-150 Toyota GT86 Mazda MX-5 Nissan Leaf Tesla Model S	Chassis Monocoque Body Body panel Bonnet Bumper Battery case, sealing component Frame and heat exchangers
Mg alloys	Engine block, steering wheel frame, seat frame, instrument panel, wheel rim, cylinder head, clutch case, cylinder block, transmission case, lower crankcase, intake manifold, air intake system, steering link bracing, oil pump body, camshaft drive chain case, gear control housing, bracket.	Ford Thunderbird Chrysler Plymouth BMW(MINI) Lexus LS430 Mercedes Roadster 300/400/500 Lexus LS430 Chrysler Jeep Audi A8 Toyota Century Toyota 2000GT Toyota Supra Alfa Romeo GTV Porsche AG 911 Dodge Raw Volvo Motors (LCP) Honda Motor Volkswagen Passat Audi A4, A6 Porsche AG 911	Steering wheel frame SL Seat frame Instrument panel Wheel rim Cylinder head Transmission case
Ti alloys	Connecting rod, engine valve, spring, intake valve, wheel, turbocharger, exhaust system, muffler, body frame, engine rocker arm, suspension component, engine piston pin, fastener, lug nut, door penetration beam, car stop bracket, brake caliper piston, pin bolt, pressure plate, shift button, clutch circle, fuel tank, fuel cell separator.	Mercedes-Benz S-class Volkswagen Honda S2000 Roadster Porsche GT3 Toyota Altezza 6cyL Nissan Infinity Q45 Mercedes-Benz truck Mitsubishi Lancer GM Corvette Z06 Acura NSX Volkswagen Lupo FSI	Brake guide pin Sealing washer (brake) Gear shift knob Connecting rod Valve Turbocharger rotor Exhaust system Engine Suspension spring

Currently, due to the development of computing technologies, numerical simulation has gained much attention and is used widely for simulating SMF processes [11]. Many industrial sectors and research development centers have employed numerical simulations to optimize complex processes [12–14]. Numerical simulation can predict the forming forces, deformation behavior of sheet metals, sheet thickness, temperatures, stresses distributions [15–18], springback [19–22] and potential cracking and wrinkling [19,23,24], as introduced in Figure 4. Furthermore, numerical simulation has also been applied for characterizing the behaviors of materials at the microscale, which is based on crystal plasticity (CP) modelling [25–27]. CP has been used to predict microstructure evolution during material deformation [28–31] as depicted in Figure 5. Besides, the conventional numerical approach based on plasticity theory was coupled with damage models for predicting the

flow behavior of metallic materials [32] and their forming limits [33,34] under complex forming conditions.
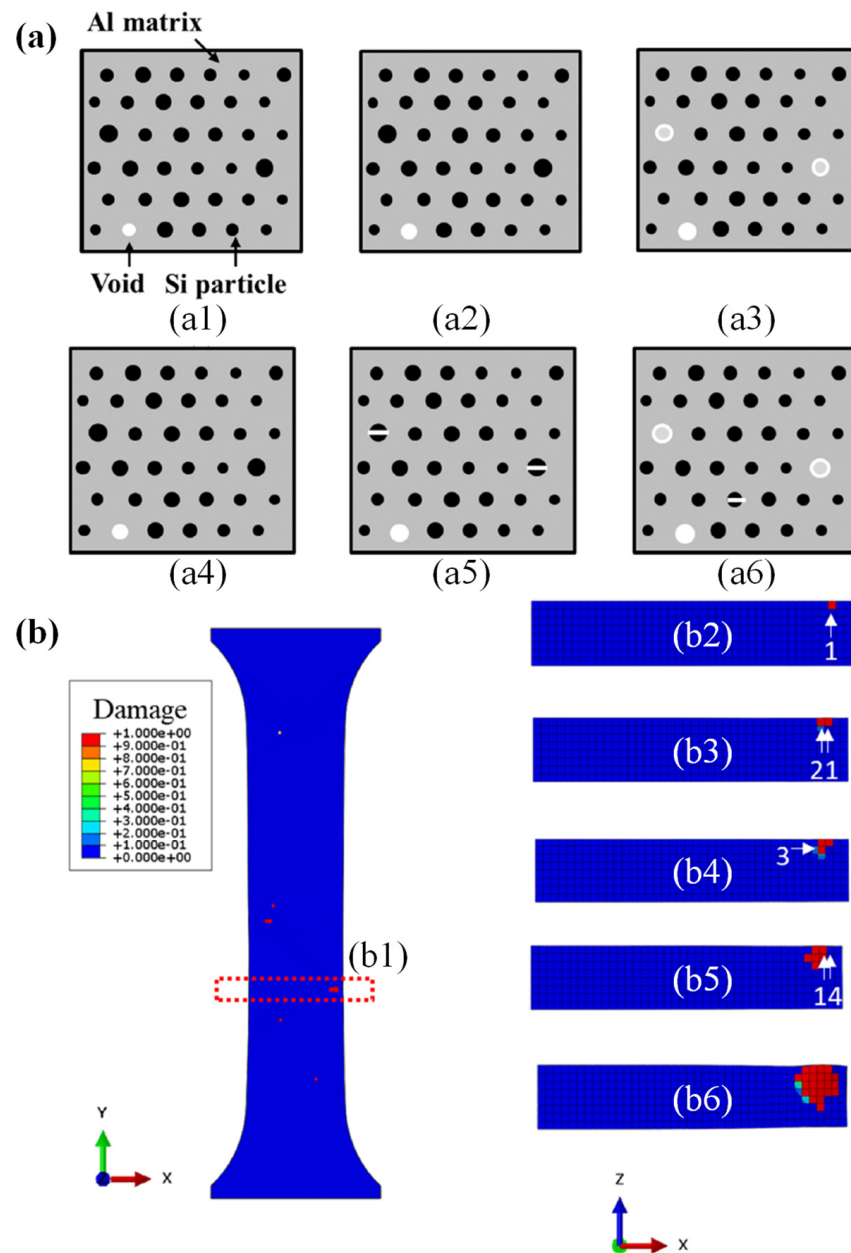
Figure 4. A schematic description of coupling numerical simulation with fracture model to predict internal cracks. (**a**) The damage evolution at the material point: (a1), (a2) and (a3) are the start of time step increment; (a4)–(a6) are the post-time steps of (a1), (a2), and (a3), respectively. (**b**) The damage value contour of simple tension simulation: (b1) shows the whole model in the X–Y plane, and (b2)–(b6) shows damage propagation in the Z–X plane through time at the red marked region in (b1). Reproduced with permission [24]. Copyright 2022, Elsevier.
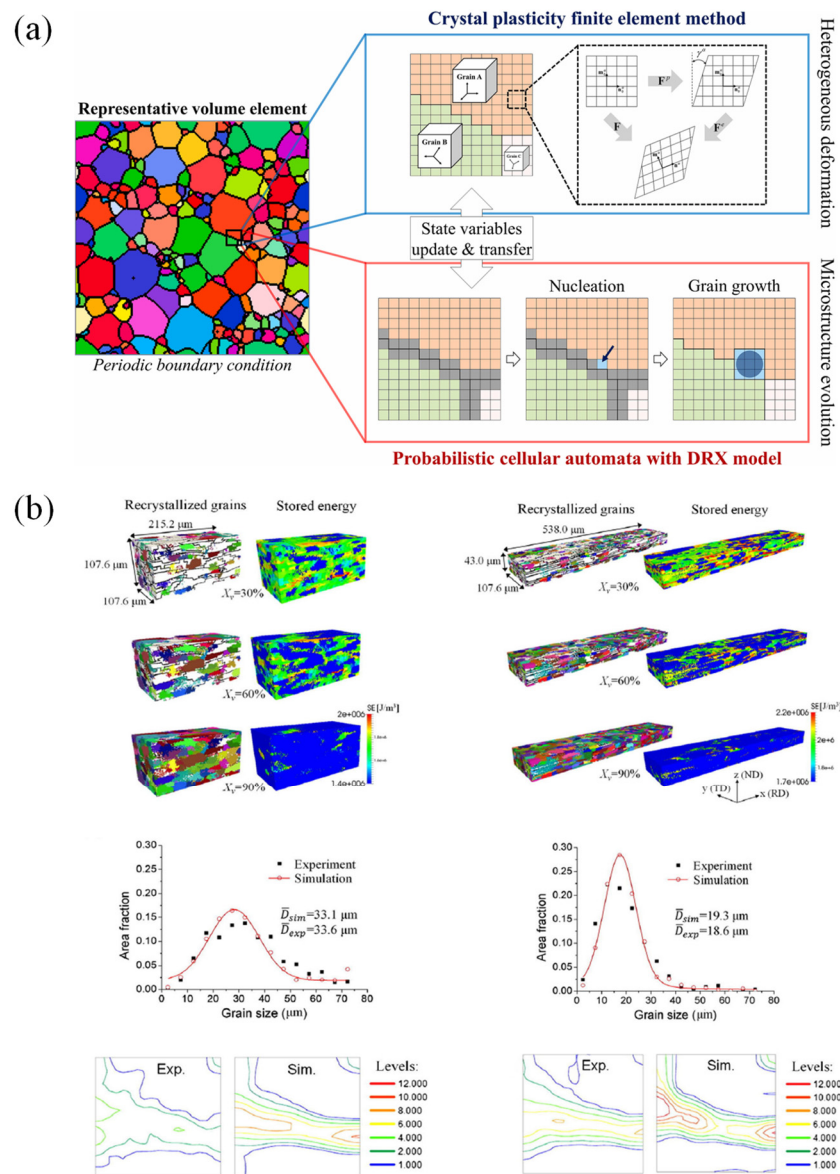
Figure 5. (**a**) A framework for the integrated CPFEM approach [31] and (**b**) an example of numerical simulations coupled with the microstructure evolution [30]. Reproduced with permission [31]. Copyright 2022, Elsevier; Reproduced with permission [30]. Copyright 2022, John Wiley and Sons.

In manufacturing automobile body components, known as body-in-white (BIW) manufacturing, SMF has been considered among the most crucial manufacturing technologies [35]. In recent years, great efforts have been made by universities and manufacturing companies to propose new SMF technologies to meet the customers' and manufacturers' requirements. In SMF processes, thin metallic sheets are stretched into the desired product shape using different tools without excessive thinning or wrinkling [36–38]. Several key factors should be considered during developing new SMF technologies, which affect the final shape and the quality of the products. Insufficient consideration of these factors will cause excessive thinning, wrinkling, buckling and tearing in the components. These factors include forming speed, temperature, friction conditions, mechanical properties of materials and the geometrical details of forming tools [39–45].

To date, various numerical simulation approaches have been developed for SMF processes. They can be classified as the discrete element method (DEM) [46,47], boundary element method (BEM) [48], finite volume method (FVM), finite difference method (FDM) [49], finite element method (FEM) including crystal plasticity finite element (CPFEM) [50–53],

extended finite element (XFEM) [54], multi-grid and mesh-free methods [55], fast Fourier transformation (FFT) [56] and arbitrary Lagrangian-Eulerian (ALE) [57,58].

Previously, many researchers have discussed the progress of SMF simulation from different aspects and there is a remarkable literature containing discussions of the importance of SMF simulations. For instance, Kaftanoglu and Tekkaya [59] briefly described a complete numerical solution for the axisymmetric deep drawing problems. Then, Makinouchi [60] introduced applications of FE simulations of SMF in several industrial sectors. He offered an outstanding literature review of existing SMF simulation codes and several examples for different industrial sectors. Makinouchi et al. [61] presented the current status and progress of SMF simulations in industries in Japan, Europe and the United States. Tekkaya [62], Tisza [63] and Wenner [64] presented developments and progress in SMF simulations in terms of methodologies, type of element and the available FE software before 2005. Ahmed et al. [65] presented the progress of SMF simulations from several points of view, such as continuum and shell approaches, material and geometrical non-linearity and frictional contact. They also discussed error estimations, error projections and adaptive mesh-refinements in SMF simulations. Banabic [66] discussed the principles of plasticity theory in SMF processes. He detailed the formability of sheet metals and presented various mathematical modelling techniques for forming limit predictions. Another important role of simulation is to quantitatively evaluate the influence of forming process parameters on the mechanical properties of formed parts through the calibrated simulation model to provide effective guidance for subsequent forming process optimization [67–69]. There have been numerous studies and reviews of SMF simulations, from fundamental plasticity theory to the optimization of FE models [31,70–72].

As described above, there has been significant progress on SMF technologies including FE simulations, but only limited literature can be found regarding a more comprehensive review of SMF technologies for lightweight metallic materials and their advanced characterization and modelling approaches. With this background, we tried to provide a review of the historical development followed by the state-of-the-art of advanced characterization and modelling approaches in the field of SMF with lightweight alloys. This review reports on the current status and future trends in experimental techniques to identify constitutive models for lightweight alloys. Theoretical and numerical models for evaluating formability are also presented along with the FE modelling approach to prove the anisotropic behavior of sheet metals [73] (Figure 6).
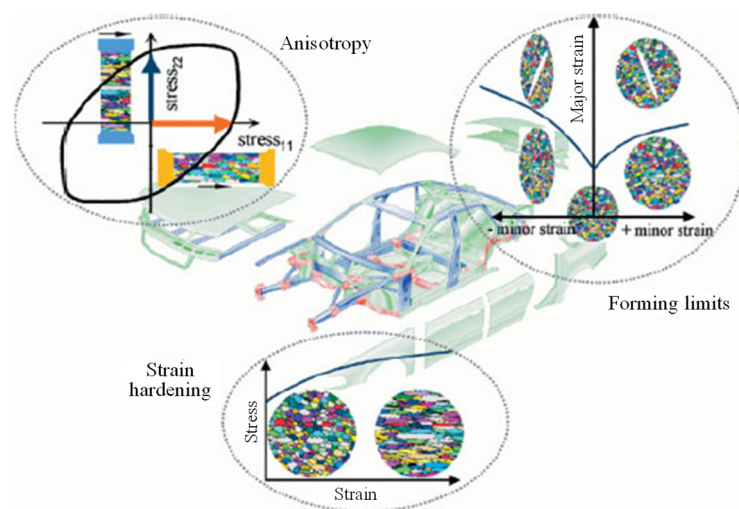
Figure 6. A schematic diagram describing the materials input date used for modern FE technologies to optimize SMF processes. Reprinted from Ref. [73] with permission. Copyright 2002, John Wiley and Sons.

In addition to forming single-layer metallic sheets, investigations on bilayer or multilayer sheets have also attracted much attention for several special components, such as pouch batteries. Yanagimoto et al. [74] observed the enhancement of the bending formability of type-420J2 stainless steel sheets when they are composed into a multilayer metallic sheet with type-304. Rydz et al. [75] analyzed the shaping of bimetallic Al–Cu sheets in cup drawing tests. Kim et al. [76] predicted the forming limit curve of a three-layer AA5182-O/polypropylene/AA5182-O (AA/PP/AA) sandwich sheet based on the Marciniak-Kuczynski (M-K) model and strain-rate potentials. Microstructure, texture, anisotropy, formability and mechanical properties of a layered composite (Brass/IFS/Brass) at various annealing temperatures were investigated by Bagheri et al. [77].

The content of this review paper follows the PRISMA guidelines [78], as depicted in Figure 7. As summarized in Figure 8, we begin with a brief discussion of simulation methods in SMF. Then, progress in constitutive modelling and the experimental techniques used to identify the constitutive parameters are discussed in Sections 3 and 4, respectively. Subsequently, the theoretical and numerical models used for formability evaluation are summarized in Section 5. Finally, the paper is concluded by providing discussion on advanced characterization and modelling approaches for SMF and the outlook for SMF technologies.
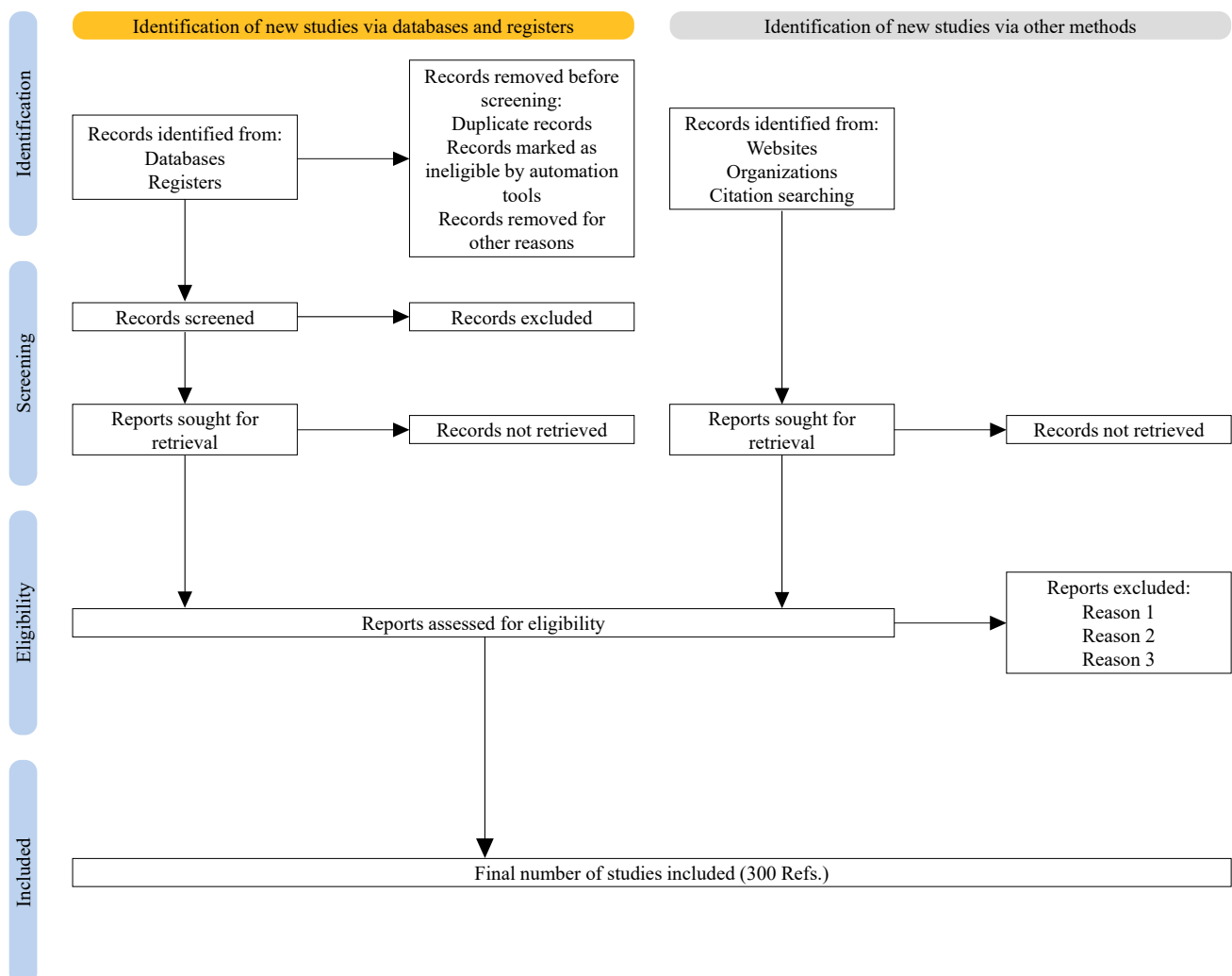
Figure 7. A schematic flowchart of PRISMA guidelines [78] used to prepare the current review.
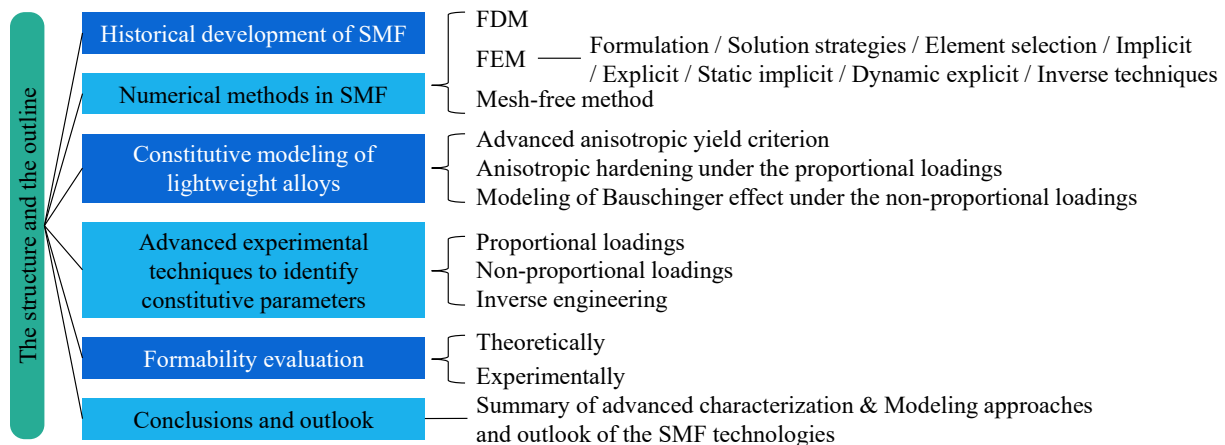
Figure 8. The structure of the current review.

2. History of Numerical Methods in Sheet Metal Forming Simulation

Early-stage simulation of SMF was restricted to two-dimensional symmetric simple problems. In the 1960s, the first simulation of the SMF process was performed by the finite difference method (FDM), simulating a two-dimensional cylindrical cup manufactured via a deep drawing process [79]. Afterwards, many trials were performed in the 1990s to use FDM for three-dimensional problems, but not very successfully because of the complexity in applying complicated boundary conditions. The FDM was utilized to simulate the thermal effect in SMF processes [80].

The finite element method (FEM) is the key method for simulating SMF processes. Wifi [81] presented a FEA of axisymmetric elastoplastic circular blank sheets for deep drawing and stretch forming processes. Then, a general formulation of FEA was proposed by Gotoh et al. [82] for deep drawing technology based on the rigid-plastic material model, where the analysis was performed by the quadratic and fourth-order yield functions. Afterwards, Wang et al. [83] proposed a general FE approach for the stamping process and the presumed small thickness of the sheet metal based on membrane theory. Besides, it is assumed that the sheet obeyed rate the independent elastic-plastic material model with the J2 flow rule. They demonstrated that both rigid-plastic and elastic-plastic material models generated similar strain distributions at the material's point unloading.

Tang et al. [84] extended the implementation of FE simulation from two-dimensional to three-dimensional via modelling deformed automotive body panels. Afterwards, Toh et al. [85] also introduced a general approach to 3D sheet metal simulation. In these simulations, either a static implicit or explicit method was utilized [64,65] with elasto-plasticity as a material model [66]. Later, deformation mechanics were introduced to DYNA3D FE software by Benson et al. [86]. Then, Belytschko [87] applied the dynamic explicit technique to FE simulation software. Massoni et al. [88] discussed the principle of replacing the draw bead with an artificial force and Wang et al. [89] considered viscous effects in their study. From the late 1990s, predicting springback accurately gained much attention from many researchers, which in turn affected the developments in sheet metal simulations to design and develop accurate, robust and efficient algorithms and solution methods.

The literature discussed several SMF simulation techniques [80–86,89–91]; for instance, Makinouchi [60,61] categorized formulations into three types, i.e., static implicit, dynamic explicit and dynamic implicit formulations. Besides, the solution frameworks were classified into incremental, one-step and large-step methods. These methods were investigated in detail by comparing different numerical algorithms [92–94]. For example, Banabic [66] categorized the simulation methods based on constitutive equations and motion description to flow method, static implicit (solid) method, rigid-plastic method, static explicit method and dynamic explicit method. The implicit method used an iterative strategy to solve linear system problems, which offered correct and unconditionally stable solutions for the simulations. Therefore, a larger time step could be used in the simulation but, because of

the iterative procedures in the solution process, this needs longer computation time and a huge memory. When a huge element's numbers are included in the deformation, it is difficult to achieve convergence. Nevertheless, the explicit technique needs less memory and computation time. Besides, it can be efficiently parallelized and convergence is easily acquired. On the other hand, this technique is stable only under certain conditions.

When extending simulation from the 2D to 3D SMF process, the shortcomings of the implicit technique were reduced by using a static explicit technique where the forward Euler scheme is used to integrate a set of equations [60–62,95–100]. Finn et al. [101] and Micari et al. [102] introduced a novel approach by coupling the advantages of both implicit and explicit techniques. In this novel framework, the explicit technique and implicit technique are used for simulating the forming process and springback, respectively.

The one-step technique was modified by applying the single time-step and the original blank sheet metals were determined from the final shapes of the deformed sheets. This is based on assumptions such as ignoring friction and neglecting the history of contact and linear strain path. This technique needs only a small computational time [103–105]. Lan et al. [12] expanded this technique for non-linear problems and Kim et al. [13] proposed a multi-step inverse approach based on it. Then, Tang et al. [14] introduced a multi-step inverse approach to simulate the stamping processes. One-step technique was accomplished by analyzing the node's position, the thickness of the initial blank and the strain distributions of the initial configurations with respect to the final configuration. The multi-step approach constantly expands the one-step technique among two consecutive steps. Azizi [106] studies the implementations of the one-step method in SMF in terms of convergence speed, type of solution and the solution time of the equations. Na and Chen [107] coupled a quasi-one-step approach with the conjugate gradient technique.

As the simulation methods progressively gained attention in industrial applications, commercial software was developed accordingly. ABAQUS (from Dassault Systèmes Simulia Corp.) and LS-DYNA (from Ansys, Inc) are the general FE software extensively used in SMF simulations. On the other hand, specialized software such as OPTRIS (from DYNAMIC SOFTWARE), PAMSTAMP (from ESI Group) and AutoForm (from AutoForm Engineering GmbH) is also broadly used [66]. In spite of the momentous development in computing power, simulation results still do not fulfil industrial requirements. Thus, further studies were performed to develop the static implicit approach in the long term because the requirement for high efficiency in industrial applications is directing further investigations to improve the static implicit method [92].

The key factors affecting the simulation results are the element type and formulation. Therefore, various element types were applied in the simulation for different SMF processes. Membrane, continuum (solid) and shell (thick/thin) elements were typically utilized in SMF simulations. Membrane elements are used when the sheet's bending radius is more than 20 times the sheet's thickness. Thus, the shell element is used in the simulation of the deep drawing process instead of the membrane element [62]. On the other hand, the shell element is a poor choice for the simulations when it is required to describe the deformation in the thickness direction [108]. Solid elements can describe through-thickness plastic deformation; therefore, they are an excellent choice to simulate blanking and hydroforming [97]. This leads to the development of 3D solid-shell and solid elements to simulate the SMF process if the deformation in the thickness direction is critical [108–110]. For deep drawing simulation, Menezes et al. [109] proposed a 3D iso-parametric element with selective reduced integration. For simulating springback, Papeleux and Ponthot [111] proposed an enhanced assumed strain (EAS) element and compared it with other elements. Furthermore, a 4-nodes tetrahedral element and an 8-node hexahedron element are also applied for simulating SMF [112–114]. Currently, Chung et al. [108] investigated the feasibility of using tetrahedron-MINI elements to simulate single and multi-layer SMF.

Along with conventional FEM, a meshless or meshfree approach was also applied in the simulation of SMF processes [115–118]. Some researchers introduced a meshless formulation for SMF simulations via an SCNI approach, which overcame the limitations of

the Galerkin-based meshless approach [119]. Besides, others expanded the SCNI approach and applied it for simulating springback [119]. Liu et al. [120] used a meshfree approach in their study for simulating hemisphere drawing and deep drawing processes. Liu and Fu [121] proposed an adaptive multi-scale meshfree approach for simulating and analyzing springback at two scales. They determined low and high components of the effective strain via the integration of the decomposed low and high scales of the shape function of RKPM to a non-linear elastoplastic formulation. When identifying the high-strain areas, a suitable scheme of node refinement was applied to calculate the stress correctly, therefore predicting the springback. Then, they compared their experimental results with the results acquired from FEM, meshfree approach and adaptive meshfree approach and noticed that the adaptive meshfree approach's results were very close to the experiment results. Liu et al. [120] applied a high gradient indicator to RKPM based on adaptive multiscale meshfree approach to simulate the deep drawing process with a high accuracy.

3. Constitutive Modelling of Lightweight Alloys

The constitutive model is the theoretical basis to describe the plastic deformation of lightweight sheet metals. The objective of this section is not to review all the existing constitutive models, but to provide an overview of recent advances regarding advanced yield criteria, flow rule and hardening law.

3.1. Advanced Anisotropic Yield Criterion

The phenomenological yield criterion provides an efficient way to describe yield behavior. Lightweight alloys show obvious plastic anisotropy, which was modelled by various anisotropic yield criteria [122–124]. The yield criteria can be divided into two categories (as shown in Figure 9). One is the yield criterion under the framework of the associated flow rule (AFR), where the yield function ($\overline{\sigma}_y$) and the plastic potential function ($\overline{\sigma}_p$) are identical, with the same parameters. The other type is the yield criterion under the non-associated flow rule (NAFR), where the yield function and the plastic potential function are two independent functions used to describe the yield stresses and the flow direction, respectively.
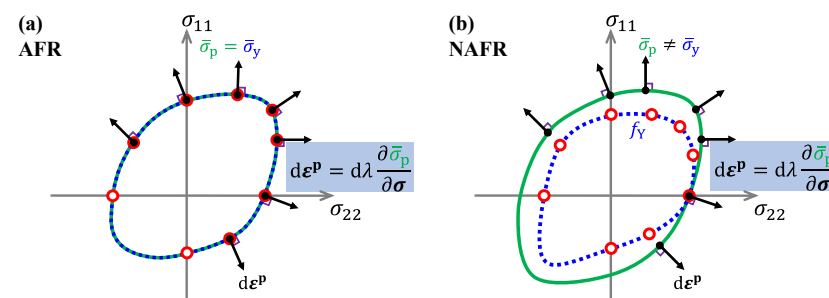
Figure 9. Constitutive model of plastic deformation under (**a**) AFR and (**b**) NAFR.

Most anisotropic plasticity models were developed based on AFR. Anisotropy parameters were introduced in the isotropic yield function to account for the plastic anisotropy. Hill [122] proposed a quadratic anisotropic yield function in 1948 based on the Mises yield criterion, which became one of the industry's most widely used yield functions to describe anisotropic yielding behavior. Barlat and Lian [125] modified the isotropic Hosford 1972 yield function to account for in-plane anisotropy. Gotoh [126] proposed a fourth-order polynomial anisotropic yield criterion; other researchers also developed different polynomial equations to describe the yield surface of metallic materials [127–129]. However, identifying the material parameters of the polynomial yield function and the proof of the convexity of the yield surface are complicated. Therefore, a classical method using the linear transformation of the Cauchy stress tensor was developed to extend the isotropic yield function to the anisotropic yield function [123,130–132]. This method of linear trans-

formation of the stress tensor can effectively improve the flexibility of the yield function and efficiently ensure convexity. The well-known 8-parameter Yld2k-2d model [123] is based on the AFR framework to capture the yield stress and strain rate ratio (r-values) by a linear combination of two functions based on a linear transformation. Cazacu and Barlat [133] proposed a representative theoretical framework for the second and third stress invariants. Based on the above-mentioned stress tensor linear transformation and representative theoretical framework, researchers have developed different advanced anisotropic yield criteria [134–136].

The anisotropic yield criteria mentioned above have been mostly used for sheet metals with body-centered cubic and face-centered cubic structures, such as high-strength steels or aluminium alloys. However, hexagonal close-packed (HCP) metals, such as magnesium alloys and titanium alloys, show obvious tension-compression asymmetry (TCA), i.e., strength differential (SD) effect under small plastic strain [137,138]. In addition, recent studies have found that third-generation advanced high-strength steels (AHSS) such as Q&P steels exhibit significant SD effect [21,139,140]. The above symmetric yield criterion cannot be used to describe the SD effect of special lightweight alloys. Several macroscopic yield criteria were developed to consider the SD effect, which is used in the SMF process to gain an accurate simulation for HCP metals. Cazacu and Barlat [141] proposed a new yield function to describe the SD effect of HCP metals. Cazacu et al. [142] developed an anisotropic asymmetric CPB2006 yield criterion using a linear transformation method for materials which is insensitive to hydrostatic stress. Khan et al. [143] proposed an asymmetric yield function related to the temperature and strain rate of Ti-6Al-4V alloy to describe the thermodynamic properties of Ti-6Al-4V in compression and tension loading. Yoon et al. [144] introduced the first stress tensor invariant to the asymmetric CB2004 yield function and proposed a stress-invariant-based yield criterion for pressure-sensitive metals. Hu et al. [145] linearly combined the cubic polynomial of the normalized third invariant and the stress triaxiality to improve the yield criterion in describing the SD effect with high flexibility.

Although the advanced yield functions under AFR can describe the yield behavior of metals and improve the accuracy of the finite element simulation, the forms of these functions become more complex, resulting in complicated parameter identification and high computing costs. To predict the yield stress and plastic flow of lightweight alloys with strong anisotropy, another approach is to use NAFR. Over the past decade, researchers generally believe that NAFR provides simple and efficient modelling to capture the anisotropic yielding and plastic flow of metallic materials. The model is formulated with a separate yield function and plastic potential function, both of which have a simpler function and convenient (analytical) parameter calibration. Stoughton [146] proposed a non-associative flow model based on the Hill48 function. With explicit parameter calibration, the Stoughton2002 model could accurately predict the uniaxial and biaxial yield stress with strong anisotropy. Later, plasticity models under NAFR were widely developed [147–153], as shown in Table 2, considering the non-quadratic feature and SD effect. The number of investigations and applications of NAFR is gradually increasing.

Table 2. The advanced NAFR constitutive models.

Reference	Non-Quadratic	SD Effect	Analytical Calibration
Stoughton (& Yoon) [146,148]	×	×	√
Stoughton & Yoon [147]	×	√	√
Min et al. [149]	√	×	√
Lee et al. [150]	√	×	√
Chen et al. [154]	√	×	√
Park et al. [151]	√	√	√
Hou et al. [155]	√	√	√
Hu et al. [156]	√	√	√
Lou et al. [153]	√	√	√

3.2. Anisotropic Hardening under Proportional Loadings

Due to the various hardening mechanisms, experiments show that hardening behaviors are stress-state-dependent and loading-orientation-dependent even under the proportional loadings [137,148,149,154]. These evolving yield surfaces cannot be captured by the anisotropic yield functions with isotropic hardening. Anisotropic hardening models can be divided into three groups. The first group captures the evolving yield surfaces at discrete levels of plastic deformation with an interpolation method. Hill and Hutchinson [157] studied the anisotropic hardening of the yield equation and the distortion of the yield surface. Aretz [158] established an anisotropic hardening model based on the variation of anisotropic coefficients with discrete equivalent plastic strain. The Yld2k-2d yield criterion was transformed to consider the anisotropic hardening by Wang et al. [159] and Cai et al. [160] using different evolving functions of equivalent plastic strain. The second approach to account for anisotropic hardening relies on introducing an evolving fourth-order tensor to modify the equivalent stress [161], or fourth-order tensors to the hardening function [162]. The third group of anisotropic hardening models was based on an analytical determination of anisotropic parameters without interpolation at discrete levels of plastic deformation. Stoughton and Yoon [148] proposed this kind of NAFR plasticity model based on the Hill48 quadratic function to capture anisotropic hardening, where four stress–strain curves in the different directions, $0°$, $45°$, $90°$ to RD and equi-biaxial tension were explicitly integrated into the yield criterion to describe the continuous change in anisotropy. Min et al. [149], Lee et al. [150] and Chen et al. [154] advanced this constitutive model scheme to obtain good agreement with measured data with a non-quadratic feature. Park et al. [151] and Hou et al. [155] further developed the CQN (coupled quadratic and non-quadratic) framework [150] to account for the SD effect. The pressure-sensitive function in Hou et al. [140,155,163] can directly employ the strain hardening curves along $0°$, $45°$, $90°$ to RD under uniaxial tension (UT) and compression (UC) and the equi-biaxial tension (EBT) condition. For the general yield criterion developed by Yoon et al. [144], the optimization method was used to determine the corresponding parameters. Hu et al. [156] proposed an analytical yield criterion based on Yoon's yield function in 2014 [144] to describe anisotropy/asymmetry-induced distorted yield surface during deformation under proportional loadings. Most recently, Hou et al. [152] proposed a NAFR plasticity model with fourth-order polynomial functions (NAFR-Poly4) to accurately predict the anisotropic evolution of yield surfaces in sheet metals under plane strain loading. The current model accounts for the anisotropic yield stress under near-plane strain (NPS) states in the calibration step with an analytical parameter identification.

### 3.3. Modelling of the Bauschinger Effect under Non-Proportional Loadings

The Bauschinger effect refers to a material property of stress/strain characteristics under the non-proportional loadings, i.e., strain path changes (SPCs) due to microscopic activities. Studies show that sheet metals exhibit special hardening behavior, including the Bauschinger effect (early re-yielding), transient strain hardening and permanent softening under SPCs, as shown in Figure 10. This hardening behavior complicates the mechanical analysis of the forming process of lightweight alloys. To simplify the problem, the mechanical analysis of simple parts with traditional materials usually does not consider the Bauschinger effect-related hardening behaviors. However, the special hardening behaviour should be considered for the advance lightweight alloys under SPCs such as loading-unloading-reloading. Besides, numerous studies show that springback can be considerably affected by hardening behavior after reverse loading [164] or other complex strain paths [165]; thus, the Bauschinger effect-related hardening behaviors are required for springback simulations as one of the important factors.
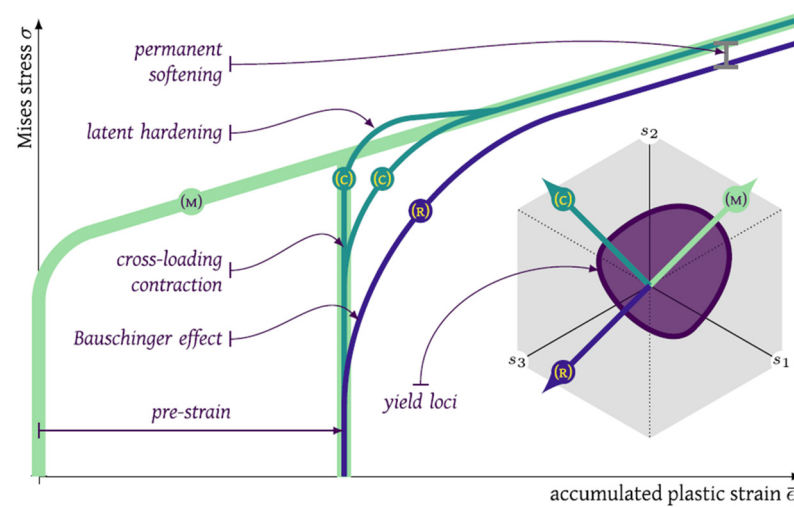
Figure 10. Graphical summary of the non-linear strain path effects: (M) monotonic represents no strain path change; (C) cross-loading is an orthogonal change of strain path in the deviatoric stress space; (R) reverse loading is an inversion of the reference direction. Reprinted from Ref. [166] with permission. Copyright 2022, Elsevier.

Prager [167] proposed the earliest kinematic hardening model by introducing the concept of back stress to translate the yield surface to capture asymmetric plastic behavior. Armstrong and Frederick [168] proposed a kinematic hardening model for nonlinear back stress evolution and Chaboche [169] proposed a general nonlinear kinematic hardening model. Using this principle, researchers studied the kinematic hardening model of multi-yield surfaces. The most widely used two-yield surface model is the Yoshida-Uemori model [170], which can describe both hardening stagnation and elastic modulus degradation. Chaboche [171] reviewed nonlinear kinematic hardening models that have been used to accurately describe plastic mechanical behavior during reverse or cyclic loading. Many studies applied typical nonlinear kinematic hardening models to loading conditions involving arbitrary SPCs [172–175].

Another theoretical modelling approach to describe the Bauschinger effect related hardening behaviour during SPCs is the distortional hardening model proposed by Barlat et al. [176–179], namely the HAH model (Homogeneous yield function-based Anisotropic Hardening). This modelling method of distortion hardening rather than kinematic hardening (with back stress) is a viable option for describing the Bauschinger effect and other transient hardening phenomena. It introduced state variables such as microstructure deviators to record loading history [166]. Compared with the kinematic hardening model, the advantage of the HAH model is that the expression and parameter calibration of the isotropic and anisotropic hardening terms are independent of each other. The HAH model can be referred to as a framework because it can be used for any isotropic or anisotropic yield condition suitable for isotropic hardening and distorts the corresponding yield surface shape depending on the loading conditions. The HAH model can capture the measured Bauschinger effect with a fluctuating term in the cyclic loading path [180,181]. Figure 11 shows the schematic diagrams of the kinematic hardening model and the distortion hardening model: (1) In the kinematic hardening model, the center of the yield surface is translated in the stress space according to the loading path and the size of the yield surface is fixed or determined by the isotropic hardening equation; (2) in the distortion hardening model, the yield surface expands in the loading direction, while the contraction occurs in the opposite direction of the load path to capture the early yielding behavior and subsequent special hardening behavior.
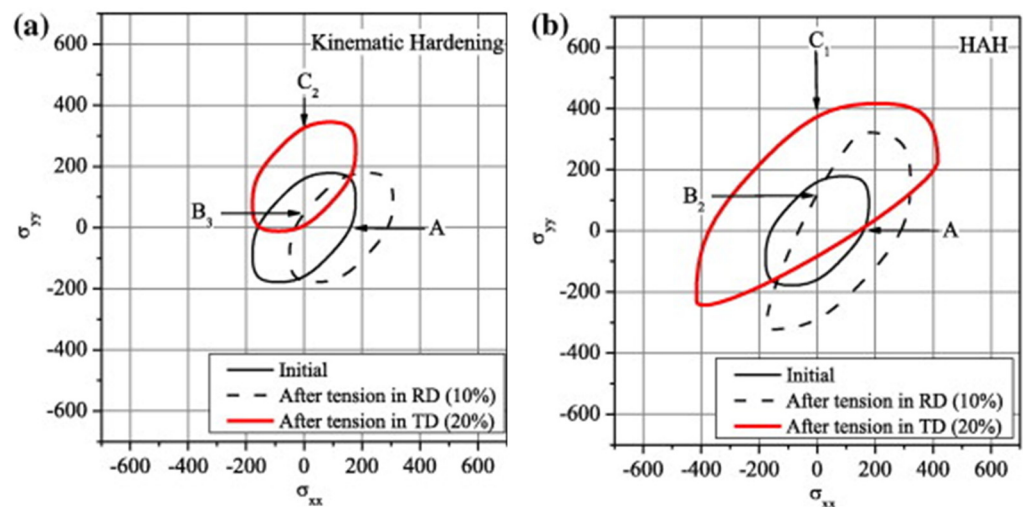
Figure 11. Yield loci during tension (up to 10% strain) followed by orthogonal tension (up to 20% strain) with (**a**) kinematic hardening and (**b**) HAH model. Reprinted from Ref. [182] with permission. Copyright 2012, Elsevier.

HAH models have been continuously developed since initially proposed. They can better describe the evolution behavior of the yield surface under a wide range of SPCs [177–179,183,184]. The original HAH model (HAH2011) can only consider forward and reverse loading, such as tension-compression or shear-reverse shear [176]. Barlat et al. [177] extended the HAH model to account for the latent hardening during cross-loading, which accurately described the stress overshoot phenomenon of EDDQ steel in two-step UT tests. Lee et al. [185] combined the HAH2011 model and the QPE model: the HAH2011 model was utilized to capture complex plastic flow behavior, such as the Bauschinger effect, transient behavior, work hardening stagnation and permanent softening, while the QPE model reproduced unloading and nonlinear elastic behavior. Barlat et al. [178] enhanced the HAH model and this version improved the theoretical framework for the evolution of microstructure deviator and the distortion effects during cross-loading. He et al. [186] modified HAH2011 and introduced more parameters to describe the Bauschinger effect of the material in two-step UT tests. Lee et al. [187] proposed a modified distortional hardening model (HAH) that improved the description of differential permanent softening under various SPCs. Barlat et al. [179] developed the HAH model into the HAH2020 version, which incorporates the effect of hydrostatic pressure, manifesting as higher flow stress in UC than in UT. Compared to previous HAH models, the state variable evolution has been revised to improve the description of the material response when SPCs occur under pure cross-loading conditions. Reyne et al. [166] presented a new HAH-based framework, i.e., HEXAH, using an arbitrary number of microstructure deviators to describe a smooth evolution from one set of activated slip systems to another under abrupt SPCs.

In addition, some scholars proposed a hardening model that combines kinematic hardening and distortion hardening to describe the material response under SPCs. Francois [188] used distortion stress instead of Cauchy stress in the Mises yield criterion, which depends on two parameters, the back stress tensor and the scalar material constant. Feigenbaum and Dafalias [189], Rokhgireh et al. [190] and Qin et al. [191] proposed different approaches to achieve the combination of back stress (kinematic hardening) and distortion hardening. Holmedal [192] established a model that distorts the yield surface by flattening it in the opposite direction of loading. The model applies a pair of back stress tensors similar to the kinematic hardening model. Table 3 summarizes the constitutive models proposed to capture the Bauschinger effect under SPCs in terms of the adopted modelling strategies.

**Table 3.** Constitutive models to capture the Bauschinger effect under SPCs.

Modelling Strategy	Back Stress	Change of Yield Surface Shape	References
Kinematic hardening	$\sqrt{}$	$\times$	[167–170,172–175,193]
Distortional hardening	$\times$	$\sqrt{}$	[166,176–181,183,184,186,187,194]
Combined hardening	$\sqrt{}$	$\sqrt{}$	[188–192,195–198]

3.4. Application of Crystal Plasticity for Constitutive Modelling

As an advanced multi-scale modelling solution, CP is used to model the deformation behaviour of polycrystalline materials through the process of slip, twinning and phase transformation. The underlying crystal-level physical mechanisms, e.g., texture evolution and micromechanical field distribution, can be captured by CP models in addition to the macroscale stress–strain response. Wang and Wen [199] stated that CP models with high prediction capability are required for modern industry. The two widely used formulations of CP are: (1) that based on the FEM known as the crystal plasticity finite element method (CPFEM) [200] and (2) the spectral formulation, which is more computationally efficient based on the fast Fourier transform, but is for small strain formulation [201]. Figure 12 shows the various conceptual ingredients with different deformation mechanisms, phases, orientations and homogenization schemes that can be assigned to the same integration point in the DAMASK (Düsseldorf Advanced Material Simulation Kit) framework to provide the constitutive response at the mesoscale and predict plastic deformation at the component level [202]. Han et al. [203] developed an approach using CP-spectral based virtual experiments to update advanced anisotropic yield functions to realize a multi-scale model for formation of a of a 2090-T3 aluminium alloy sheet. Texture evolution at different positions of the cup was quite different, as shown in Figure 13.
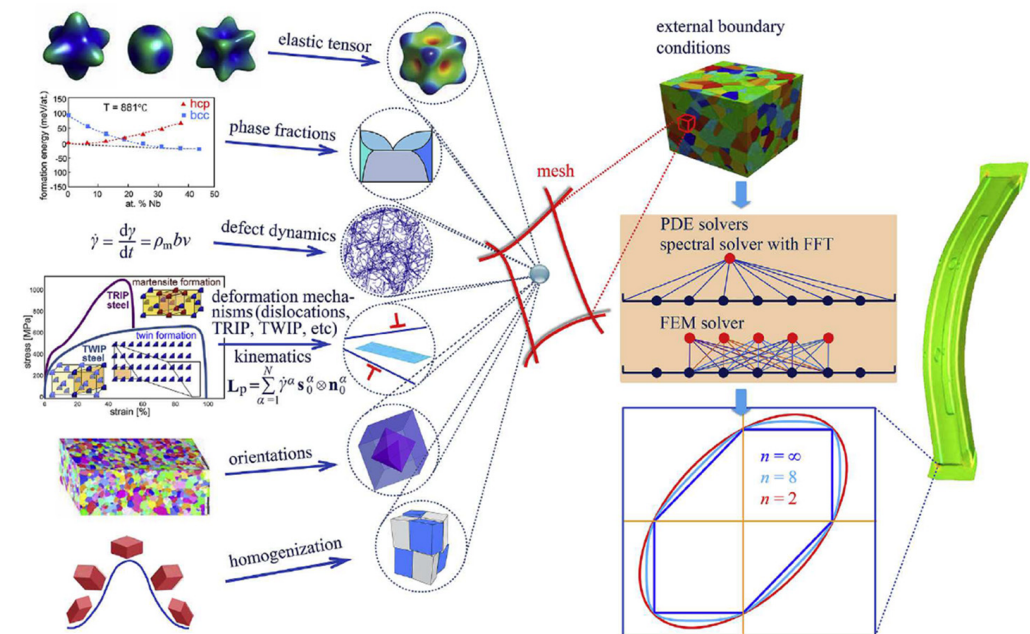

Figure 12. Yield surface calculated by DAMASK, a multi-scale and multi-physics CP modelling framework. Reprinted from Ref. [202] with permission. Copyright 2016, Elsevier.
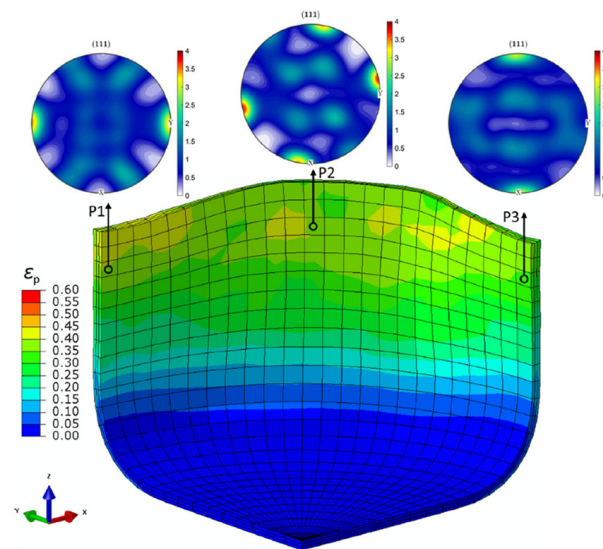
Figure 13. Equivalent plastic strain distribution and textures at three cup positions simulated with the evolving Yld2004-18p yield function calibrated from the CP model. Reprinted from Ref. [203] with permission. Copyright 2020, Elsevier.

Several advanced CP models were proposed to describe the constitutive behavior of magnesium alloy sheets (as HCP crystals) considering plastic anisotropy induced by the texture and the critical resolve shear stress (CRSS) ratio between available slip/twin systems [204–207]. Qiao et al. [208] proposed a simple empirical equation to model the twinning kinematics of magnesium alloy sheets. Recently, Shi et al. [137] reviewed the physics-based mesoscale modelling for the anisotropy of magnesium alloys. The mechanical responses of magnesium alloy sheets under different loading conditions, e.g., strain path changes [209–212], various strain rates [213–215] and elevated temperatures [216,217], were investigated by using CP models.

CPFEM were employed to provide yield stresses and plastic strain rates under various loading conditions to identify the parameters of advanced yield functions, which were implemented in FE models to achieve accurate metal forming simulations of lightweight aluminium alloys [218,219]. In order to predict the effect of microstructure evolutions on the mechanical properties of aluminium alloys during the thermo-mechanical process, Chen et al. [220] proposed an integrated CP-continuous dynamic recrystallization (CDRX) framework, as illustrated in Figure 14. Recently, the modelling approaches of DRX for aluminium alloys during hot working were further developed [221,222].
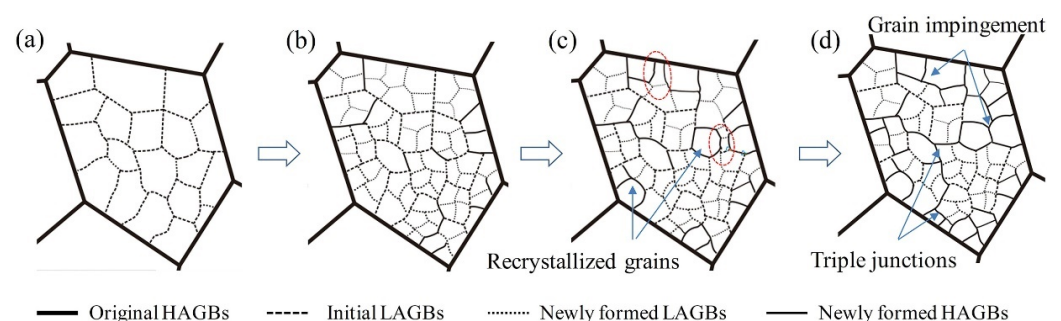
Figure 14. The proposed CDRX modelling approach by Chen et al. [220]: (**a**) initial microstructure before deformation; (**b**) microstructure change in the initial strain stage; (**c**) generation of recrystallized grains; (**d**) immobilization of recrystallized grain boundaries. Reprinted from Ref. [220] with permission. Copyright 2020, Elsevier.

CP models were utilized to investigate the microstructure evolution of advanced high-strength steels [223–227]. The strain-induced martensite phase transformation is the key feature of the third-generation advanced high-strength steels (3GAHSS). Accurate microstructural modelling of phase transformation (from retained austinite to martensite) by CP is critical to exploit new QP steels for automotive light-weighting [228–232]. Recently, a thermodynamically consistent constitutive model based on rate-dependent CP was developed to predict the stress, temperature and retained austenite evolution responses of a QP3Mn alloy over a wide range of strain rates and temperatures [232], where plastic slip and transformation kinetics laws were proposed to account for the temperature, strain and orientation-dependent mechanical behavior. Nowadays, the application of CP models in predicting the constitutive behaviors of lightweight alloys under complex loading conditions has drawn significant attention [233–237]. As shown in Figure 15, Bong et al. [238] proposed a CP approach based on a three-component dislocation density model as a virtual experimental model to accurately predict the non-proportional anisotropic hardening behavior of ultra-thin sheet metals. The validated model can predict the stress-strain curves under tension-compression loading, which are difficult to measure by mechanical experiments due to premature buckling for ultra-thin sheet metals.
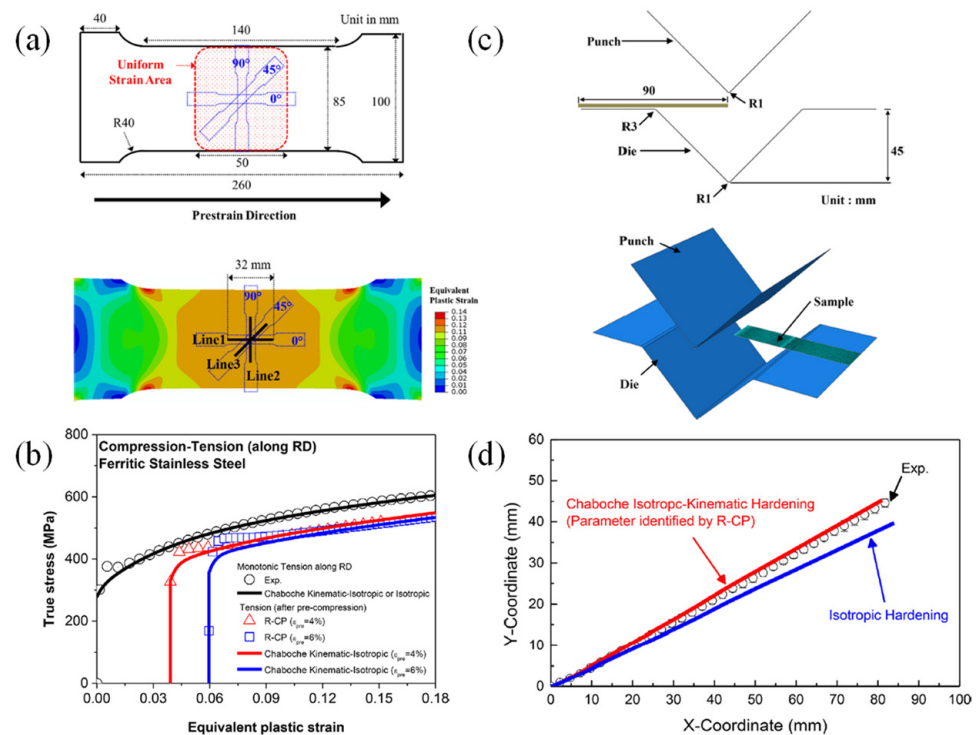

Figure 15. A CP approach based on a three-component dislocation density model to predict non-proportional anisotropic hardening behavior of ultra-thin sheet metals: (**a**) dimension of large specimen for the prior tension, ASTM E8 sub-size specimens for the second tension, and simulated equivalent plastic strain map after 25 mm tension; (**b**) CP predicted stress-strain curves of 0.1 mm thick ferritic stainless steel sheet during compression-tension along the rolling direction and comparison with Chaboche kinematic hardening model prediction; (**c**) dimension of V-bending test for 0.1 mm thick ferritic stainless steel sheet and FE model for V-bending test, and (**d**) comparison of springback profiles after V-bending of pre-deformed sample. Reprinted from Ref. [238] with permission. Copyright 2019, Elsevier.

4. Advanced Experimental Techniques to Identify the Constitutive Parameters

The advanced constitutive models require specific mechanical characterization methods to calibrate the parameters. A large amount of accurate and representative experimental data is an important input for the popular data-driven constitutive models [239]. The appli-

cation of digital image correlation (DIC) technique in measuring strain field improved the accuracy of characterization experiments for sheet metals. It also promoted the development of various advanced characterization techniques [240]. The key to the experimental characterization of the yield surface evolution behavior is to use experimental equipment and systems to realize the plastic deformation of sheet materials under different typical stress states (as shown in Figure 16). Typical stress states include uniaxial tension (UT), uniaxial compression (UC), plane strain (PS), equal-biaxial tension (EBT) and simple shear (SH). For thin plate materials, it is generally considered to be in a state of plane stress during the forming process. For mechanical characterization, when the specimen is loaded at different angles from the rolling direction of the sheet metals, the material anisotropy can be investigated.
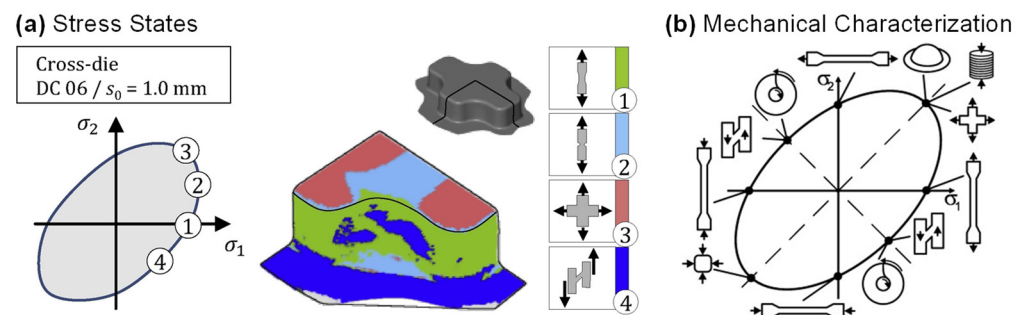
Figure 16. (**a**) Various stress states in deep drawing of a cross-cup. Reprinted from Ref. [240] with permission. Copyright 2018, Elsevier; (**b**) overview of testing methods for sheet metal characterization under different stress states. Reprinted from Ref. [241] with permission. Copyright 2014, Elsevier.

4.1. Proportional Loadings

4.1.1. Uniaxial Tension (UT)

The UT test is the simplest method for sheet metals and an international testing standard has been established [242]. The UT test combined with DIC provides a quick tool to accurately obtain the basic mechanical properties of sheet metals, such as Young's modulus, yield strength, tensile strength, uniform elongation, total elongation and r-values. These parameters work as significant engineering indicators for lightweight alloys. The stress–strain curves measured from the UT test are important data for investigating the hardening behavior of lightweight alloy sheets. Some classical constitutive models embedded in the commercial finite element software are calibrated directly using the UT experimental data to predict the forming process with acceptable accuracy. However, stress–strain curves measured from the UT test tend to over- or underestimate hardening curves under other stress states, which highly depends on the selected yield criterion. Furthermore, the obtained stress–strain curve from the UT test is limited due to the localized necking of the UT specimens. In order to obtain an accurate description of the post-necking hardening behavior, the method of curve fitting is adopted based on the chosen hardening law, e.g., Swift or Voce hardening laws.

4.1.2. Uniaxial Compression (UC)

Studies show that polycrystalline sheet metals such as magnesium and titanium alloys have obvious SD effects [243,244]. Thus, the measured stress–strain curves from the UT test cannot be used to describe the hardening behavior under UC. The thin sheet metal is prone to buckling when it is compressed, so the key to the mechanical characterization for measuring the UC stress–strain curve is the design of the anti-buckling fixture. Boger et al. [245] designed a hydraulic actuating fixture, which exerted pressure on the sample's surface along the thickness direction through two parallel movable plates. A new method was proposed to correct the influence of friction force and sheet thickness stress. The non-contact laser extensometer was used to measure the strain distribution and history of the lateral surface of the sample. Kuwabara et al. [246] designed an interdigitated comb-like

device as shown in Figure 17a to prevent the buckling of the specimen. A part of the test specimen surface was kept in normal contact with the support structure and the strain was measured using conventional strain gauges on the sample surface not supported by the comb device. Cao et al. [247] developed a wedge-shaped device to measure the stress–strain curve during compression using a geometry that ensures that the specimen is fully supported during testing. However, this design requires machining fins outside the specimen to enable strain measurements during UC loading. Hou et al. [248] measured the UC stress–strain curves of dual-phase steel sheets with a support fixture for suppressing buckling. The strain field was measured by the DIC method on one of the edge surfaces of the UC specimen (see Figure 17b). Hou et al. [249] further used this setup to determine the UC stress–strain curves of ultra-thin pure titanium bipolar plates based on a newly designed sandwich specimen. The above-mentioned UC anti-buckling fixture can be further utilized for the tension-compression cyclic loading experiment of sheet metals and realize the investigation of the Bauschinger effect, which will be detailed in Section 4.2.
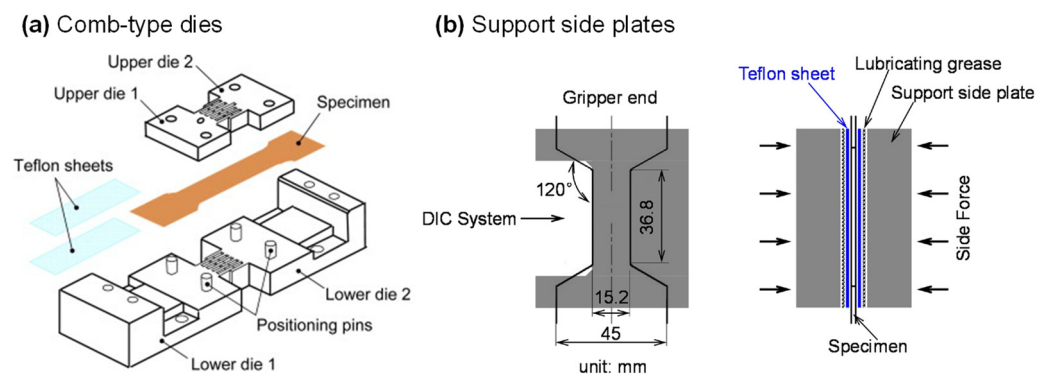
Figure 17. Experimental apparatus for UC tests of sheet metals: (**a**) configuration of the dies. Reprinted from Ref. [246] with permission. Copyright 2009, Elsevier; (**b**) the support side plates. Reprinted from Ref. [248] with permission. Copyright 2021, Elsevier.

4.1.3. Simple Shear (SH)

SH experiments are often used to calibrate material parameters in advanced constitutive models or to determine the hardening curve of materials at large plastic strains [250]. In an SH experiment, the rectangular test area deforms into a parallelogram along its length when the width is fixed. Bouvier et al. [251] studied the stress and strain distribution of SH specimens and found that the uniformity of shear bands depends on the geometries of the SH specimen. They recommend a 10:1 ratio of shear area length to height to maximize the uniform region. A standardized shear test method ASTM-B831 [252] was established stipulating the shape and size of the SH specimen. Merklein and Biasutti [253] modified the ASTM standard specimen. Moreover, double bridge SH specimens were proposed [254–256]. There are boundaries in the gauge areas of the above SH specimens, so the materials near the boundary areas are always in a stress state of UT. There will be an interference of edge effect when calculating the shear stress. In order to avoid the influence of the edge effect, Marciniak [257] realized the measurement of SH loading of the copper plate for the first time by using in-plane torsion tests. Tekkaya et al. [258] used in-plane torsion experiments to determine flow stress curves for plates with equivalent plastic strain up to 1.0. Subsequently, in-plane torsion tests were further improved to measure the flow stress, kinematic hardening and fracture limit under SH of thin sheet metals [259–261].

4.1.4. Hydraulic Bulging (HB)

Lightweight sheet metals experience complex stress states including various biaxial deformation states, such as EBT and PS. Hydraulic bulging [262–264], pneumatic bulging [265] and bulging with viscous material as medium [266] experiments are advanced characterization methods to obtain stress–strain curves and the biaxial strain ratio in a large strain range

under biaxial deformation [267]. An example of a bulge test set-up with a circular die and DIC measurement system is presented in Figure 18. The calculation method of stress–strain data in bulging experiments has undergone many years of development. Studies show that biaxial deformation in hydraulic bulging is sensitive to material anisotropy [262]. With the aid of DIC technology, Min et al. [268] proposed an accurate method for calculating stress and strain in circular hydraulic bulging experiments considering the anisotropic deformation of sheet materials. Despite some progress in the analytical measurement of stress–strain data, based on the membrane assumption, it is still necessary to use an experimental system with a ratio of die opening diameter to initial specimen thickness greater than 100 to ensure the validity of the computational method [264]. Lafilé et al. [269] proposed a new method to directly determine material behavior using DIC data on the outer surface of the specimen, which is suitable for hydraulic bulging experiments with small opening diameters of dies. A stress–strain curve close to the plane strain state can be obtained by hydraulic bulging with a reasonably designed elliptical die [270–272].
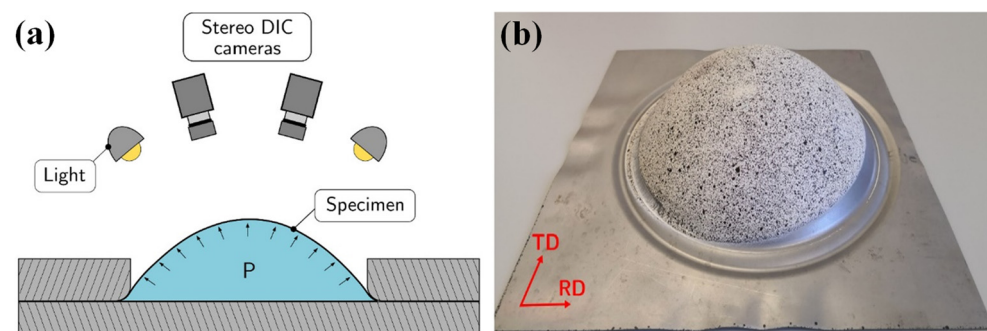
Figure 18. Hydraulic bulge test: (**a**) schematic of the experimental apparatus with DIC and (**b**) formed bulge specimen with DIC speckle pattern. Reprinted from Ref. [273], open access.

In addition, the tube expansion experiment can realize the plastic deformation of the material under various strain paths because it can control the axial tension or compression and radial bulging. Combined with the DIC method, the mechanical behavior under various strain paths can be accurately measured [274–276]. He et al. [274] developed a tube expansion testing system based on DIC feedback control, which realized the measurement of stress–strain curves in a large strain range under any biaxial loading paths in the first quadrant of the principal stress space. Tiji et al. [276] built a hydraulic bulging testing system based on finite element simulation and PID (Proportional Integral Derivative) control to achieve various linear strain paths.

The tube expansion experiment can realize the mechanical characterization of materials at large plastic deformation under various stress states. However, for sheet metals, it is necessary to prepare in advance closed tubular samples by methods such as laser welding. Sample preparation is difficult for high-strength materials and the influence of welding quality cannot be ignored. Moreover, the deformation of the specimen in the bulging experiment will be affected by the bending strain and the through-thickness stress, especially in the elastic or small plastic deformation stage. Therefore, bulging experiments are often inapplicable for advanced lightweight alloys, or accurate analytical methods are required to consider the effects of bending strain and through-thickness stress.

4.1.5. Biaxial Tensile Testing with Cruciform Specimen (BTC)

Compared with experiments such as hydraulic bulging, BTC has some outstanding advantages: no bending strain, no thickness stress and no friction effect. In addition, the stress ratio can be controlled arbitrarily by the program of the BTC testing system. Therefore, BTC is widely used to study the hardening behavior under different BT conditions and to measure the yield locus of sheet metals [277]. In recent years, one of the main topics in the research on BTC is the design of cruciform specimens. The design of a cruciform specimen

with uniform thickness mainly focuses on the geometrical design of the cruciform arms and the junction of the cruciform arms [278]. Kuwabara made outstanding contributions to the research on BTC [279–281]. The International Standards Organization established the ISO16842:2014 standard in 2014 [282]. ISO16842:2014 specifies the shape, geometric dimensions and processing method of the cruciform specimen with slits. However, when using ISO standard cruciform specimens, a challenging problem arises: the achievable plastic strain in the test area of the cruciform specimen is limited by the premature fracture of the arms of the cruciform specimen. There are two ways to increase the maximum plastic strain that can be achieved in the central region: (1) thinning the central test region; (2) strengthening the arms of the cruciform specimen. Liu et al. [283] designed a cruciform specimen with reduced thickness and a notch with a small central circular area. They conducted BT experiments combined with DIC to study the hardening behavior of AA5086 aluminium alloy under large strains. Recently, Zhang et al. [284] reviewed the development history of cruciform specimen designs, including 17 different geometries. Almost all of the above-mentioned cruciform specimens with thinned central test areas will produce fracture in the gauge area; that is, the premature fracture of the cruciform arms can be effectively avoided.

However, the thinning of the cruciform specimen in the central area generates some problems: (1) the thinning method by mechanical processing may introduce certain damage to the test material; (2) the thinning of the specimen often cannot ensure that the size and accuracy of the specimen thickness reduction in the test area meet the requirements of the sample design; (3) the thinned specimen in the central area must be suitable for determining the fracture limit of the thin-plate material. If it is used to characterize the hardening behavior of the thin-plate material, it needs to undergo analytical methods or combined with finite element simulation. The inverse process method should be used to calculate the stress–strain curves of the material under different biaxial loading conditions.

Another way to increase the maximum plastic strain achievable in the central region of the cruciform specimen is to strengthen the cruciform arms. There are several innovative ways to strengthen the outer region to increase the plastic deformation of the cruciform specimens [285–287]. The achievable plastic strain range in the gauge area of a cruciform specimen can be significantly increased using novel specimens by Hou et al. [248] with laser deposition on the arms (as shown in Figure 19) in comparison with ISO Standard specimens for three dual-phase steels with strength grades from 590 to 980 MPa. Evolving yield behavior can be experimentally measured up to large plastic strains, e.g., ~0.11 for DP590, ~0.07 for DP780 and ~0.05 for DP980.
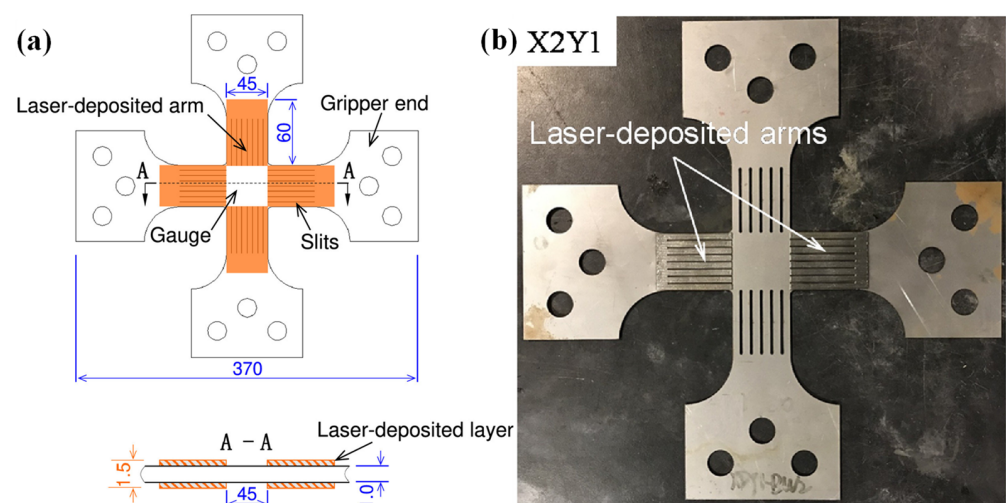
Figure 19. Cruciform specimen with arms reinforced by laser deposition: (**a**) dimensions and (**b**) a laser-deposited cruciform specimen. Reprinted from Ref. [248] with permission. Copyright 2021, Elsevier.

4.2. Non-Proportional Loadings

Sheet metals are often subjected to complex strain histories, e.g., SPCs, during stamping of automotive components, for instance, sheets undergo a bending-reverse-bending deformation process when flowing through a draw bead or die fillet. Therefore, the mechanical characterization of materials under non-proportional loadings is of great significance in studying Bauschinger effect related hardening behaviors.

4.2.1. Uniaxial Tension-Uniaxial Compression (TC)

The TC cyclic loading experiment is the most widely used experimental method to study the Bauschinger effect of sheet metals. The key to developing the mechanical characterization for measuring the hardening curve of the sheet metals under TC is the same as that of the UC tests, which require the design of the anti-buckling fixture. The measured stress–strain curves under TC loadings are used to characterize the Bauschinger effect and to calibrate and validate the kinematic or distortional hardening models [21,170,179,245,288–292].

4.2.2. Shear-Reverse Shear (SRS)

The SRS test is an important experimental method to study the Bauschinger effect under the load-reverse load state [182,185,293,294]. Bouvier et al. [251] used the optimally designed shear testing fixture to achieve uniform distribution of stress and strain in the shear region of the SH specimen and to obtain stress–strain curves under SRS by changing the direction of loading. Yin et al. [260] developed an in-plane torsion experimental system that combines shear-reverse shear loading with the DIC technique. The advantage of this experiment is that only one experimental test is performed on one sample and the determination of stress–strain curves under different pre-strains can be realized. Zou et al. [139] designed a lateral support fixture to prevent the shear specimen from buckling and measured the stress during SRS experiments of two advanced high-strength steels DP980 and QP980.

4.2.3. Bending-Reverse Bending (BRB)

The BRB test can also be used to determine the Bauschinger effect in thin sheet materials. The inner/outer layer material undergoes a compression-tension/tension-compression deformation history during the BRB test. Yoshida et al. [295] designed a cyclic bending experimental setup to perform BRB experiments on three thin sheet metals and proposed an advanced parameter optimization technique based on the measured bending moment-curvature curves. Beginning with the work of Yoshida [296], the determination of the cyclic stress–strain response from cyclic bending experiments using the inverse method has gained some popularity [296,297]. Zang et al. [298] proposed an experimental method to characterize the Bauschinger effect of materials by using the three-point bending springback test of the specimen after pre-tension deformation. For pre-tensioned specimens, the subsequent three-point bending experiment will cause the inner layer of the sheet to undergo a reverse loading of first tension and then compression, so it can be used to study the Bauschinger effect of the material. More recently, this method was adopted by Choi et al. [299] to calibrate the parameters of the HAH model for ultrathin sheet metals.

4.2.4. Non-Reverse Strain Path Changes

There are some experimental characterization methods for non-reverse SPCs. Barlat and co-workers made outstanding contributions to the characterization of the mechanical properties of large specimens with UT preloading and related research on the Bauschinger effect [300–304]. Zaman et al. [302] cut sub-size UT and cruciform specimens from the pre-deformed specimens for secondary deformation (Figure 20).
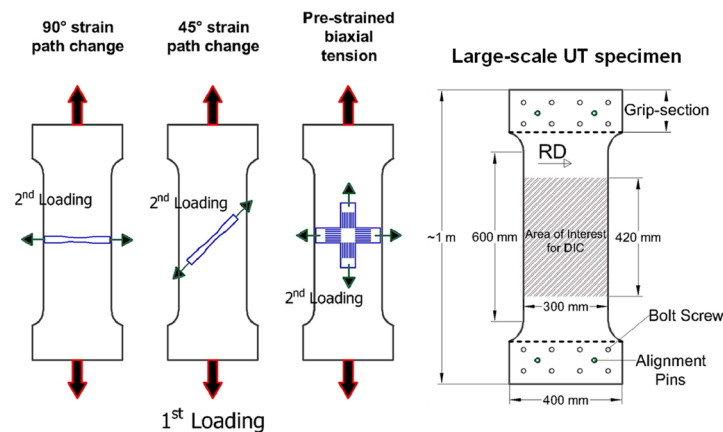
Figure 20. Schematic illustration of the selection of standard specimens from the uniform region of the large-scale specimen. Reprinted from Ref. [302] with permission. Copyright 2018, Elsevier.

Wi et al. [303] designed a smaller cruciform specimen to characterize the hardening behavior in the BT stress state. The stress–strain curves under various SPCs were measured, providing experimental data for calibrating and validating advanced constitutive models. Using the commonly-used cruciform specimens, it is difficult to measure the strain hardening curves under large plastic strains [282]. For advanced high-strength materials, only the initial yield stress could be measured and the subsequent yield surface evolution of the material could not be obtained. Recently, the complex anisotropic hardening behavior of a Q&P steel sheet with a strength of 980 MPa (QP980) subject to biaxial proportional and non-proportional loadings was investigated through advanced mechanical characterization, as shown in Figure 21. The biaxial SPCs, e.g., UT followed by PS, EBT followed by PS, UT and SH, were successfully characterized by the BT tests with arm-reinforced cruciform specimens.
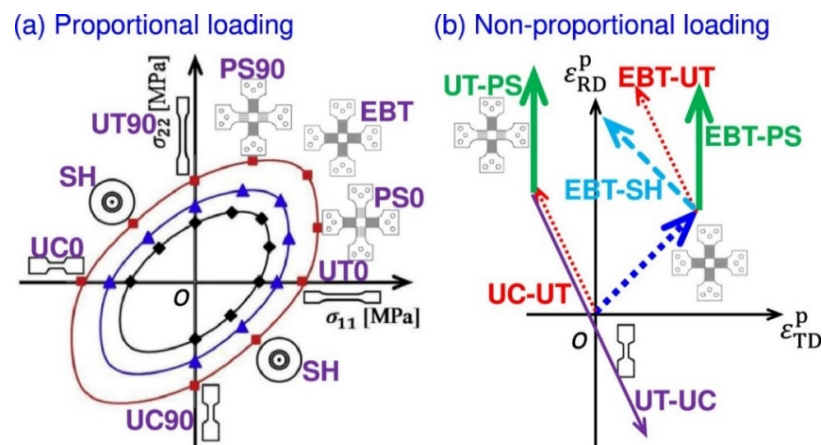
Figure 21. Mechanical characterization approaches used to investigate the evolving yield surfaces under (**a**) proportional loading and (**b**) non-proportional loading. Reprinted from Ref. [184] with permission. Copyright 2022, Elsevier.

In summary, advanced lightweight alloys exhibit complex mechanical properties, which puts forward new requirements for the advanced constitutive models and characterization methods under complex loading conditions. Complex loading conditions are mostly limited to reverse loadings such as TC, SRS and BRB. Hence, novel mechanical characterization methods under SPCs are required for the engineering application of advanced lightweight alloys.

4.3. Inverse Engineering

Advances in optical and numerical techniques have led to developing a new generation of characterization methods such as inverse engineering to understand the complex deformation behavior of materials or components. These techniques, including DIC, finite element model updating (FEMU) and virtual fields method (VFM), enable new approaches to generate more knowledge about plastic deformation behavior. Recent reviews of the research on the optimization and inverse analysis of metal forming and heterogeneous mechanical tests for the identification of material parameters can be found in Andrade-Campos et al. [305] and Pierron and Grédiac [306]. FEMU compares measurable variables to obtain the cost function: (1) local observations, such as the strains and (2) global observations, such as the load, while VFM uses a balance equation between the external and internal virtual work to determine the parameters.

As mentioned in Section 4.1, the measured stress–strain curve from the UT test is limited due to the localized necking of the specimens; hence, inverse engineering can be used to determine the post-necking responses. Approaches for obtaining stress–strain curves at large strains (or strain at post-necking process) by coupling experiments (or load-displacement curve) with finite element analysis have been developed [307,308]. Pham et al. [309] coupled the inverse finite element analysis and the curve-fitting method to identify the post-necking stress–strain curves. The high flexibility was highlighted in the selected hardening laws.

Another significant application of inverse engineering is identifying an anisotropic yield function. Lou et al. [310] identified the optimized parameters for the proposed yield function and the Swift-Voce hardening law. The numerical simulation errors were calculated for mechanical tests with the dog-bone specimen, the central hole specimen, the notched specimen and the in-plane shear specimen by comparison of predicted load-stroke curves with experiments. The downhill simplex algorithm was selected as the optimization algorithm. Zhang et al. [311] compared the analytical computation and inverse engineering approach under different stress states (simple shear, uniaxial tension, plane strain tension and equi-biaxial tension) of the AA5182-O sheet. The evaluation showed that the inverse engineering approach could effectively characterize the strain hardening curve up to large plastic strains, especially for tests with inhomogeneous deformation.

Inverse engineering with full-field measurements, e.g., VFM, is increasingly and widely employed in identifying constitutive parameters of anisotropic plasticity models. Grédiac and Pierron [312] presented the first attempt to apply VFM to identify elasto-plastic constitutive parameters, where a very simple Prandtl-Reuss law was considered. Rossi et al. [313] described an application of VFM to large-strain anisotropic plasticity. Full-field data of notched specimens could be processed with low computational times to identify the constitutive parameters of plasticity models. Recently, Kim et al. [314] proposed a new VFM based on real nodal displacements to improve the accuracy of VFM at large plastic deformation, as shown in Figure 22. Using cruciform specimen, Martins et al. [315] explored a potential test to simultaneously identify the parameters that govern an anisotropic yield criterion and a hardening law using the virtual fields. Moreover, the different complex geometries were used to enhance and further increase the robustness of the used VFM [316,317], as shown in Figure 23. A comparative study of four identification strategies based on full-field measurements was conducted by Martins et al. [318] and the results showed that VFM could be a perfect candidate for achieving a reasonable balance between the quality of the identification procedure and computational cost.
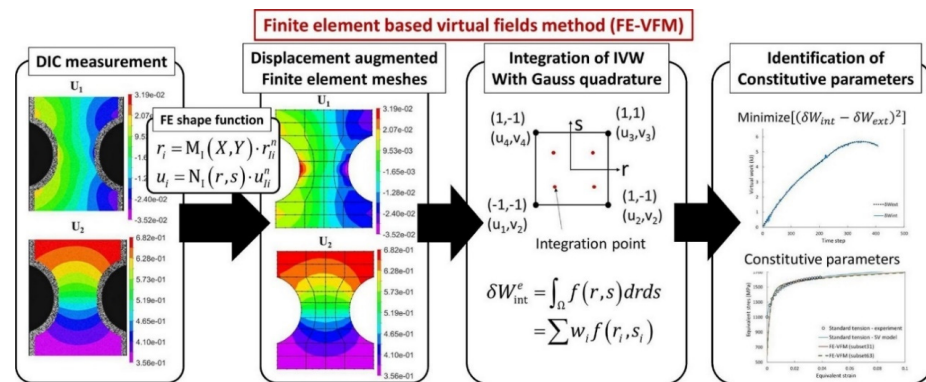
Figure 22. Finite element-based virtual fields method with pseudo-real deformation fields for identifying constitutive parameters. Reprinted from Ref. [314] with permission. Copyright 2021, Elsevier.
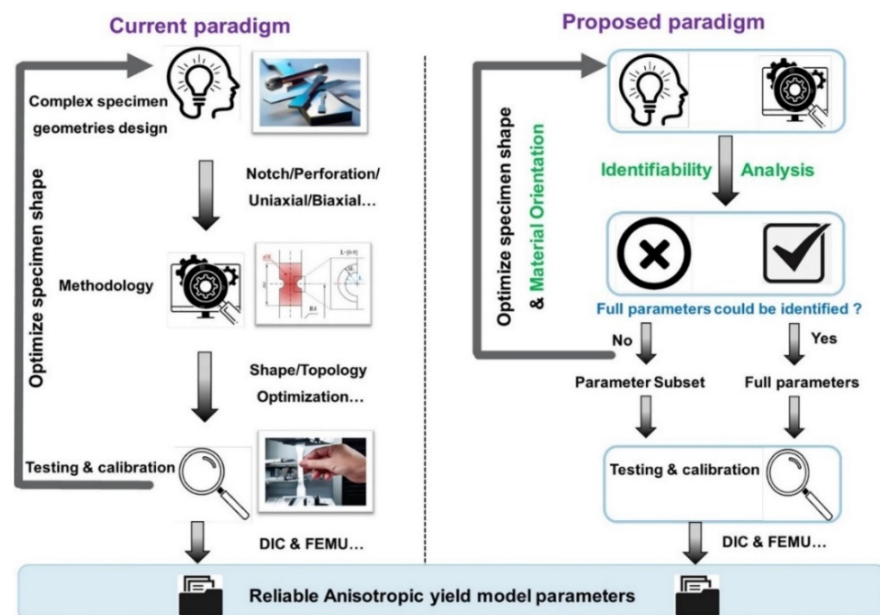

Figure 23. Comparison of current and proposed paradigm for non-conventional test design using specimens of complex geometries and parameters identification. Reprinted from Ref. [317], open access.

5. Evaluation and Modelling of Forming Limit

The formability of sheet metal is defined as its ability to resist the plastic deformation before the onset of fracture. It can be used to describe the flow and anisotropic behaviors, plastic anisotropy and the forming limit diagram/curve (FLD/FLC) which is characterized through determining two principal strains at fracture called major strain (ε_1) and minor strain (ε_2) [319]. Unveiling the formability of sheet metals is challenging because it depends on the many factors in Figure 24.
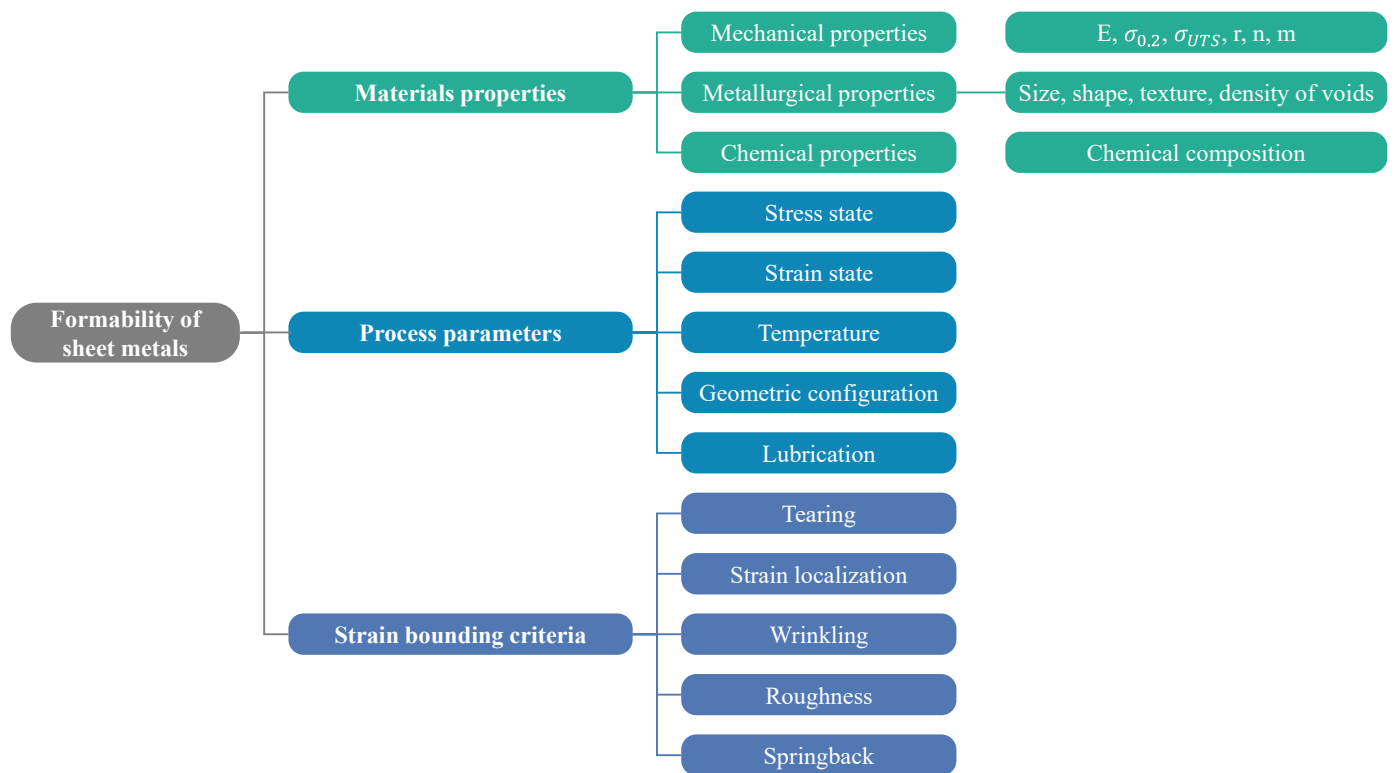
Figure 24. Factors affecting the formability of sheet metals.

FLD is considered as a critical tool used for evaluating sheet metal's formability. Keeler proposed the negative region of the minor strain of FLD, then Goodwin [320] extended this by proposing the positive region of the minor strain. Extensive and standardized experimental techniques were used to determine the FLDs of sheet metals under different forming conditions such as forming temperatures and out-of-plane (Nakajima test) and in-plane (Marciniak test) formability testing [321,322]. Furthermore, the machines used for planar-biaxial tensile testing can also be utilized for determining FLDs of sheet metals because of their ability to control strain path precisely and avoid the impact of friction [323,324]. The details of FLD are depicted in Figure 25 [325]. As depicted, FLC is the crucial feature of FLD, where it can describe the strains limit at the necking onset. FLC is defined by the plotted major strain (ε_1) and minor strain (ε_2) which were determined from the formability testing under different strain paths from uniaxial to biaxial tensions. FLC highly depends on strain rates and forming temperatures and its shape depends on the strain path. Besides, the microstructure can seriously affect the formability of lightweight materials. Zecevic et al. [326] found that the continuous-bending-under-tension process postponed the onset of necking and significantly increased the percentage elongation at failure of AA6022-T4 sheets. A similar phenomenon regarding formability enhancement was also reported in other lightweight metallic materials [327–329], where the underlying mechanisms behind the enhancement of formability were discussed in detail. Regarding the formability of lightweight sheet metals, the regions under and above the FLC describe the safe forming and instability or necking regions, respectively [330,331].
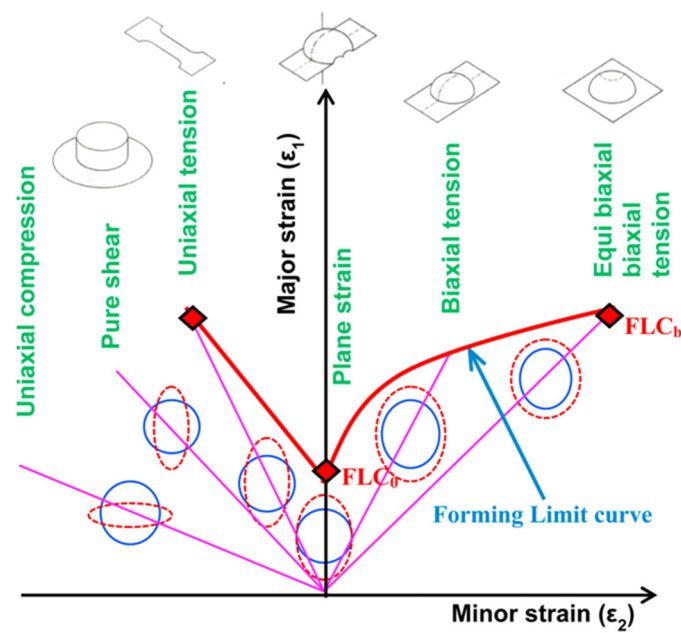
Figure 25. A schematic description of FLD and other failure limits. Reprinted from Ref. [325] with permission. Copyright 2016, Elsevier.

The main issue of a determined FLD is its validity only for a process where the straining path is linear and the loading is proportional [332]. Since strain paths are commonly not linear in the multistage forming processes, the influence of the non-proportional strain paths restricts the adequacy of the FLDs for evaluating the formability of sheet metal. To address this issue, Kleemola and Pelkkikangas [333] and Arrioux et al. [334] offered FLSD, which does not depend on strain paths. The FLCs of the FLSD cannot be determined straightforwardly from experimentation, but they are represented through major principal stress and minor principal stress as coordinates. Thus, Stoughton and Yoon [335] proposed a new model-based on Hill's yield criterion and hardening law to transfer the FLDs of metallic materials into FLSDs, as shown in Figure 26.
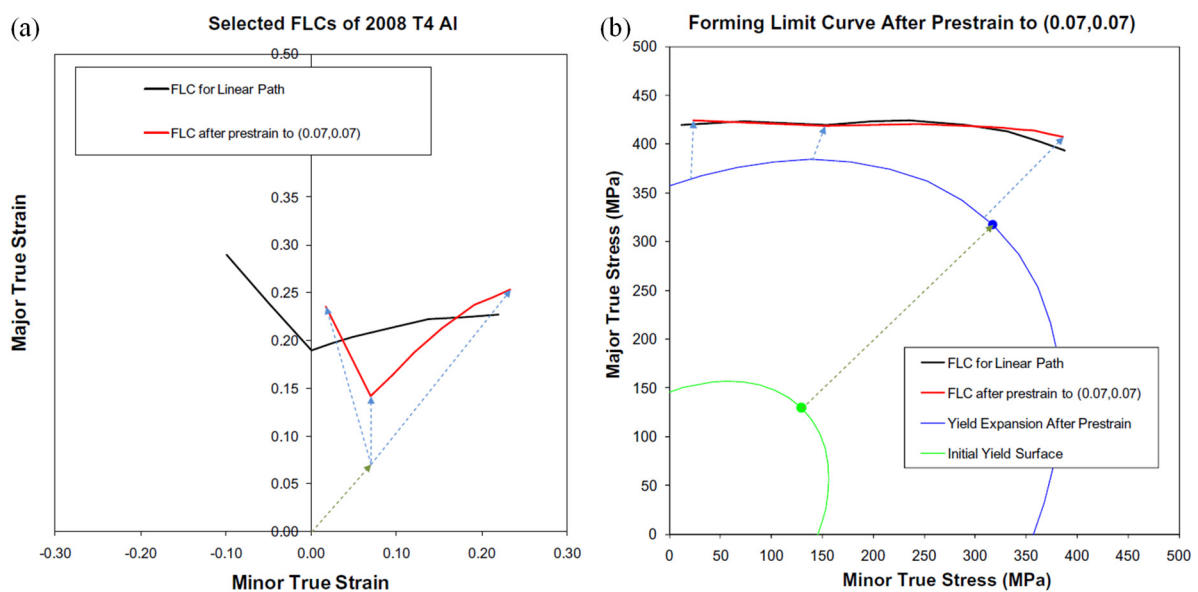
Figure 26. The transformation from an FLD to an FLSD. (**a**) FLD which contains two FLCs including one FLC with pre-strain; (**b**) transformed FLCs in the FLSD. Reprinted from Ref. [335] with permission. Copyright 2012, Elsevier.

The experimental techniques to determine FLDs of sheet metals are costly and time-consuming notably testing at elevated temperatures [336]. Thus, many researchers have and developed different numerical techniques and theoretical models which can be implemented easily in numerical simulation software for predicting and analyzing sheet metal's formability, as summarized in Figure 27.
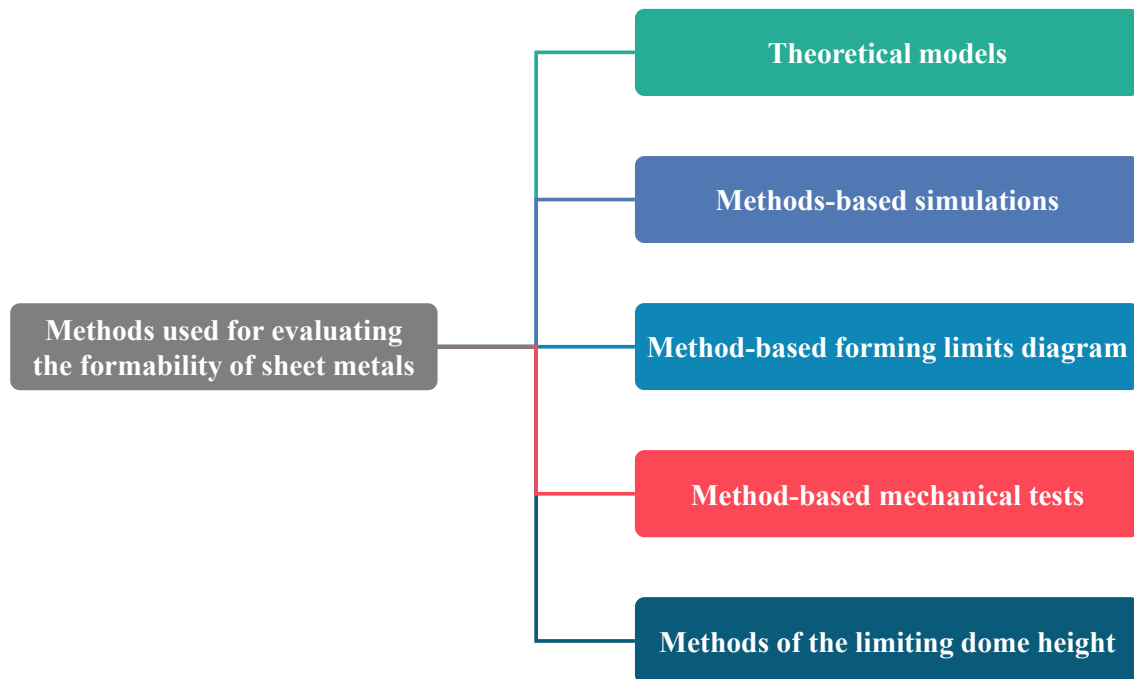
Figure 27. Methods used to evaluate the formability of sheet metals.

Zhang et al. [337] discussed in their study the primary empirical and theoretical models used for evaluating and predicting the formability of sheet metals and categorized them into bifurcation theory-based models, geometrical imperfection theory-based models, continuum damage mechanics (CDM) models and other models based on necking or fracture criteria, as depicted in Figure 28. The details of these models are discussed briefly in Section 5.3. Afterwards, Stoughton and Zhu [332] proposed a theoretical FLD model-based strain and explained its relevance with FLSD. Then, many reviews were performed by Aretz [338], Stoughton and Zhu [332], Hosford and Duncan [339] and Banabic et al. [340] to discuss the development and the progress of different theoretical models such as Hill's, Swift's and M-K models, for several metallic materials, strain paths and process parameters through coupling various hardening laws and yield criteria.
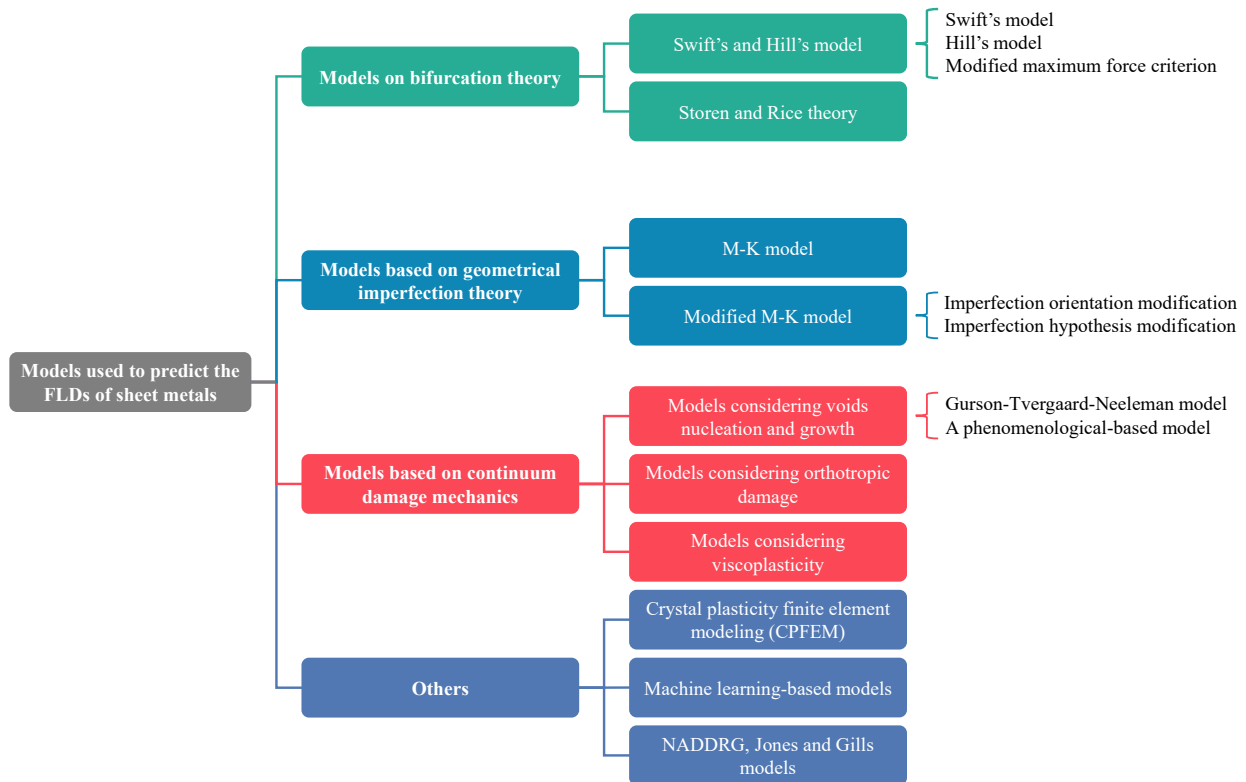
Figure 28. Theoretical and numerical models used for formability prediction.

5.1. Measurement of Surface Strains in Sheet Metal Forming

Measuring surface strains is one of the essential requirements for analyzing and evaluating the formability of sheet metals. Therefore, it is crucial to complete this stage because most of metallic sheets used for forming processes have thicknesses less than 1.5 mm, which may affect the strain measurements. Many techniques (manual and automatic) are used for strain measurements, as summarized in Figure 29 [341].

Figure 29. Classification of automatic strain measurement system.

The manual techniques include a stereo microscope, travelling microscopes and mylar tapes. Bandyopadhyay et al. [342] proposed a manual technique for strain measurement and used these results and their theoretical model to build FLSD to investigate the formability of TWB. Prasad et al. [343] used a stereo microscope technique for measurement of strains and studying the formability of Incon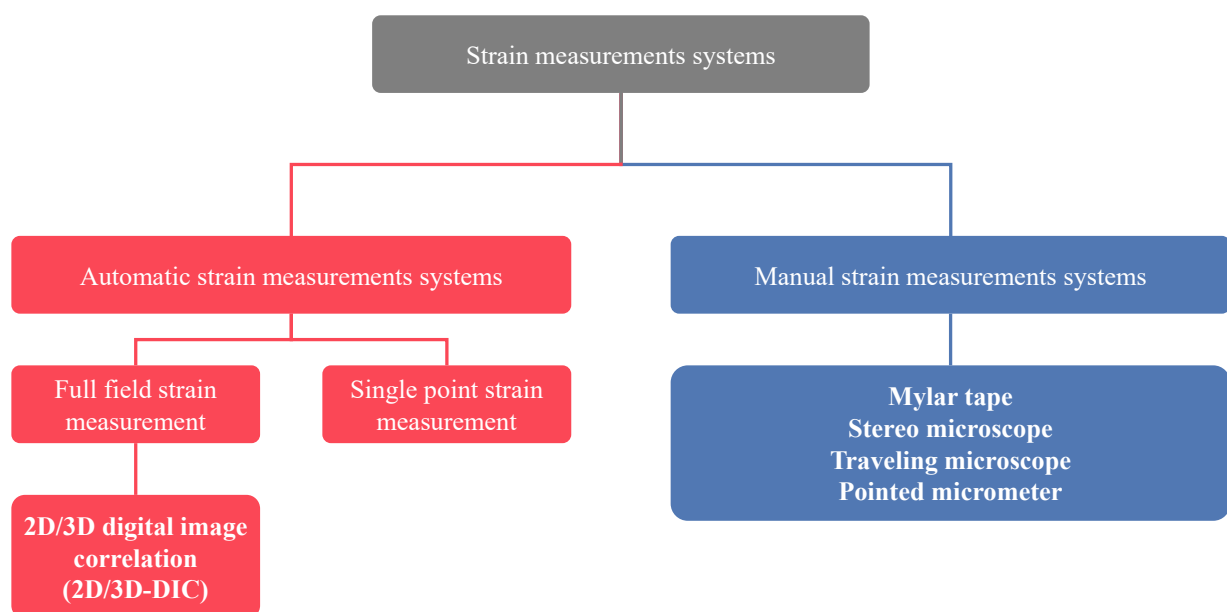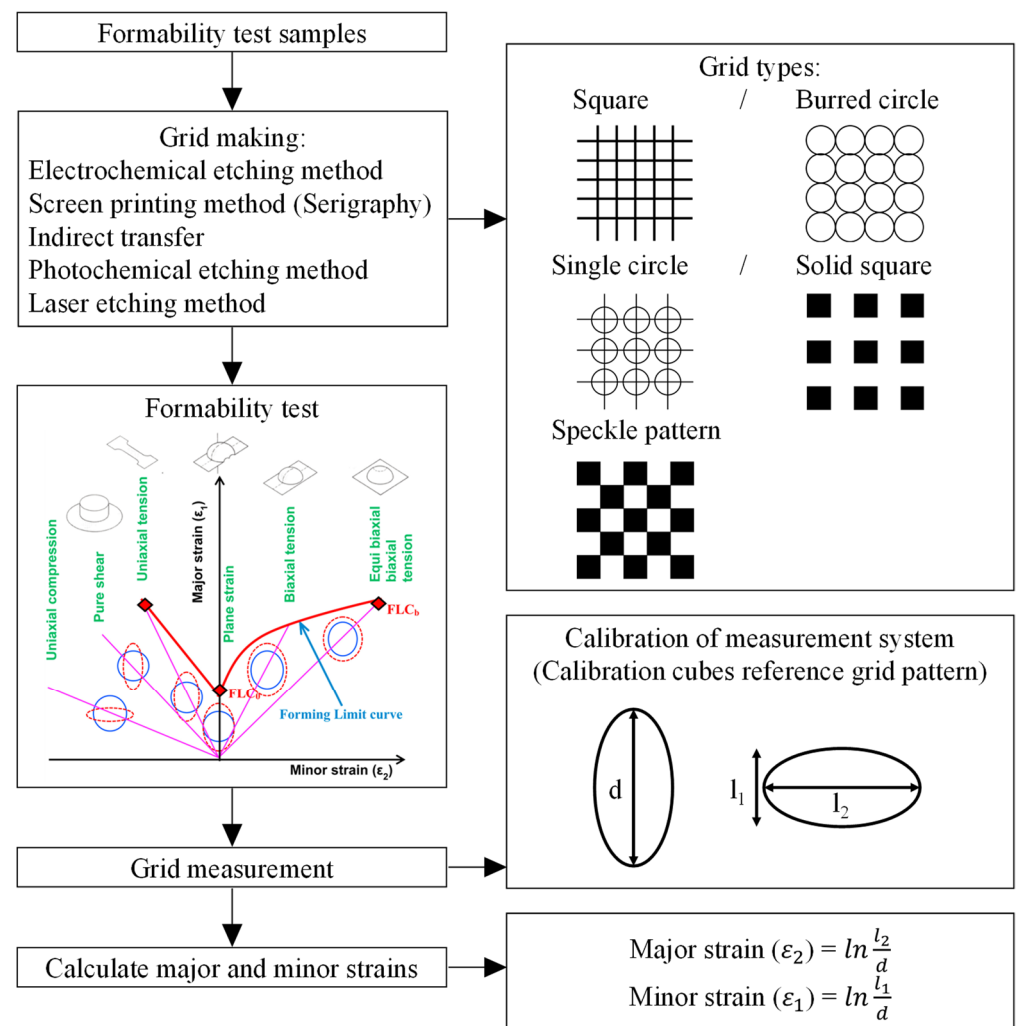el 718. Nevertheless, their techniques are less accurate and time-consuming than automatic techniques. Figure 30 describes the detailed procedures for measuring major and minor strains manually.

Figure 30. Detailed procedures of measuring major and minor strains manually. Reprinted from Ref. [325] with permission. Copyright 2016, Elsevier.

The available automatic strain measurements techniques are for full-field, such as DIC, and single-point strain analyses, as summarized in Figure 29. In GPA, after forming, the deformed grids were captured by a camera, and software was used to fit the ellipse to deformed grids and determine the major and minor the deformed grids strains. On the other hand, the full-field technique commonly uses the principles of DIC to measure strain automatically [344]. This technique assesses deformation and strains with the assistance of a minimum of two images with a mutual geometrical relation. Omar et al. [344] used offline DIC software ARGUS which was proposed via GOM for measuring strains to study the forming limits of welded steel tubes manufactured by hydroforming. Bhargava et al. [345] used an online ARAMIS system to measure strains and construct the FLDs for AHSS sheets. Sutton et al. [346] offered a review discussing DIC's concept, theory and applications for strain measurements. Khoo et al. [347] explained the concept, theory and applications

of the 2D-DIC system. McCormick et al. [348] presented the benefits and uses of DIC to analyze the crack propagations in real scenarios using a low-cost experimental setup.

5.2. Experimental Determination of Forming Limit Diagram (FLD)

The classical stretching tool used to assess sheet metal formability is a punch with a diameter of 20 ± 0.05 developed via Erichsen [349]. Then Olsen [350] modified the test method proposed by Erichsen, but using a different tool size. Afterwards, Hecker [351] introduced a new test method based on the concept of the tests developed by Olsen and Erichsen and used a punch with a bigger diameter of 50 mm to overcome the limitations of the aforementioned tests which were caused by using punches with small diameters. Kotkunde et al. [352] also used Hecker's test in their study and compared the test results predicted from his theoretical model. Jovignot [353] developed a new hydraulic bulging testing machine used notably for equi-biaxial strain path. The formability of sheet metals is usually assessed experimentally by Nakajima test (out-of-plane) [354] or Marciniak test (in-plane) [321]. The test setups and the assessment techniques of Nakajima and Marciniak tests to determine FLDs for sheet metals are standardized via ASTM E2218-15 [355] and ISO 12004–2 [356]. In the Nakajima test, known as limiting dome height (LDH), a hemispherical punch is used; however, a flat bottom cylindrical punch is used for the Marciniak test. Many investigations have been performed to evaluate the formability of sheet metals apart from the standard procedures by using other samples and punch sizes in stretching operations to plot the FLD, where the standard diameters of the hemispherical punch and blank which should be used are 101.4 and 177.8 mm, respectively [357–359]. Several methods were proposed to determine the onset of localized necking in order to improve the accuracy of FLD [360,361]. The methods can be classified into three categories: (1) spatial methods, e.g., from ISO 12004-2 [356] and Zhang et al. [362]; (2) temporal methods, from Volk and Hora [363], Merklein et al. [364] and Hotz et al. [365]; (3) Spatio-temporal methods, from Li et al. [366], Wang et al. [367], Martínez-Donaire et al. [368] and Min et al. [369,370].

Some vital parameters affect the formability test and stretching operation, such as the size of punch and die, blank holding pressure (approximately 2% of the material's yield strength) and draw beads, which are provided for resisting the material flows from the flange region. The punch size is crucial to determine accurate FLD, as mentioned by Basak et al. [371]. They used a sub-size punch in their study to reveal the impact on the accuracy of determining the FLD of sheet metals. They mentioned that sub-size punches are responsible for inducing bending strains in the sheet's outer surfaces which could be overcome by subtracting the bending strains from both major and minor strains. On the other hand, these experimental techniques are time-consuming, costly and complicated and require many specimens for testing under different strain paths. To address the aforementioned issues and overcome the limitations of the experimental procedure, many theoretical and empirical models have been proposed to predict the FLDs of sheet metals. Yield criteria and the hardening model are the key parameters which should be considered to determine the limit strains using theoretical models.

5.3. Determination of FLD via Modelling Techniques

5.3.1. Models Based on Bifurcation Theory

In 1952, Hill [372] and Swift [373] proposed classical models for predicting localized (through-thickness direction) and diffuse necking, respectively, and they assumed that the sheet metal is homogeneous. Then, Hill's model was developed by Aretz [374], where it was assumed that the localized necking occurred once the large forces per unit widths reached to the critical values, not maximum values. Then, Sing and Rao [375] and Chung et al. [376] developed Hill's criterion to determine the forming limits of several steel sheets such as SS4011, DP600 and TWIP940. On the other hand, they can only predict the LHS of the FLDs of sheet metals because of the zero-extension hypothesis. Thus, Swift [373] introduced his model, known as maximum force criterion (MFC), which is based on diffuse necking for the sheet metals deformed biaxially. Swift [373] assumed

in his model that the diffuse necking occurring and the formability limit on strains can be determined once the loading reaches to maximum value. On the other hand, the obtained results commonly underestimate the formability limits strains detected from experimentation [375]. Hora et al. [377,378] considered the impact strain state and modified Swift's model, known as MMFC. Then, Hora et al. [379] performed further modifications to their model and considered the influence of forming temperatures. Storen and Rice [380] introduced a new model (S-R model) for predicting the formability limits strains at the necking onset by assuming a vertex on subsequent yield locus. Then, Hashiguchi and Protasov [381] developed an S-R model to determine the FLDs of several elastoplastic materials under different working conditions. Afterwards, Zhu et al. [382] considered the moment equilibrium and modified the S-R model and Min et al. [383] successfully determined the FLD of 22MnB5 sheet metal at elevated temperatures by coupling the Logan-Hosford criterion with the S-R model.

5.3.2. Models Based on Geometrical Imperfection Theory

Marciniak and Kuczynski [321] proposed a new model (M-K model) based on the geometrical imperfections on the sheets before the deformation to determine the FLD of sheet metals, where the imperfections are assumed to be normal to the major principal stresses, as shown in Figure 31. Then, Hutchinson et al. modified the M-K model [384,385] to predict the FLD of sheet metals by considering an arbitrary angle between the minor principal stress and imperfection. The formability limit strains determined via the M-K model are sensitive to the size of the geometrical imperfection, which is impractical for the applications of formability limit strains predictions [386]. The formability limits strains predicted via the M-K model are commonly overestimated, notably at a high strain ratio [387].
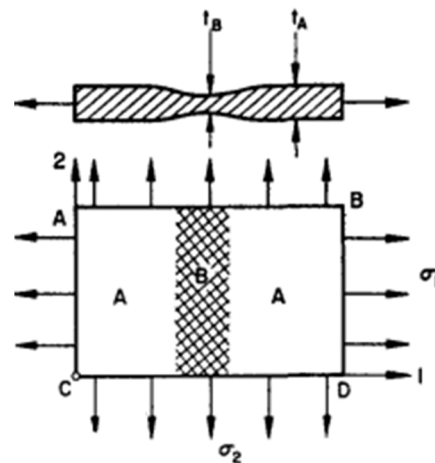
Figure 31. A schematic description of the pre-existing groove supposed in the M-K model before the deformation. Reprinted from Ref. [321] with permission. Copyright 1967, Elsevier.

To address the aforementioned issue, the M-K model was modified via considering the voids growth [388,389] and the roughness surface [390] in the imperfection hypothesis, as depicted in Figure 32. As shown in Figure 32a, based on the zero extension hypothesis proposed by Hill, the imperfection groove was modified in the M-K model. inclined with an angle θ to the minor principal stress [384,385,391,392], as shown in Figure 32b. For instance, Parmar et al. [390] considered the surface roughness of sheet metals in the M-K model and determined the formability limit strains of Al alloys sheets utilizing both modified M-K and Swift's models. They first predicted the sheet's instability via Swift's model; afterwards, they used the modified M-K model to determine the formability limit strains. Thereafter, Bong et al. [393] used the same models (i.e., Swift's model for sheet instability and M-K model for formability limits) to determine the FLDs for stainless steel sheets and

verified their results with those obtained from experimentation. Chan et al. [394], Hashemi et al. [392], Panich et al. [395] and Abedrabbo et al. [396] also modified the M-K model in their studies and predicted the FLDs of different metallic materials such as Al and steel alloys. Needleman and Triantafyllidis [388] and Melander [389] considered the impact of void growth in their modified M-K models and determined the forming limit strains in their investigations.
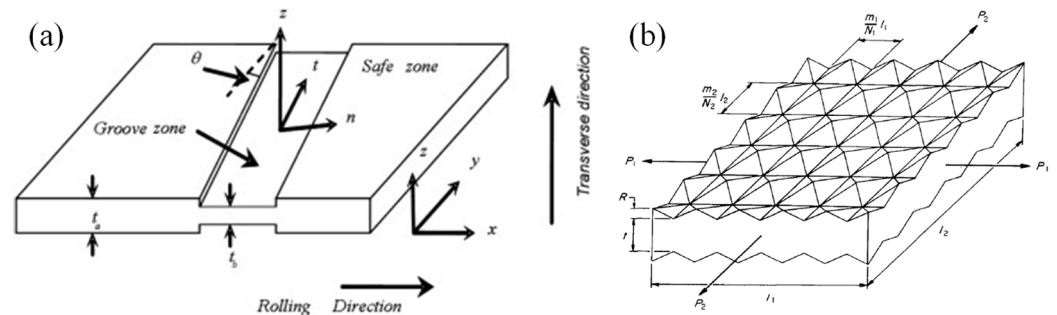
Figure 32. Schematic descriptions of the (**a**) pre-existing groove. Reprinted from Ref. [392] with permission. Copyright 2009, Elsevier; and (**b**) surface roughness considered in the modified M-K model. Reprinted from Ref. [390] with permission. Copyright 1977, Elsevier.

### 5.3.3. Models Based on Continuum Damage Mechanics (CDM)

The ductile fracture process can be classified into three stages, micro-voids nucleation, growth and coalescence [397]. GTN is one of the models based on these processes and has been used to determine the formability limit strains of metallic sheets [398]. Lin et al. and Shao et al. [399,400] proposed new stress-based CDM theories for predicting the FLDs of Al alloy sheets at a wide range of elevated temperatures. Brunet and Morestin [401] modified the GTN model based on Hill's anisotropic yield surface and the necking criterion of Swift's model to determine the formability limits of Al and Ti alloy sheets. Chen and Dong [402] modified the GTN model, using Hill's quadratic stress instead of von Mises stress to determine the FLDS of AA6111-T4 sheets. Chow et al. [403,404] proposed anisotropic damage models for predicting the FLDs of AA6111-T4 sheets at different forming conditions. Then, they developed their model and coupled it with Hill's 48 yield criterion and mixed isotropic-kinematic hardening models to determine the FLD of AA6111-T4 at complex strain paths [405].

5.3.4. Alternative Models

In 1975, a new empirical model was proposed by Keeler and Brazier [406] to determine the major principal strain at plane state. They assumed in their study that FLD consisted of two lines inclined on the major principal strain with an angle of 20° for the RHS and 45° for the LHS in the FLD. Then, Bleck et al. [407] utilized this model for predicting the formability limits for IF and DP steel sheets, because it is suitable only for ultra-deep drawable steels. Slota and Spisak [408] obtained the same conclusions when they used this model in their study to determine the FLDs of various steels. Afterwards, Djavanroodi and Derogar [409] utilized Keeler's model for predicting the FLDs of both Al6016-T6 and Ti6Al4V sheets; however, the model tended to overestimate the formability limits. Jones and Gillis [410] introduced a new model (J-G model) to determine formability limit strains at the beginning of necking. Still, they obtained the formability limits in RHS of the FLD only because of their assumption that the neck direction is normal to major principal stress. Then, Choi et al. [411] modified the J-G model and determined the FLDs for different Al alloys sheets. Compared with the experimental results, the developed J-G model can successfully determine the FLDs for AA2036-T4 and AA1100-H19 alloys but not for AA3003-O alloy.

Artificial neural network (ANN) has also been applied to predict FLDs for a perforated sheet with different geometrical features which are the input of this model, while limit strains are the output, as depicted in Figure 33 [412]. It is required in the ANN model

to train huge experimental data; afterwards, the limit strains can be determined at other forming conditions. For instance, Elangovan et al. [412] and Kotkunde et al. [413] developed their own ANN-based models for predicting the FLDs of pure Al alloys and Ti-6Al-4V alloy, respectively.
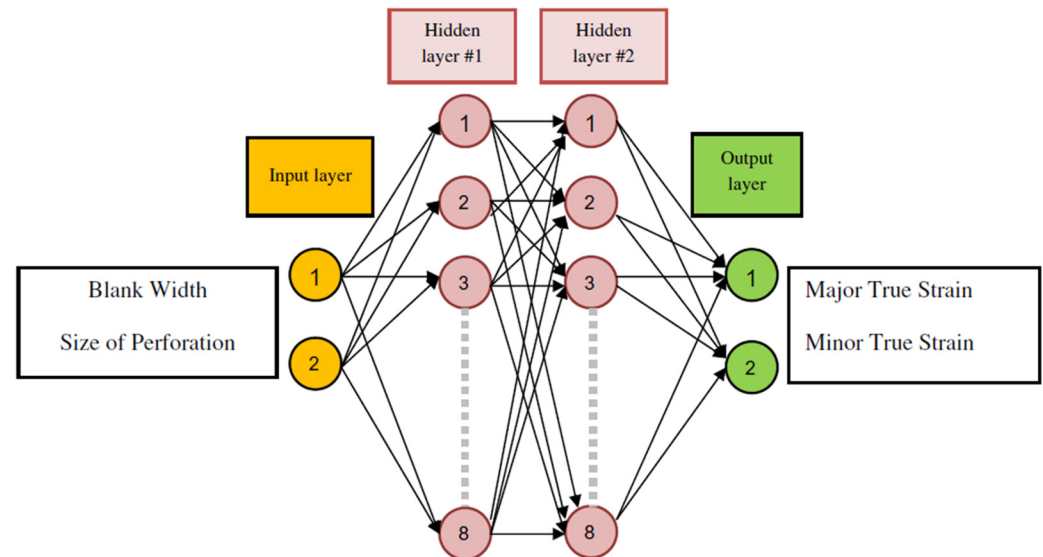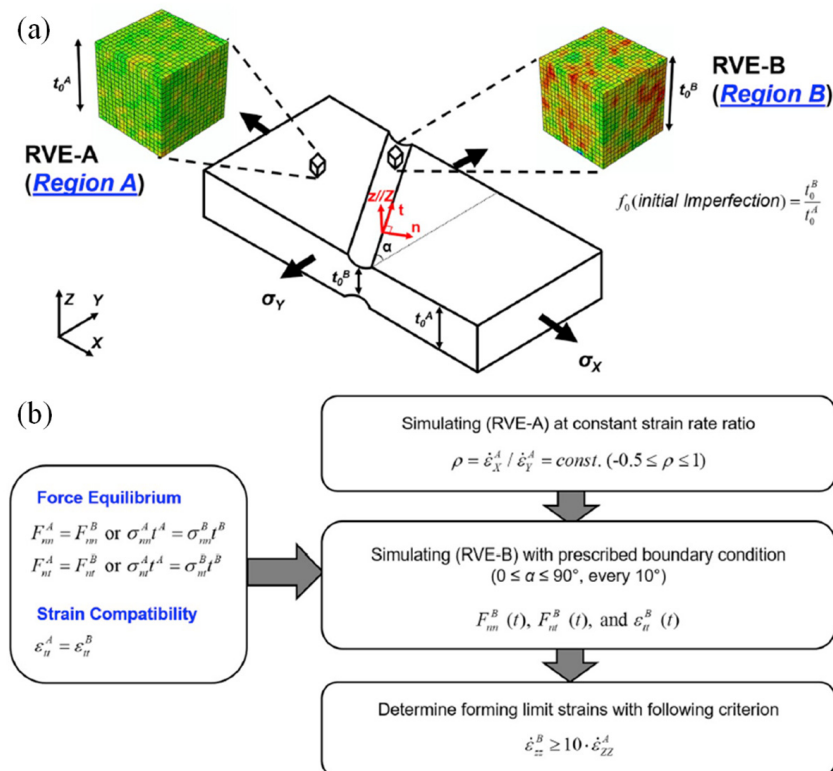

Figure 33. A schematic description of ANN-based model. Reprinted from Ref. [412] with permission. Copyright 2010, Elsevier.

As mentioned previously, most theoretical models used to predict the FLD of metallic materials are based on the M-K model, where initial linear imperfections are typically assumed on the sheet's surface. Then, many investigations were performed to modify the M-K model and improve its prediction capability by considering other microstructure inhomogeneity. For instance, Wu et al. [414], Savoie et al. [415], McGinty et al. [416], Inal et al. [417], Neil and Agnew [418], Wang et al. [419] and Kim et al. [420] considered sheet texture to improve the modified M-K model. Besides, Ragab and Saleh [421] and Bong et al. [393,422] considered void density and surface roughness in their investigations. Karafillis and Boyce [423] and Barlat et al. [123,424] combined the M–K model with advanced models especially yield function, to consider the plastic anisotropy of sheet metals before and after deformation. Furthermore, Banabic et al. [340], Bong et al. [425] and Panich et al. [395] proposed several M-K-based techniques to predict the FLD of sheet metals with acceptable precision at room and elevated temperatures. Nevertheless, it is still challenging to consider plastic anisotropy due to the change in the shape of the yield surface during deformation. The considerations of the plastic anisotropy in Mg alloys is more important than those of FCC and BCC sheet metals because of their low crystal symmetry and limited slip activities [426]. CP modelling can track the plastic anisotropy of sheet metals by considering textures changes during non-proportional loading [238]. Thus, researchers employed CP modelling to predict the FLDs of such sheet metals [414–420,427–431] by coupling the M-K model with crystal plasticity. Their new framework was based on the RVE, representing a single material point on the metallic sheet. Tadano et al. [432] used the homogenization framework developed by Guedes and Kikuchi [433] and coupled it with the M-K model to determine the FLDs of FCC sheet metals. Besides, they introduced a novel technique to predict the localization onset via simulating the RVEs for two material points only. Hajian et al. [434,435] combined the M–K model with their new 2D-CPFE model. They assumed initial imperfections oriented along different directions and simulated the forming limits criterion. The above-mentioned models [429,432–435] could not precisely solve the issue of heterogeneity of stresses and strains in the thickness direction. Thus, researchers proposed the 3D-CPFE model with multi-grains in the thickness direction and introduced multiscale frameworks-based CP modelling to predict FLDs accurately. However, there are limitations

in the computational time required for the frameworks proposed by Srivastava et al. [427] and Mohammed et al. [436]. Kim et al., [420] tried to address the aforementioned issue by proposing a computationally effective multiscale approach by combining the M-K model with their CPFE model to determine the forming limit strains of BCC sheet using 2 RVEs for imperfection and uniform areas, as depicted in Figure 34. As depicted in Figure 35, Bong et al. [437] proposed a novel framework that combined their modified CPFE model and M-K model, which successfully predicted the FLDS of AZ31 and ZE10 Mg sheets.
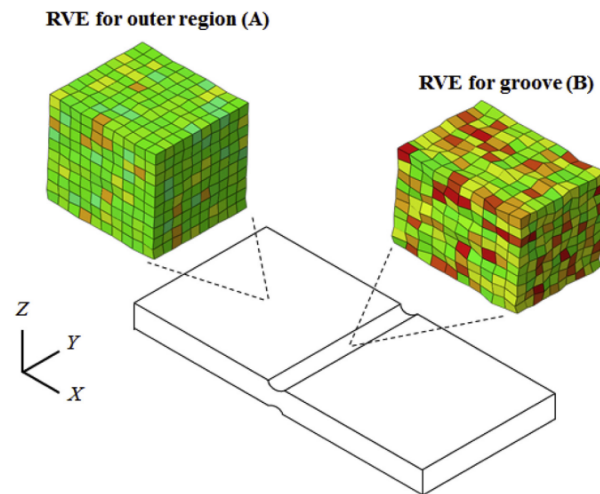
Figure 34. A schematic description of a multiscale approach that coupling the M-K model and CPFEM. Reprinted from Ref. [420] with permission. Copyright 2017, Elsevier.

Figure 35. A schematic description of the novel multiscale approach proposed by Bong et al. [437] to predict the FLDs of AZ31 and ZE10 Mg sheets: (**a**) schematic of the proposed hybrid approach; (**b**) flowchart for the multiscale FLD prediction. Reprinted from Ref. [437] with permission. Copyright 2020, Elsevier.

Although CP has been regarded as an outstanding modelling tool, it requires higher computational time for its broad applications. Thus, several techniques such as a spectral database technique [438–440], wavelet transformations-based algorithm [441,442], graphics processing unit (GPUs)-acceleration of CP [443,444] and parallel computing [445] were implemented for accelerating the CP simulations. Recently, machine learning (ML) methods have gained attention in CP applications due to its ability to accelerate the CP simulations via a function approximation tool, instead of these being explicitly programmed [446]. ML techniques usually depend on trained models which are not computationally demanding, compared to conventional numerical simulations. For instance, Ali et al. [447] proposed a new approach by coupling ANN and CPFEM to predict the flow behavior of Al sheet metal subjected to complex strain paths. Yuan et al. [448] introduced a novel ML-based reduced order CP model to predict the flow behavior of FCC sheet metals. Miyazawa et al. [449] developed a new framework by coupling ML and CP modelling and predicted the mechanical behavior of steel under cyclic loading. Pandey and Pokharel [450] used ML approaches coupled with CP modelling to predict the texture evolution of copper sheets subjected to uniaxial tension. Acar [451] proposed a novel ML-based computational framework to predict CP parameters and revealed the relations of these parameters with the texture of Ti alloy, as depicted in Figure 36. Ibragimova et al. [452] proposed a novel approach to predict the localized deformation in sheet metals by coupling convolutional neural network (CNN) and CPFEM, as depicted in Figure 37, to predict localized deformation in metals.
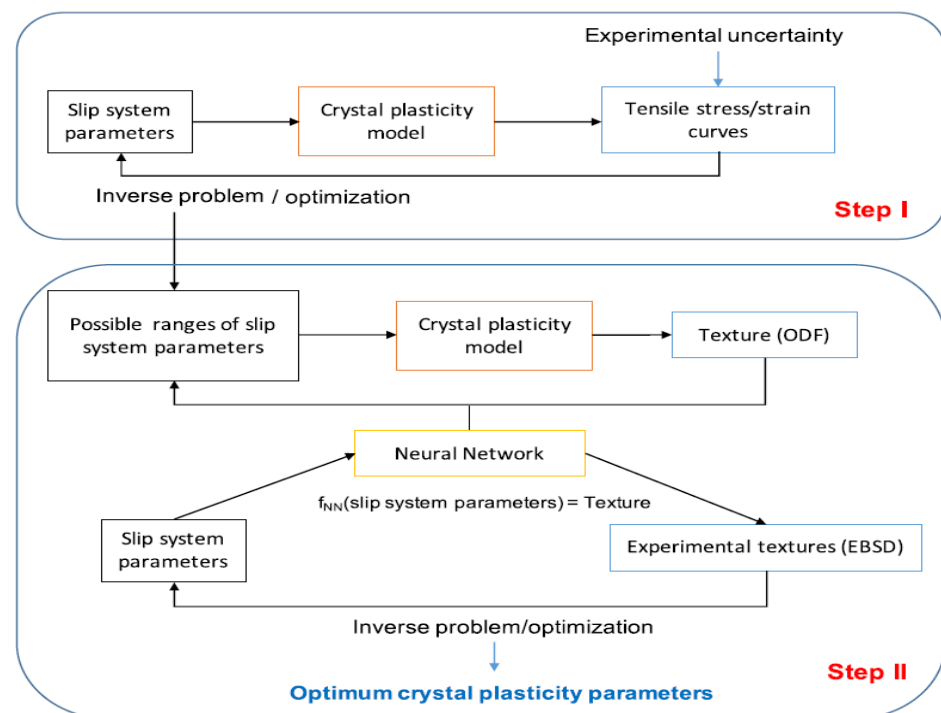
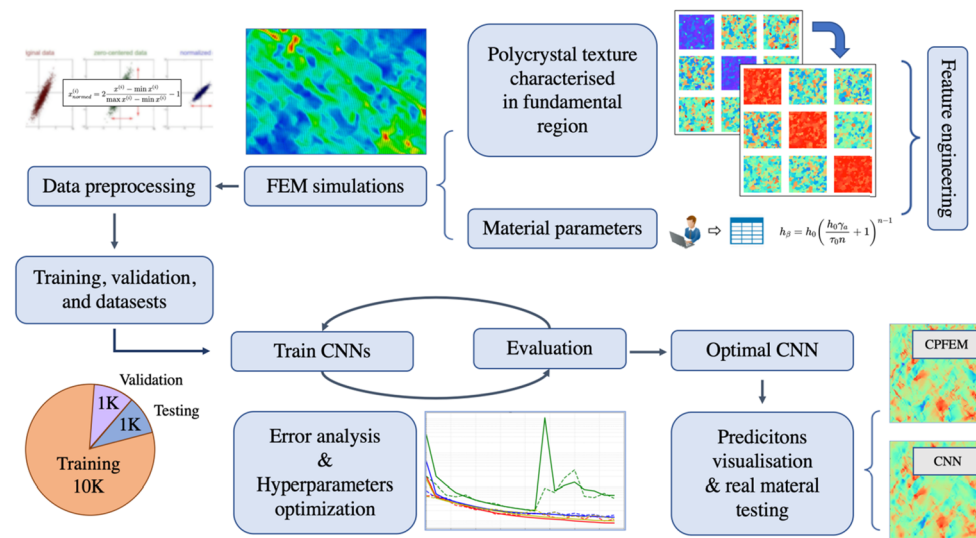**Figure 36.** A schematic description of the novel multiscale approach proposed by Acar [451]. Reprinted from Ref. [451] with permission. Copyright 1963, AIAA.

Figure 37. A schematic description of the novel framework proposed by Ibragimova et al. [452] to predict the FLDs of AZ31 and ZE10 Mg sheets. Reprinted from Ref. [452] with permission. Copyright 2022, Elsevier.

6. Conclusions and Outlook

6.1. Conclusions and Remarks

This comprehensive review discussed the characterization and modelling approaches for SMF of lightweight alloys based on the PRISMA guidelines. The following conclusions can be drawn:

- In the past few decades, the numerical methods in SMF simulation have undergone rapid development, including from two-dimensional to three-dimensional, from symmetric to asymmetric, from classical to advanced constitutive models, traditional mesh to meshless, etc.

- Plasticity models under NAFR were widely developed and applied in SMF simulation due to high accuracy, high flexibility, user-friendly parameter identification and convenient consideration of the continuous anisotropic/distortional hardening (yield surface evolution) of lightweight alloys under proportional and non-proportional loadings.

- Advanced CP models can capture the underlying process-microstructure-properties for the physical mechanisms. Besides, applying CP models in predicting the constitutive behaviors of lightweight alloys under complex loading conditions (challenging to achieve in mechanical characterization) has drawn significant attention.

- The application of the DIC technique improved the accuracy of mechanical characterization and promoted the development of advanced characterization techniques, e.g., inverse engineering. Novel mechanical characterization methods under SPCs, rather than reverse loadings, are required for the engineering application of advanced lightweight alloys.

- The formability (FLD) of sheet metals is usually assessed experimentally by Nakajima test (out-of-plane) or Marciniak test (in-plane). Several methods were developed to determine the onset of localized necking, e.g., spatial methods, temporal methods and spatio-temporal methods.

- Theoretical models based upon bifurcation theory, geometrical imperfection theory and continuum damage mechanics were developed to predict the forming limit strains of lightweight alloys under various loading conditions, e.g., strain path changes, through coupling different hardening laws and yield criteria.

- Multiscale forming limit diagram (FLD) prediction schemes were developed by combining the CPFEM with the geometrical imperfection theory, e.g., M–K model. Besides,

approaches or frameworks by coupling machine learning and CP simulations were proposed to predict the FLD of lightweight alloys.

6.2. Outlook and Future Directions

Despite the extensive knowledge accumulated in characterization and modelling approaches for SMF of lightweight metallic materials, there are still several directions of progressive research that should be continued:

➢ The development and application of advanced multiscale modelling approaches for the simulations of SMF under particular conditions (or extreme manufacturing), such as hydrogen environments, cryogenic temperatures and heterostructures/laminated materials, is notable.

➢ For phenomenological constitutive modelling, these efforts include the development of the NAFR framework via analytical parameter identification. Attention should be further focused on stress state-dependent anisotropy and hardening due to the specific underlying mechanisms, such as phase transformation and slip/twinning activity in advanced lightweight materials.

➢ The inverse engineering method, as the next-generation of mechanical characterization, for identification of the parameters of advanced constitutive models under large plastic strains should be highlighted. The focus should be on a reasonable choice of the optimization algorithm and the constitutive model. A suitable plasticity model with high flexibility and fidelity should be selected appropriately in inverse engineering.

➢ Machine learning-based methods, such as artificial neural network, are drawing more attention. As fundamental inputs to train and test these data-driven models, massive, accurate and representative data are crucial to the parameterized artificial intelligence framework. This requirement dramatically fosters the development of advanced characterization techniques, including mechanical experiments and virtual data generation based on accurate multi-physics models (e.g., CP) for advanced lightweight materials.

References

1. Tisza, M.; Czinege, I. Comparative study of the application of steels and aluminium in lightweight production of automotive parts. *Int. J. Lightweight Mater. Manuf.* **2018**, *1*, 229–238. [CrossRef]
2. Blanco, D.; Rubio, E.M.; Lorente-Pedreille, R.M.; Sáenz-Nuño, M.A. Lightweight Structural Materials in Open Access: Latest Trends. *Materials* **2021**, *14*, 6577. [CrossRef]
3. Gloria, A.; Montanari, R.; Richetta, M.; Varone, A. Alloys for Aeronautic Applications: State of the Art and Perspectives. *Metals* **2019**, *9*, 662. [CrossRef]
4. Mallick, P.K. *Materials, Design and Manufacturing for Lightweight Vehicles*; Woodhead Publishing: Cambridge, UK, 2020.
5. Hirsch, J. Recent development in aluminium for automotive application. *Trans. Nonferrous Met. Soc. China.* **2014**, *24*, 1995–2002. [CrossRef]
6. Zeng, X.; Li, M.; Abd El-Hady, D.; Alshitari, W.; Al-Bogami, A.S.; Lu, J.; Amine, K. Commercialization of lithium battery technologies for electric vehicles. *Adv. Energy Mater.* **2019**, *9*, 1900161. [CrossRef]
7. İnci, M.; Büyük, M.; Demir, M.H.; İlbey, G. A review and research on fuel cell electric vehicles: Topologies, power electronic converters, energy management methods, technical challenges, marketing and future aspects. *Renew. Sustain. Energy Rev.* **2021**, *137*, 110648. [CrossRef]
8. Kulekci, M.K. Magnesium and its alloys applications in automotive industry. *Int. J. Adv. Manufac-Turing Technol.* **2008**, *39*, 851–865. [CrossRef]
9. Zhang, W.; Xu, J. Advanced lightweight materials for Automobiles: A review. *Mater. Des.* **2022**, *221*, 110994. [CrossRef]
10. Abd El-Aty, A.; Xu, Y.; Guo, X.; Zhang, S.-H.; Ma, Y.; Chen, D. Strengthening mechanisms, deformation behavior, and anisotropic mechanical properties of Al-Li alloys: A review. *J. Adv. Res.* **2018**, *10*, 49–67. [CrossRef]
11. Assempour, A.; Emami, M.R. Pressure estimation in the hydroforming process of sheet metal pairs with the method of upper bound analysis. *J. Mater. Process. Technol.* **2009**, *209*, 2270–2276. [CrossRef]
12. Lan, J.; Dong, X.; Li, Z. Inverse finite element approach and its application in sheet metal forming. *J. Mater. Process. Technol.* **2005**, *170*, 624–631. [CrossRef]
13. Kim, S.H.; Kim, S.H.; Huh, H. Finite element inverse analysis for the design of intermediate dies in multi-stage deep-drawing processes with large aspect ratio. *J. Mater. Process. Technol.* **2001**, *113*, 779–785. [CrossRef]
14. Tang, B.; Li, Y.; Lu, X. Developments of multistep inverse finite element method and its application in formability prediction of multistage sheet metal forming. *J. Manuf. Sci. Eng.* **2010**, *132*, 041013. [CrossRef]
15. Van Houtte, P.; Gawad, J.; Eyckens, P.; Van Bael, B.; Samaey, G.; Roose, D. Multi-scale modelling of the development of heterogeneous distributions of stress, strain, deformation texture and anisotropy in sheet metal forming. *Procedia IUTAM* **2012**, *3*, 67–75. [CrossRef]
16. Barik, S.; Narayanan, R.; Sahoo, N. Forming response of AA5052–H32 sheet deformed using a shock tube. *Trans. Nonferrous Met. Soc. China* **2020**, *30*, 603–618. [CrossRef]
17. Nakata, T.; Xu, C.; Ohashi, H.; Yoshida, Y.; Yoshida, K.; Kamado, S. New Mg–Al based alloy sheet with good room-temperature stretch formability and tensile properties. *Scr. Mater.* **2020**, *180*, 16–22. [CrossRef]
18. Badrish, A.; Morchhale, A.; Kotkunde, N.; Singh, S.K. Influence of material modeling on warm forming behavior of nickel based super alloy. *Int. J. Mater. Form.* **2020**, *13*, 445–465. [CrossRef]
19. Neto, D.; Oliveira, M.; Santos, A.; Alves, J.; Menezes, L. Influence of boundary conditions on the prediction of springback and wrinkling in sheet metal forming. *Int. J. Mech. Sci.* **2017**, *122*, 244–254. [CrossRef]
20. Fei, H.; Mo, J.; Qi, H.; Long, R.; Cui, X.; Li, Z. Springback prediction for incremental sheet forming based on FEM-PSONN technology. *Trans. Nonferrous Met. Soc. China* **2013**, *23*, 1061–1071. [CrossRef]
21. Min, J.; Guo, N.; Hou, Y.; Jiang, K.; Chen, X.; Carsley, J.E.; Lin, J. Effect of tension-compression testing strategy on kinematic model calibration and springback simulation of advanced high strength steels. *Int. J. Mater. Form.* **2021**, *14*, 435–448. [CrossRef]
22. Hou, Y.; Min, J.; Lin, J.; Liu, Z.; Carsley, J.E.; Stoughton, T.B. Springback prediction of sheet metals using improved material models. *Procedia Eng.* **2017**, *207*, 173–178. [CrossRef]
23. Hu, Q.; Zhang, F.; Li, X.; Chen, J. Overview on the prediction models for sheet metal forming failure: Necking and ductile fracture. *Acta Mech. Solida Sin.* **2018**, *31*, 259–289. [CrossRef]
24. Jeong, W.; Kim, C.; Lee, C.-A.; Bong, H.J.; Hong, S.-H.; Lee, M.-G. A probabilistic mean-field and microstructure based finite element modeling for predicting mechanical and ductile fracture behavior of the cast aluminum alloy. *Int. J. Plast.* **2022**, *154*, 103299. [CrossRef]
25. Li, T.; Garg, R.; Galvin, J.; Pannala, S. Open-source MFIX-DEM software for gas-solids flows: Part II—Validation studies. *Powder Technol.* **2012**, *220*, 138–150. [CrossRef]
26. Neuwirth, J.; Antonyuk, S.; Heinrich, S.; Jacob, M. CFD–DEM study and direct measurement of the granular flow in a rotor granulator. *Chem. Eng. Sci.* **2013**, *86*, 151–163. [CrossRef]
27. Martínez-Valle, Á.; Martínez-Jiménez, J.M.; Goes, P.; Faes, K.; De Waele, W. Multiphysics fully-coupled modelling of the electromagnetic compression of steel tubes. In *Advanced Materials Research*; Trans Tech Publications Ltd.: Zurich, Switzerland, 2011; pp. 31–39.
28. Liu, X.; Li, H.; Zhan, M. A review on the modeling and simulations of solid-state diffusional phase transformations in metals and alloys. *Manuf. Rev.* **2018**, *5*, 10. [CrossRef]

29. Rodríguez-Martínez, J.A.; Rusinek, A.; Pesci, R.; Zaera, R. Experimental and numerical analysis of the martensitic transformation in AISI 304 steel sheets subjected to perforation by conical and hemispherical projectiles. *Int. J. Solids Struct.* **2013**, *50*, 339–351. [CrossRef]

30. Jo, S.Y.; Hong, S.; Han, H.-N.; Lee, M.-G. Modeling and Simulation of Steel Rolling with Microstructure Evolution: An Overview. *Steel Res. Int.* **2023**, 2200260. [CrossRef]

31. Park, J.; Rout, M.; Min, K.-M.; Chen, S.-F.; Lee, M.-G. A fully coupled crystal plasticity-cellular automata model for predicting thermomechanical response with dynamic recrystallization in AISI 304LN stainless steel. *Mech. Mater.* **2022**, *167*, 104248. [CrossRef]

32. Liewald, M.; Riedmüller, K.R. A new one-phase material model for the numerical prediction of critical material flow conditions in thixoforging processes. *CIRP Ann.* **2019**, *68*, 293–296. [CrossRef]

33. Amaral, R.; Santos, A.D.; de Sá José, C.; Miranda, S. Formability prediction for AHSS materials using damage models. In *Journal of Physics: Conference Series*; IOP Publishing: Bristol, England, 2017; p. 012018.

34. Oliveira, M.C.; Fernandes, J.V. Modelling and simulation of sheet metal forming processes. *Metals* **2019**, *9*, 1356. [CrossRef]

35. Wadas, T.; Tisza, M. *Lightweight Manufacturing of Automotive Parts*; IOP Publishing: Bristol, England, 2020.

36. Gronostajski, Z.; Pater, Z.; Madej, L.; Gontarz, A.; Lisiecki, L.; Łukaszek-Sołek, A.; Łuksza, J.; Mróz, S.; Muskalski, Z.; Muzykiewicz, W. Recent development trends in metal forming. *Arch. Civ. Mech. Eng.* **2019**, *19*, 898–941. [CrossRef]

37. Wang, P.-Y.; Wang, Z.-J.; Xiang, N.; Li, Z.-X. Investigation on changing loading path in sheet metal forming by applying a property-adjustable flexible-die. *J. Manuf. Processes* **2020**, *53*, 364–375. [CrossRef]

38. Flegler, F.; Neuhäuser, S.; Groche, P. Influence of sheet metal texture on the adhesive wear and friction behaviour of EN AW-5083 aluminum under dry and starved lubrication. *Tribol. Int.* **2020**, *141*, 105956. [CrossRef]

39. Evin, E.; Tomáš, M. Verification of Friction Models Implemented in the Simulation Software. In *Materials Science Forum*; Trans Tech Publications Ltd.: Zurich, Switzerland, 2020; pp. 223–231.

40. Shisode, M.P.; Hazrati, J.; Mishra, T.; de Rooij, M.; van den Boogaard, T. Modeling mixed lubrication friction for sheet metal forming applications. *Procedia Manuf.* **2020**, *47*, 586–590. [CrossRef]

41. Sigvant, M.; Pilthammar, J.; Hol, J.; Wiebenga, J.H.; Chezan, T.; Carleer, B.; van den Boogaard, T. Friction in sheet metal forming: Influence of surface roughness and strain rate on sheet metal forming simulation results. *Procedia Manuf.* **2019**, *29*, 512–519. [CrossRef]

42. Sulaiman, M.; Farahana, R.; Bienk, K.; Nielsen, C.; Bay, N. Effects of DLC/TiAlN-coated die on friction and wear in sheet-metal forming under dry and oil-lubricated conditions: Experimental and numerical studies. *Wear* **2019**, *438*, 203040. [CrossRef]

43. Seshacharyulu, K.; Bandhavi, C.; Naik, B.B.; Rao, S.S.; Singh, S. Understanding Friction in sheet metal forming—A review. *Mater. Today Proc.* **2018**, *5*, 18238–18244. [CrossRef]

44. Park, J.; Min, K.M.; Kim, H.; Hong, S.-H.; Lee, M.-G. Integrated Computational Materials Engineering for Advanced Automotive Technology: With Focus on Life Cycle of Automotive Body Structure. *Adv. Mater. Technol.* **2022**, 2201057. [CrossRef]

45. El-Aty, A.A.; Guo, X.; Lee, M.-G.; Tao, J.; Hou, Y.; Hu, S.; Li, T.; Wu, C.; Yang, Q. A review on flexibility of free bending forming technology for manufacturing thin-walled complex-shaped metallic tubes. *Int. J. Lightweight Mater. Manuf.* **2023**, *6*, 165–188. [CrossRef]

46. da Silva, G.S.; Kosteski, L.E.; Iturrioz, I. Analysis of the failure process by using the Lattice Discrete Element Method in the Abaqus environment. *Theor. Appl. Fract. Mech.* **2020**, *107*, 102563. [CrossRef]

47. Tallinen, T.; Åström, J.A.; Timonen, J. Discrete element simulations of crumpling of thin sheets. *Comput. Phys. Commun.* **2009**, *180*, 512–516. [CrossRef]

48. Topčagić, Z.; Križaj, D.; Bulić, E. Application of a current sheet in BEM analysis for numerical calculation of torque in the magnetostatic field. *IEEE Trans. Magn.* **2020**, *56*, 1–9. [CrossRef]

49. Saad, M.; Akhtar, S.; Srivastava, M.; Chaurasia, J. Role of simulation in metal forming processes. *Mater. Today Proc.* **2018**, *5*, 19576–19585. [CrossRef]

50. Wu, Y.; Shen, Y.; Chen, K.; Yu, Y.; He, G.; Wu, P. Multi-scale crystal plasticity finite element method (CPFEM) simulations for shear band development in aluminum alloys. *J. Alloys Compd.* **2017**, *711*, 495–505. [CrossRef]

51. Mellbin, Y.; Hallberg, H.; Ristinmaa, M. A combined crystal plasticity and graph-based vertex model of dynamic recrystallization at large deformations. *Modell. Simul. Mater. Sci. Eng.* **2015**, *23*, 045011. [CrossRef]

52. Abd El-Aty, A.; Xu, Y.; Ha, S.; Zhang, S.-H. Computational homogenization of tensile deformation behaviors of a third generation Al-Li alloy 2060-T8 using crystal plasticity finite element method. *Mater. Sci. Eng. A* **2018**, *731*, 583–594. [CrossRef]

53. Abd El-Aty, A.; Zhang, S.-H.; Xu, Y.; Ha, S. Deformation behavior and anisotropic response of 2060 Al-Cu-Li alloy: Experimental investigation and computational homogenization-based crystal plasticity modeling. *J. Mater. Res. Technol.* **2019**, *8*, 1235–1249. [CrossRef]

54. Xue, F.; Li, F.; Li, J.; He, M.; Yuan, Z.; Wang, R. Numerical modeling crack propagation of sheet metal forming based on stress state parameters using XFEM method. *Comput. Mater. Sci.* **2013**, *69*, 311–326. [CrossRef]

55. Yuan, B.; Wang, Z. A multi-deformable bodies solution method coupling finite element with meshless method in sheet metal flexible-die forming. *Procedia Eng.* **2017**, *207*, 1641–1646. [CrossRef]

56. Kochmann, J.; Wulfinghoff, S.; Reese, S.; Mianroodi, J.R.; Svendsen, B. Two-scale FE–FFT-and phase-field-based computational modeling of bulk microstructural evolution and macroscopic material behavior. *Comput. Methods Appl. Mech. Eng.* **2016**, *305*, 89–110. [CrossRef]

57. Gasiorek, D.; Baranowski, P.; Malachowski, J.; Mazurkiewicz, L.; Wiercigroch, M. Modelling of guillotine cutting of multi-layered aluminum sheets. *J. Manuf. Process.* **2018**, *34*, 374–388. [CrossRef]

58. Crutzen, Y.; Boman, R.; Papeleux, L.; Ponthot, J.-P. Lagrangian and arbitrary Lagrangian Eulerian simulations of complex roll-forming processes. *C.R. Mec.* **2016**, *344*, 251–266. [CrossRef]

59. Kaftanoglu, B.; Tekkaya, A. Complete numerical solution of the axisymmetrical deep-drawing problem. *J. Eng. Mater. Technol.* **1981**, *103*, 326–332. [CrossRef]

60. Makinouchi, A. Sheet metal forming simulation in industry. *J. Mater. Process. Technol.* **1996**, *60*, 19–26. [CrossRef]

61. Makinouchi, A.; Teodosiu, C.; Nakagawa, T. Advance in FEM simulation and its related technologies in sheet metal forming. *CIRP Ann.* **1998**, *47*, 641–649. [CrossRef]

62. Tekkaya, A.E. State-of-the-art of simulation of sheet metal forming. *J. Mater. Process. Technol.* **2000**, *103*, 14–22. [CrossRef]

63. Tisza, M. Numerical modelling and simulation in sheet metal forming. *J. Mater. Process. Technol.* **2004**, *151*, 58–62. [CrossRef]

64. Wenner, M.L. Overview—Simulation of Sheet Metal Forming. AIP Conference Proceedings; American Institute of Physics: College Park, MD, USA, 2005; pp. 3–7.

65. Ahmed, M.; Sekhon, G.; Singh, D. Finite element simulation of sheet metal forming processes. *Def. Sci. J.* **2005**, *55*, 389. [CrossRef]

66. Banabic, D. *Sheet Metal Forming Processes: Constitutive Modelling and Numerical Simulation*; Springer Science & Business Media: Berlin, Germany, 2010. [CrossRef]

67. Akhavan Farid, A.; Shen, F.S.; Rahimian Koloor, S.S.; Petrů, M. Quality evaluation of aluminum-AA6061 truncated cone deformed by single point incremental forming. *J. Braz. Soc. Mech. Sci. Eng.* **2022**, *44*, 420. [CrossRef]

68. Yan, B.Y.; Meng, B. Wall thickness control in multi-stage hydroforming of multiwave seal ring with small diameter. *IOP Conf. Ser. Mater. Sci. Eng.* **2022**, *1270*, 012067. [CrossRef]

69. Liu, Y.; Min, J.; Zhang, J.; Cai, W.; Carlson, B.E.; Bobel, A.C.; Hector, L.G.; Sachdev, A.K. Laser-assisted robotic roller forming of an ultrahigh strength martensitic steel. *J. Manuf. Process.* **2022**, *82*, 192–202. [CrossRef]

70. Ablat, M.A.; Qattawi, A. Numerical simulation of sheet metal forming: A review. *Int. J. Adv. Manuf. Technol.* **2017**, *89*, 1235–1250. [CrossRef]

71. Chung, K.; Lee, M.-G. *Basics of Continuum Plasticity*; Springer: Berlin, Germany, 2018. [CrossRef]

72. Trzepieciński, T. Recent developments and trends in sheet metal forming. *Metals* **2020**, *10*, 779. [CrossRef]

73. Raabe, D.; Klose, P.; Engl, B.; Imlau, K.-P.; Friedel, F.; Roters, F. Concepts for Integrating Plastic Anisotropy into Metal Forming Simulations. *Adv. Eng. Mater.* **2002**, *4*, 169–180. [CrossRef]

74. Yanagimoto, J.; Oya, T.; Kawanishi, S.; Tiesler, N.; Koseki, T. Enhancement of bending formability of brittle sheet metal in multilayer metallic sheets. *CIRP Ann.* **2010**, *59*, 287–290. [CrossRef]

75. Rydz, D.; Stradomski, G.; Szarek, A.; Kubik, K.; Kordas, P. The Analysis of Pressed Cups Producing Possibilities from Rolled Bimetallic Al-1050 + Cu-M1E Sheets. *Materials* **2020**, *13*, 2413. [CrossRef]

76. Kim, D.; Kim, H.; Kim, J.H.; Lee, M.G.; Kim, K.J.; Barlat, F.; Lee, Y.; Chung, K. Modeling of forming limit for multilayer sheets based on strain-rate potentials. *Int. J. Plast.* **2015**, *75*, 63–99. [CrossRef]

77. Bagheri, A.; Shabani, A.; Toroghinejad, M.R.; Taherizadeh, A. Post-rolling annealing of a multilayered Brass/IFS/Brass composite: An evaluation of anisotropy, formability, and mechanical properties. *J. Mater. Res. Technol.* **2022**, *19*, 732–746. [CrossRef]

78. Page, M.J.; McKenzie, J.E.; Bossuyt, P.M. The PRISMA 2020 statement: An updated guideline for reporting systematic reviews. *Syst Rev.* **2021**, *10*, 89. [CrossRef]

79. Woo, D. On the complete solution of the deep-drawing problem. *Int. J. Mech. Sci.* **1968**, *10*, 83–94. [CrossRef]

80. Tseng, A.A. A generalized finite difference scheme for convection-dominated metal-forming problems. *Int. J. Numer. Methods Eng.* **1984**, *20*, 1885–1900. [CrossRef]

81. Wifi, A.S. An incremental complete solution of the stretch-forming and deep-drawing of a circular blank using a hemispherical punch. *Int. J. Mech. Sci.* **1976**, *18*, 23–31. [CrossRef]

82. Gotoh, M.; Ishise, F. A finite element analysis of rigid-plastic deformation of the flange in a deep-drawing process based on a fourth-degree yield function. *Int. J. Mech. Sci.* **1978**, *20*, 423–435. [CrossRef]

83. Wang, N.-M.; Budiansky, B. Analysis of sheet metal stamping by a finite-element method. *J. Appl. Mech.* **1978**, *45*, 73–82. [CrossRef]

84. Tang, S.; Chu, E.; Samanta, S. Finite element prediction of the deformed shape of an automotive body panel during preformed stage. *Numer. Methods Ind. Form. Process.* **1982**, 629–640.

85. Toh, C.; Kobayashi, S. Finite element process modeling of sheet metal forming of general shapes. In *Grundlagen der Umformtechnik—Stand und Entwicklungstrends/Fundamentals of Metal Forming Technique—State and Trends*; Springer: Berlin, Germany, 1983; pp. 39–56. [CrossRef]

86. Benson, D.; Hallquist, J. A simple rigid body algorithm for structural dynamics programs. *Int. J. Numer. Methods Eng.* **1986**, *22*, 723–749. [CrossRef]

87. Belytschko, T. Explicit integration of structural problems. *Finite Elem. Nonlinear Mech.* **1977**, *2*, 697–720.

88. Massoni, E.; Bellet, M.; Chenot, J.; Detraux, J.; De Baynast, C. *A Finite Element Modelling for Deep Drawing of Thin Sheet in Automotive Industry*; Springer: Berlin, Germany, 1987; pp. 719–725.

89. Wang, N.-M.; Wenner, M. Elastic-viscoplastic analyses of simple stretch forming problems. In *Mechanics of Sheet Metal Forming*; Springer: Berlin, Germany, 1978; pp. 367–402. [CrossRef]

90. Griffiths, J.; Edwardson, S.; Dearden, G.; Watkins, K. Finite Element modelling of laser forming at macro and micro scales. *Phys. Procedia* **2010**, *5*, 371–380. [CrossRef]

91. Doege, E.; Ropers, C. Berechnung der Wärmeleitung in dreidimensional geformten Blechen mit der Finite-Differenzen-Methode während eines Umformprozesses. *Forsch. Ingenieurwes.* **1999**, *65*, 169–177. [CrossRef]

92. Lee, M.G.; Kim, C.; Pavlina, E.J.; Barlat, F. Advances in Sheet Forming-Materials Modeling, Numerical Simulation, and Press Technologies. *J. Manuf. Sci. Eng. -Trans. ASME* **2011**, *133*, 061001–061012. [CrossRef]

93. Oñate, E.; Rojek, J.; Garino, C.G. NUMISTAMP: A research project for assessment of finite-element models for stamping processes. *J. Mater. Process. Technol.* **1995**, *50*, 17–38. [CrossRef]

94. Yang, D.-Y.; Jung, D.; Song, I.; Yoo, D.; Lee, J. Comparative investigation into implicit, explicit, and iterative implicit/explicit schemes for the simulation of sheet-metal forming processes. *J. Mater. Process. Technol.* **1995**, *50*, 39–53. [CrossRef]

95. Kheloufi, K.; Amara, E.H. Numerical Simulation Of Steel Plate Bending Process Using Stationary Laser Beam By A Coupled Finite Element Thermal Mechanical Analysis. AIP Conference Proceedings; American Institute of Physics: College Park, MD, USA, 2008; pp. 176–179.

96. Nakamachi, E. Sheet-forming process characterization by static-explicit anisotropic elastic-plastic finite-element simulation. *J. Mater. Process. Technol.* **1995**, *50*, 116–132. [CrossRef]

97. Mamalis, A.; Manolakos, D.; Baldoukas, A. Simulation of sheet metal forming using explicit finite-element techniques: Effect of material and forming characteristics: Part 1. Deep-drawing of cylindrical cups. *J. Mater. Process. Technol.* **1997**, *72*, 48–60. [CrossRef]

98. Jung, D.; Yoo, D.; Yang, D.-Y. A dynamic explicit/rigid-plastic finite element formulation and its application to sheet metal forming processes. *Eng. Comput.* **1995**, *12*, 707–722. [CrossRef]

99. Jung, D. Study of dynamic explicit analysis in sheet metal forming processes using faster punch velocity and mass scaling scheme. *J. Mater. Eng. Perform.* **1998**, *7*, 479–490. [CrossRef]

100. Carleer, B.; Huétink, J. Closing the gap between the workshop and numerical simulations in sheet metal forming. In *Computational Methods in Applied Sciences (Proceedings Eccomas' 96)*; Désidéri, J.-A., Hirsch, C., Le Tallec, P., Oñate, E., Pandolfi, M., Périaux, J., Stein, E., Eds.; Wiley: Hoboken, NJ, USA, 1996; pp. 554–560.

101. Finn, M.; Galbraith, P.; Wu, L.; Hallquist, J.; Lum, L.; Lin, T.-L. Use of a coupled explicit—Implicit solver for calculating spring-back in automotive body panels. *J. Mater. Process. Technol.* **1995**, *50*, 395–409. [CrossRef]

102. Micari, F.; Forcellese, A.; Fratini, L.; Gabrielli, F.; Alberti, N. Springback evaluation in fully 3-D sheet metal forming processes. *CIRP Ann.* **1997**, *46*, 167–170. [CrossRef]

103. Batoz, J.L.; Guo, Y.Q.; Mercier, F. The inverse approach with simple triangular shell elements for large strain predictions of sheet metal forming parts. *Eng. Comput.* **1998**, *15*, 864–892. [CrossRef]

104. Guo, Y.; Batoz, J.; Naceur, H.; Bouabdallah, S.; Mercier, F.; Barlet, O. Recent developments on the analysis and optimum design of sheet metal forming parts using a simplified inverse approach. *Comput. Struct.* **2000**, *78*, 133–148. [CrossRef]

105. Bostan Shirin, M.; Assempour, A. Some improvements on the unfolding inverse finite element method for simulation of deep drawing process. *Int. J. Adv. Manuf. Technol.* **2014**, *72*, 447–456. [CrossRef]

106. Azizi, R. Different implementations of inverse finite element method in sheet metal forming. *Mater. Des.* **2009**, *30*, 2975–2980. [CrossRef]

107. Na, J.; Chen, W. One step positive approach for sheet metal forming simulation based on quasi-conjugate-gradient method. *Chin. J. Mech. Eng.* **2013**, *26*, 730–736. [CrossRef]

108. Chung, W.; Kim, B.; Lee, S.; Ryu, H.; Joun, M. Finite element simulation of plate or sheet metal forming processes using tetrahedral MINI-elements. *J. Mech. Sci. Technol.* **2014**, *28*, 237–243. [CrossRef]

109. Menezes, L.; Teodosiu, C. Three-dimensional numerical simulation of the deep-drawing process using solid finite elements. *J. Mater. Process. Technol.* **2000**, *97*, 100–106. [CrossRef]

110. Park, S.; Jung, J.; Cho, W.; Jeong, B.-S.; Na, H.; Kim, S.-I.; Lee, M.-G.; Han, H.N. Predictive dual-scale finite element simulation for hole expansion failure of ferrite-bainite steel. *Int. J. Plast.* **2021**, *136*, 102900. [CrossRef]

111. Papeleux, L.; Ponthot, J.-P. Finite element simulation of springback in sheet metal forming. *J. Mater. Process. Technol.* **2002**, *125*, 785–791. [CrossRef]

112. Parente, M.; Valente, R.F.; Jorge, R.N.; Cardoso, R.P.; de Sousa, R.A. Sheet metal forming simulation using EAS solid-shell finite elements. *Finite Elem. Anal. Des.* **2006**, *42*, 1137–1149. [CrossRef]

113. De Sousa, R.A.; Yoon, J.W.; Cardoso, R.; Valente, R.F.; Gracio, J. On the use of a reduced enhanced solid-shell (RESS) element for sheet forming simulations. *Int. J. Plast.* **2007**, *23*, 490–515. [CrossRef]

114. Lee, M.; Chung, S.; Jang, S.; Joun, M. Three-dimensional simulation of forging using tetrahedral and hexahedral elements. *Finite Elem. Anal. Des.* **2009**, *45*, 745–754. [CrossRef]

115. Yoon, S.; Wu, C.-T.; Wang, H.-P.; Chen, J.-S. Efficient meshfree formulation for metal forming simulations. *J. Eng. Mater. Technol.* **2001**, *123*, 462–467. [CrossRef]

116. Cueto, E.; Chinesta, F. Meshless methods for the simulation of material forming. *Int. J. Mater. Form.* **2015**, *8*, 25–43. [CrossRef]
117. Yoon, S.; Chen, J.-S. Accelerated meshfree method for metal forming simulation. *Finite Elem. Anal. Des.* **2002**, *38*, 937–948. [CrossRef]
118. Liu, H.S.; Xing, Z.W.; Yang, Y.Y. Simulation of sheet metal forming process using reproducing kernel particle method. *Int. J. Numer. Methods Biomed. Eng.* **2010**, *26*, 1462–1476. [CrossRef]
119. Garg, S.; Pant, M. Meshfree methods: A comprehensive review of applications. *Int. J. Comput. Methods* **2018**, *15*, 1830001. [CrossRef]
120. Liu, H.; Xing, Z.; Sun, Z.; Bao, J. Adaptive multiple scale meshless simulation on springback analysis in sheet metal forming. *Eng. Anal. Bound. Elem.* **2011**, *35*, 436–451. [CrossRef]
121. Liu, H.; Fu, M. Adaptive reproducing kernel particle method using gradient indicator for elasto-plastic deformation. *Eng. Anal. Bound. Elem.* **2013**, *37*, 280–292. [CrossRef]
122. Hill, R. A theory of the yielding and plastic flow of anisotropic metals. *Proc. R. Soc. London. Ser. A. Math. Phys. Sci.* **1948**, *193*, 281–297. [CrossRef]
123. Barlat, F.; Brem, J.C.; Yoon, J.W.; Chung, K.; Dick, R.E.; Lege, D.J.; Pourgoghrat, F.; Choi, S.H.; Chu, E. Plane stress yield function for aluminum alloy sheets—part 1: Theory. *Int. J. Plast.* **2003**, *19*, 1297–1319. [CrossRef]
124. Yoshida, F.; Hamasaki, H.; Uemori, T. A user-friendly 3D yield function to describe anisotropy of steel sheets. *Int. J. Plast.* **2013**, *45*, 119–139. [CrossRef]
125. Barlat, F.; Lian, J. Plastic behavior and stretchability of sheet metals.1. A yield function for orthotropic sheets under plane-stress conditions. *Int. J. Plast.* **1989**, *5*, 51–66. [CrossRef]
126. Gotoh, M. A theory of plastic anisotropy based on a yield function of fourth order (plane stress state)—I. *Int. J. Mech. Sci.* **1977**, *19*, 505–512. [CrossRef]
127. Tong, W. A plane stress anisotropic plastic flow theory for orthotropic sheet metals. *Int. J. Plast.* **2006**, *22*, 497–535. [CrossRef]
128. Soare, S.; Yoon, J.W.; Cazacu, O. On the use of homogeneous polynomials to develop anisotropic yield functions with applications to sheet forming. *Int. J. Plast.* **2008**, *24*, 915–944. [CrossRef]
129. Hu, W. A novel quadratic yield model to describe the feature of multi-yield-surface of rolled sheet metals. *Int. J. Plast.* **2007**, *23*, 2004–2028. [CrossRef]
130. Banabic, D.; Aretz, H.; Comsa, D.; Paraianu, L. An improved analytical description of orthotropy in metallic sheets. *Int. J. Plast.* **2005**, *21*, 493–512. [CrossRef]
131. Barlat, F.; Aretz, H.; Yoon, J.W.; Karabin, M.E.; Brem, J.C.; Dick, R.E. Linear transfomation-based anisotropic yield functions. *Int. J. Plast.* **2005**, *21*, 1009–1039. [CrossRef]
132. Bron, F.; Besson, J. A yield function for anisotropic materials application to aluminum alloys. *Int. J. Plast.* **2004**, *20*, 937–963. [CrossRef]
133. Cazacu, O.; Barlat, F. Generalization of Drucker's yield criterion to orthotropy. *Math. Mech. Solids* **2001**, *6*, 613–630. [CrossRef]
134. Soare, S.; Barlat, F. Convex polynomial yield functions. *J. Mech. Phys. Solids* **2010**, *58*, 1804–1818. [CrossRef]
135. Aretz, H.; Barlat, F. New convex yield functions for orthotropic metal plasticity. *Int. J. Non Linear Mech.* **2013**, *51*, 97–111. [CrossRef]
136. Cazacu, O. New yield criteria for isotropic and textured metallic materials. *Int. J. Solids Struct.* **2018**, *139*, 200–210. [CrossRef]
137. Shi, B.; Yang, C.; Peng, Y.; Zhang, F.; Pan, F. Anisotropy of wrought magnesium alloys: A focused overview. *J. Magnes. Alloy.* **2022**, *10*, 1476–1510. [CrossRef]
138. Khan, A.S.; Yu, S. Deformation induced anisotropic responses of Ti–6Al–4V alloy. Part I: Experiments. *Int. J. Plast.* **2012**, *38*, 1–13. [CrossRef]
139. Zou, D.Q.; Li, S.H.; He, J.; Gu, B.; Li, Y.F. The deformation induced martensitic transformation and mechanical behavior of quenching and partitioning steels under complex loading process. *Mater. Sci. Eng. A-Struct. Mater. Prop. Microstruct. Process.* **2018**, *715*, 243–256. [CrossRef]
140. Hou, Y.; Min, J.; Guo, N.; Shen, Y.; Lin, J. Evolving asymmetric yield surfaces of quenching and partitioning steels: Characterization and modeling. *J. Mater. Process. Technol.* **2021**, *290*, 116979. [CrossRef]
141. Cazacu, O.; Barlat, F. A criterion for description of anisotropy and yield differential effects in pressure-insensitive metals. *Int. J. Plast.* **2004**, *20*, 2027–2045. [CrossRef]
142. Cazacu, O.; Plunkett, B.; Barlat, F. Orthotropic yield criterion for hexagonal closed packed metals. *Int. J. Plast.* **2006**, *22*, 1171–1194. [CrossRef]
143. Khan, A.S.; Yu, S.; Liu, H. Deformation induced anisotropic responses of Ti–6Al–4V alloy Part II: A strain rate and temperature dependent anisotropic yield criterion. *Int. J. Plast.* **2012**, *38*, 14–26. [CrossRef]
144. Yoon, J.W.; Lou, Y.S.; Yoon, J.; Glazoff, M.V. Asymmetric yield function based on the stress invariants for pressure sensitive metals. *Int. J. Plast.* **2014**, *56*, 184–202. [CrossRef]
145. Hu, Q.; Li, X.; Han, X.; Li, H.; Chen, J. A normalized stress invariant-based yield criterion: Modeling and validation. *Int. J. Plast.* **2017**, *99*, 248–273. [CrossRef]
146. Stoughton, T.B. A non-associated flow rule for sheet metal forming. *Int. J. Plast.* **2002**, *18*, 687–714. [CrossRef]
147. Stoughton, T.B.; Yoon, J.W. A pressure-sensitive yield criterion under a non-associated flow rule for sheet metal forming. *Int. J. Plast.* **2004**, *20*, 705–731. [CrossRef]

148. Stoughton, T.B.; Yoon, J.W. Anisotropic hardening and non-associated flow in proportional loading of sheet metals. *Int. J. Plast.* **2009**, *25*, 1777–1817. [CrossRef]

149. Min, J.; Carsley, J.E.; Lin, J.; Wen, Y.; Kuhlenkotter, B. A non-quadratic constitutive model under non-associated flow rule of sheet metals with anisotropic hardening: Modeling and experimental validation. *Int. J. Mech. Sci.* **2016**, *119*, 343–359. [CrossRef]

150. Lee, E.H.; Stoughton, T.B.; Yoon, J.W. A yield criterion through coupling of quadratic and non quadratic functions for anisotropic hardening with non associated flow rule. *Int. J. Plast.* **2017**, *99*, 120–143. [CrossRef]

151. Park, N.; Stoughton, T.B.; Yoon, J.W. A criterion for general description of anisotropic hardening considering strength differential effect with non-associated flow rule. *Int. J. Plast.* **2019**, *121*, 76–100. [CrossRef]

152. Hou, Y.; Du, K.; Abd El-Aty, A.; Lee, M.-G.; Min, J. Plastic anisotropy of sheet metals under plane strain loading: A novel non-associated constitutive model based on fourth-order polynomial functions. *Mater. Des.* **2022**, *223*, 111187. [CrossRef]

153. Lou, Y.; Zhang, C.; Zhang, S.; Yoon, J.W. A general yield function with differential and anisotropic hardening for strength modelling under various stress states with non-associated flow rule. *Int. J. Plast.* **2022**, *158*, 103414. [CrossRef]

154. Chen, Z.; Wang, Y.; Lou, Y. User-friendly anisotropic hardening function with non-associated flow rule under the proportional loadings for BCC and FCC metals. *Mech. Mater.* **2022**, *165*, 104190. [CrossRef]

155. Hou, Y.; Min, J.; Stoughton, T.B.; Lin, J.; Carsley, J.E.; Carlson, B.E. A non-quadratic pressure-sensitive constitutive model under non-associated flow rule with anisotropic hardening: Modeling and validation. *Int. J. Plast.* **2020**, *135*, 102808. [CrossRef]

156. Hu, Q.; Yoon, J.W. Analytical description of an asymmetric yield function (Yoon2014) by considering anisotropic hardening under non-associated flow rule. *Int. J. Plast.* **2021**, *140*, 102978. [CrossRef]

157. Hill, R.; Hutchinson, J.W. Differential Hardening in Sheet Metal Under Biaxial Loading: A Theoretical Framework. *J. Appl. Mech.* **1992**, *59*, S1–S9. [CrossRef]

158. Aretz, H. A simple isotropic-distortional hardening model and its application in elastic–plastic analysis of localized necking in orthotropic sheet metals. *Int. J. Plast.* **2008**, *24*, 1457–1480. [CrossRef]

159. Wang, H.; Wan, M.; Wu, X.; Yan, Y. The equivalent plastic strain-dependent Yld2000-2d yield function and the experimental verification. *Comput. Mater. Sci* **2009**, *47*, 12–22. [CrossRef]

160. Cai, Z.; Diao, K.; Wu, X.; Wan, M. Constitutive modeling of evolving plasticity in high strength steel sheets. *Int. J. Mech. Sci.* **2016**, *107*, 43–57. [CrossRef]

161. Noman, M.; Clausmeyer, T.; Barthel, C.; Svendsen, B.; Huétink, J.; Van Riel, M. Experimental characterization and modeling of the hardening behavior of the sheet steel LH800. *Mater. Sci. Eng. A* **2010**, *527*, 2515–2526. [CrossRef]

162. Teodosiu, C.; Hu, Z. Microstructure in the Continuum Modeling of Plastic Anisotropy. *Ninet. Riso Int. Symp. Mater. Sci.* **1998**, *1998*, 149–168.

163. Hou, Y.; Min, J.; Lin, J.; Lee, M.-G. Modeling stress anisotropy, strength differential, and anisotropic hardening by coupling quadratic and stress-invariant-based yield functions under non-associated flow rule. *Mech. Mater.* **2022**, *174*, 104458. [CrossRef]

164. Wagoner, R.H.; Lim, H.; Lee, M.G. Advanced Issues in springback. *Int. J. Plast.* **2013**, *45*, 3–20. [CrossRef]

165. Clausmeyer, T.; Güner, A.; Tekkaya, A.E.; Levkovitch, V.; Svendsen, B. Modeling and finite element simulation of loading-path-dependent hardening in sheet metals during forming. *Int. J. Plast.* **2014**, *63*, 64–93. [CrossRef]

166. Reyne, B.; Barlat, F. A new concept for continuum distortional plasticity. *Int. J. Plast.* **2022**, *155*, 103303. [CrossRef]

167. Prager, W. A new methods of analyzing stresses and strains in work hardening plastic solids. *J. Appl. Mech.* **1956**, *23*, 493–496. [CrossRef]

168. Armstrong, P.J.; Frederick, C. *A mathematical Representation of the Multiaxial Bauschinger Effect*; Central Electricity Generating Board [and] Berkeley Nuclear Laboratories: Berkeley, CA, USA, 1966; Volume 731.

169. Chaboche, J.L. Time-Independent Constitutive Theories for Cyclic Plasticity. *Int. J. Plast.* **1986**, *2*, 149–188. [CrossRef]

170. Yoshida, F.; Uemori, T. A model of large-strain cyclic plasticity describing the Bauschinger effect and workhardening stagnation. *Int. J. Plast.* **2002**, *18*, 661–686. [CrossRef]

171. Chaboche, J.L. A review of some plasticity and viscoplasticity constitutive theories. *Int. J. Plast.* **2008**, *24*, 1642–1693. [CrossRef]

172. Peeters, B.; Seefeldt, M.; Teodosiu, C.; Kalidindi, S.R.; Van Houtte, P.; Aernoudt, E. Work-hardening/softening behaviour of b.c.c. polycrystals during changing strain paths: I. An integrated model based on substructure and texture evolution, and its prediction of the stress–strain behaviour of an IF steel during two-stage strain paths. *Acta Mater.* **2001**, *49*, 1607–1619. [CrossRef]

173. Wang, J.; Levkovitch, V.; Svendsen, B. Modeling and simulation of directional hardening in metals during non-proportional loading. *J. Mater. Process. Technol.* **2006**, *177*, 430–432. [CrossRef]

174. Wang, J.; Levkovitch, V.; Reusch, F.; Svendsen, B.; Huétink, J.; van Riel, M. On the modeling of hardening in metals during non-proportional loading. *Int. J. Plast.* **2008**, *24*, 1039–1070. [CrossRef]

175. Mánik, T.; Holmedal, B.; Hopperstad, O.S. Strain-path change induced transients in flow stress, work hardening and r-values in aluminum. *Int. J. Plast.* **2015**, *69*, 1–20. [CrossRef]

176. Barlat, F.; Gracio, J.J.; Lee, M.G.; Rauch, E.F.; Vincze, G. An alternative to kinematic hardening in classical plasticity. *Int. J. Plast.* **2011**, *27*, 1309–1327. [CrossRef]

177. Barlat, F.; Ha, J.J.; Gracio, J.J.; Lee, M.G.; Rauch, E.F.; Vincze, G. Extension of homogeneous anisotropic hardening model to cross-loading with latent effects. *Int. J. Plast.* **2013**, *46*, 130–142. [CrossRef]

178. Barlat, F.; Vincze, G.; Gracio, J.J.; Lee, M.G.; Rauch, E.F.; Tome, C.N. Enhancements of homogenous anisotropic hardening model and application to mild and dual-phase steels. *Int. J. Plast.* **2014**, *58*, 201–218. [CrossRef]

179. Barlat, F.; Yoon, S.Y.; Lee, S.Y.; Wi, M.S.; Kim, J.H. Distortional plasticity framework with application to advanced high strength steel. *Int. J. Solids Struct.* **2020**, *202*, 947–962. [CrossRef]

180. Fu, J.W.; Barlat, F.; Kim, J.H. Parameter identification of the homogeneous anisotropic hardening model using the virtual fields method. *Int. J. Mater. Form.* **2016**, *9*, 691–696. [CrossRef]

181. Liao, J.; Sousa, J.A.; Lopes, A.B.; Xue, X.; Barlat, F.; Pereira, A.B. Mechanical, microstructural behaviour and modelling of dual phase steels under complex deformation paths. *Int. J. Plast.* **2017**, *93*, 269–290. [CrossRef]

182. Lee, J.W.; Lee, M.G.; Barlat, F. Finite element modeling using homogeneous anisotropic hardening and application to spring-back prediction. *Int. J. Plast.* **2012**, *29*, 13–41. [CrossRef]

183. Lee, E.H.; Choi, H.; Stoughton, T.B.; Yoon, J.W. Combined anisotropic and distortion hardening to describe directional response with Bauschinger effect. *Int. J. Plast.* **2019**, *122*, 73–88. [CrossRef]

184. Hou, Y.; Lee, M.-G.; Lin, J.; Min, J. Experimental characterization and modeling of complex anisotropic hardening in quenching and partitioning (Q&P) steel subject to biaxial non-proportional loadings. *Int. J. Plast.* **2022**, *156*, 103347. [CrossRef]

185. Lee, J.; Lee, J.-Y.; Barlat, F.; Wagoner, R.H.; Chung, K.; Lee, M.-G. Extension of quasi-plastic–elastic approach to incorporate complex plastic flow behavior—application to springback of advanced high-strength steels. *Int. J. Plast.* **2013**, *45*, 140–159. [CrossRef]

186. He, W.; Lin, T.; Liu, Q. Experiments and constitutive modeling of deformation behavior of a magnesium sheet during two-step loading. *Int. J. Solids Struct.* **2018**, *147*, 52–60. [CrossRef]

187. Lee, J.; Bong, H.J.; Kim, D.; Lee, M.G. Modeling differential permanent softening under strain-path changes in sheet metals using a modified distortional hardening model. *Int. J. Plast.* **2020**, *133*, 102789. [CrossRef]

188. François, M. A plasticity model with yield surface distortion for non proportional loading. *Int. J. Plast.* **2001**, *17*, 703–717. [CrossRef]

189. Feigenbaum, H.P.; Dafalias, Y.F. Directional distortional hardening in metal plasticity within thermodynamics. *Int. J. Solids Struct.* **2007**, *44*, 7526–7542. [CrossRef]

190. Rokhgireh, H.; Nayebi, A.; Chaboche, J.L. Application of a new distortional yield surface model in cyclic uniaxial and multiaxial loading. *Int. J. Solids Struct.* **2017**, *110–111*, 219–238. [CrossRef]

191. Qin, J.S.; Holmedal, B.; Hopperstad, O.S. A combined isotropic, kinematic and distortional hardening model for aluminum and steels under complex strain-path changes. *Int. J. Plast.* **2018**, *101*, 156–169. [CrossRef]

192. Holmedal, B. Bauschinger effect modelled by yield surface distortions. *Int. J. Plast.* **2019**, *123*, 86–100. [CrossRef]

193. Ziegler, H. A modification of Prager's hardening rule. *Q. Appl. Math.* **1959**, *17*, 55–65. [CrossRef]

194. Hu, Q.; Yoon, J.W. Anisotropic distortional hardening based on deviatoric stress invariants under non-associated flow rule. *Int. J. Plast.* **2022**, *151*, 103214. [CrossRef]

195. Feigenbaum, H.P.; Dugdale, J.; Dafalias, Y.F.; Kourousis, K.I.; Plesek, J. Multiaxial ratcheting with advanced kinematic and directional distortional hardening rules. *Int. J. Solids Struct.* **2012**, *49*, 3063–3076. [CrossRef]

196. Zhang, W.; Yang, H.C.; Zhuang, X.C.; Zhao, Z. A nonassociated constitutive model describing transients in material behaviour induced by strain-path changes. *Mater. Today Commun.* **2022**, *30*, 103137. [CrossRef]

197. Zhang, W.; Zhuang, X.C.; Zhang, Y.; Zhao, Z. An enhanced Francois distortional yield model: Theoretical framework and experimental validation. *Int. J. Plast.* **2020**, *127*, 102643. [CrossRef]

198. Holmedal, B.; Hopperstad, O.S.; Berstad, T. Modeling Transients Related to Strain-path Changes. In Proceedings of the 12th International Conference on Aluminium Alloys, Yokohama, Japan, 5 September 2010.

199. Wang, W.; Wen, W. Modeling in Crystal Plasticity: From Theory to Application. In *Encyclopedia of Materials: Metals and Alloys*; Caballero, F.G., Ed.; Elsevier: Oxford, UK, 2022. [CrossRef]

200. Roters, F.; Eisenlohr, P.; Hantcherli, L.; Tjahjanto, D.D.; Bieler, T.R.; Raabe, D. Overview of constitutive laws, kinematics, homogenization and multiscale methods in crystal plasticity finite-element modeling: Theory, experiments, applications. *Acta Mater.* **2010**, *58*, 1152–1211. [CrossRef]

201. Lebensohn, R.A.; Rollett, A.D. Spectral methods for full-field micromechanical modelling of polycrystalline materials. *Comput. Mater. Sci.* **2020**, *173*, 109336. [CrossRef]

202. Zhang, H.; Diehl, M.; Roters, F.; Raabe, D. A virtual laboratory using high resolution crystal plasticity simulations to determine the initial yield surface for sheet metal forming operations. *Int. J. Plast.* **2016**, *80*, 111–138. [CrossRef]

203. Han, F.; Diehl, M.; Roters, F.; Raabe, D. Using spectral-based representative volume element crystal plasticity simulations to predict yield surface evolution during large scale forming simulations. *J. Mater. Process. Technol.* **2020**, *277*, 116449. [CrossRef]

204. Wang, H.; Raeisinia, B.; Wu, P.D.; Agnew, S.R.; Tomé, C.N. Evaluation of self-consistent polycrystal plasticity models for magnesium alloy AZ31B sheet. *Int. J. Solids Struct.* **2010**, *47*, 2905–2917. [CrossRef]

205. Habib, S.A.; Khan, A.S.; Gnäupel-Herold, T.; Lloyd, J.T.; Schoenfeld, S.E. Anisotropy, tension-compression asymmetry and texture evolution of a rare-earth-containing magnesium alloy sheet, ZEK100, at different strain rates and temperatures: Experiments and modeling. *Int. J. Plast.* **2017**, *95*, 163–190. [CrossRef]

206. Singh, J.; Kim, M.-S.; Choi, S.-H. The effect of initial texture on micromechanical deformation behaviors in Mg alloys under a mini-V-bending test. *Int. J. Plast.* **2019**, *117*, 33–57. [CrossRef]

207. Bong, H.J.; Hu, X.; Sun, X.; Ren, Y. Mechanism-based constitutive modeling of ZEK100 magnesium alloy with crystal plasticity and in-situ HEXRD experiment. *Int. J. Plast.* **2019**, *113*, 35–51. [CrossRef]

208. Qiao, H.; Wu, P.D.; Guo, X.Q.; Agnew, S.R. A new empirical equation for termination of twinning in magnesium alloys. *Scr. Mater.* **2016**, *120*, 71–75. [CrossRef]

209. Proust, G.; Tomé, C.N.; Jain, A.; Agnew, S.R. Modeling the effect of twinning and detwinning during strain-path changes of magnesium alloy AZ31. *Int. J. Plast.* **2009**, *25*, 861–880. [CrossRef]

210. Hama, T.; Tanaka, Y.; Uratani, M.; Takuda, H. Deformation behavior upon two-step loading in a magnesium alloy sheet. *Int. J. Plast.* **2016**, *82*, 283–304. [CrossRef]

211. Wang, H.; Wu, P.D.; Tomé, C.N.; Wang, J. A constitutive model of twinning and detwinning for hexagonal close packed polycrystals. *Mater. Sci. Eng. A* **2012**, *555*, 93–98. [CrossRef]

212. Hama, T.; Suzuki, T.; Hatakeyama, S.; Fujimoto, H.; Takuda, H. Role of twinning on the stress and strain behaviors during reverse loading in rolled magnesium alloy sheets. *Mater. Sci. Eng. A* **2018**, *725*, 8–18. [CrossRef]

213. Wang, H.; Sun, X.; Kurukuri, S.; Worswick, M.J.; Li, D.Y.; Peng, Y.H.; Wu, P.D. The strain rate sensitive and anisotropic behavior of rare-earth magnesium alloy ZEK100 sheet. *J. Magnes. Alloy.* **2021**. [CrossRef]

214. Wang, H.; Wu, P.; Kurukuri, S.; Worswick, M.J.; Peng, Y.; Tang, D.; Li, D. Strain rate sensitivities of deformation mechanisms in magnesium alloys. *Int. J. Plast.* **2018**, *107*, 207–222. [CrossRef]

215. Ayoub, G.; Rodrigez, A.K.; Shehadeh, M.; Kridli, G.; Young, J.P.; Zbib, H. Modelling the rate and temperature-dependent behaviour and texture evolution of the Mg AZ31B alloy TRC sheets. *Philos. Mag.* **2018**, *98*, 262–294. [CrossRef]

216. Bong, H.J.; Hu, X.; Sun, X.; Ren, Y. Temperature-dependent constitutive modeling of a magnesium alloy ZEK100 sheet using crystal plasticity models combined with in situ high-energy X-ray diffraction experiment. *J. Magnes. Alloy.* **2022**, *10*, 2801–2816. [CrossRef]

217. Bong, H.J.; Lee, J.; Lee, M.-G. Modeling crystal plasticity with an enhanced twinning–detwinning model to simulate cyclic behavior of AZ31B magnesium alloy at various temperatures. *Int. J. Plast.* **2022**, *150*, 103190. [CrossRef]

218. Sun, F.; Liu, P.; Liu, W. Multi-level deep drawing simulations of AA3104 aluminium alloy using crystal plasticity finite element modelling and phenomenological yield function. *Adv. Mech. Eng.* **2021**, *13*, 16878140211001203. [CrossRef]

219. Engler, O.; Aretz, H. A virtual materials testing approach to calibrate anisotropic yield functions for the simulation of earing during deep drawing of aluminium alloy sheet. *Mater. Sci. Eng. A* **2021**, *818*, 141389. [CrossRef]

220. Chen, S.F.; Li, D.Y.; Zhang, S.H.; Han, H.N.; Lee, H.W.; Lee, M.G. Modelling continuous dynamic recrystallization of aluminum alloys based on the polycrystal plasticity approach. *Int. J. Plast.* **2020**, *131*, 102710. [CrossRef]

221. Li, Y.; Gu, B.; Jiang, S.; Liu, Y.; Shi, Z.; Lin, J. A CDRX-based material model for hot deformation of aluminium alloys. *Int. J. Plast.* **2020**, *134*, 102844. [CrossRef]

222. Chen, F.; Tian, X.; Wu, G.; Zhu, H.; Ou, H.; Cui, Z. Coupled quantitative modeling of microstructural evolution and plastic flow during continuous dynamic recrystallization. *Int. J. Plast.* **2022**, *156*, 103372. [CrossRef]

223. Kim, J.H.; Kim, D.; Barlat, F.; Lee, M.-G. Crystal plasticity approach for predicting the Bauschinger effect in dual-phase steels. *Mater. Sci. Eng. A* **2012**, *539*, 259–270. [CrossRef]

224. Cai, Z.; Meng, B.; Wan, M.; Wu, X.; Fu, M. A modified yield function for modeling of the evolving yielding behavior and micro-mechanism in biaxial deformation of sheet metals. *Int. J. Plast.* **2020**, *129*, 102707. [CrossRef]

225. Chen, S.-F.; Bandyopadhyay, K.; Basak, S.; Hwang, B.; Shim, J.-H.; Lee, J.; Lee, M.-G. Predictive integrated numerical approach for modeling spatio-temporal microstructure evolutions and grain size dependent phase transformations in steels. *Int. J. Plast.* **2021**, *139*, 102952. [CrossRef]

226. Park, J.; Lee, K.; Kang, J.H.; Kang, J.Y.; Hong, S.H.; Kwon, S.W.; Lee, M.G. Hierarchical microstructure based crystal plasticity-continuum damage mechanics approach: Model development and validation of rolling contact fatigue behavior. *Int. J. Plast.* **2021**, *143*, 103025. [CrossRef]

227. Gui, Y.; An, D.; Han, F.; Lu, X.; Kang, G.; Zhang, X. Multiple-mechanism and microstructure-based crystal plasticity modeling for cyclic shear deformation of TRIP steel. *Int. J. Mech. Sci.* **2022**, *222*, 107269. [CrossRef]

228. Lee, M.-G.; Kim, S.-J.; Han, H.N. Crystal plasticity finite element modeling of mechanically induced martensitic transformation (MIMT) in metastable austenite. *Int. J. Plast.* **2010**, *26*, 688–710. [CrossRef]

229. Park, T.; Hector Jr, L.G.; Hu, X.; Abu-Farha, F.; Fellinger, M.R.; Kim, H.; Esmaeilpour, R.; Pourboghrat, F. Crystal Plasticity Modeling of 3rd Generation Multi-phase AHSS with Martensitic Transformation. *Int. J. Plast.* **2019**, *120*, 1–46. [CrossRef]

230. Connolly, D.S.; Kohar, C.P.; Muhammad, W.; Hector, L.G.; Mishra, R.K.; Inal, K. A coupled thermomechanical crystal plasticity model applied to Quenched and Partitioned steel. *Int. J. Plast.* **2020**, *133*, 102757. [CrossRef]

231. Yang, H.; Wang, H.; Yang, Z.; Huang, Y.; Li, D.; Peng, Y.; Wu, P. In situ neutron diffraction and crystal plasticity analysis on Q&P1180 steel during plastic deformation. *Mater. Sci. Eng. A* **2021**, *802*, 140425. [CrossRef]

232. Connolly, D.S.; Kohar, C.P.; Inal, K. A novel crystal plasticity model incorporating transformation induced plasticity for a wide range of strain rates and temperatures. *Int. J. Plast.* **2022**, *152*, 103188. [CrossRef]

233. Kim, H.; Barlat, F.; Lee, Y.; Bin Zaman, S.; Lee, C.S.; Jeong, Y. A crystal plasticity model for describing the anisotropic hardening behavior of steel sheets during strain-path changes. *Int. J. Plast.* **2018**, *111*, 85–106. [CrossRef]

234. Bong, H.; Lee, J.; Lee, M.-G. Prediction of mechanical behaviour of an ultra-thin sheet metal under non-proportional loading using a crystal plasticity model. In *IOP Conference Series: Materials Science and Engineering*; IOP Publishing: Bristol, England, 2019; p. 012002.

235. Raj, A.; Verma, R.K.; Singh, P.K.; Shamshoddin, S.; Biswas, P.; Narasimhan, K. Experimental and numerical investigation of differential hardening of cold rolled steel sheet under non-proportional loading using biaxial tensile test. *Int. J. Plast.* **2022**, *154*, 103297. [CrossRef]

236. Wroński, M.; Kumar, M.A.; McCabe, R.J.; Wierzbanowski, K.; Tomé, C.N. Deformation behavior of CP-titanium under strain path changes: Experiment and crystal plasticity modeling. *Int. J. Plast.* **2022**, *148*, 103129. [CrossRef]

237. Sharma, R.; Sargeant, D.; Daroju, S.; Kenezevic, M.; Miles, M.P.; Fullwood, D.T. Multi-strain path deformation behavior of AA6016-T4: Experiments and crystal plasticity modeling. *Int. J. Solids Struct.* **2022**, *244–245*, 111536. [CrossRef]

238. Bong, H.J.; Lee, J.; Lee, M.-G.; Kim, D. Identification of mechanical responses of steel sheets under non-proportional loadings using dislocation-density based crystal plasticity model. *Int. J. Mech. Sci.* **2019**, *155*, 461–474. [CrossRef]

239. Mozaffar, M.; Bostanabad, R.; Chen, W.; Ehmann, K.; Cao, J.; Bessa, M.A. Deep learning predicts path-dependent plasticity. *Proc. Natl. Acad. Sci. USA* **2019**, *116*, 26414–26420. [CrossRef] [PubMed]

240. Brosius, A.; Küsters, N.; Lenzen, M. New method for stress determination based on digital image correlation data. *CIRP Ann.* **2018**, *67*, 269–272. [CrossRef]

241. Yin, Q.; Zillmann, B.; Suttner, S.; Gerstein, G.; Biasutti, M.; Tekkaya, A.E.; Wagner, M.F.-X.; Merklein, M.; Schaper, M.; Halle, T. An experimental and numerical investigation of different shear test configurations for sheet metal characterization. *Int. J. Solids Struct.* **2014**, *51*, 1066–1074. [CrossRef]

242. *ASTM-E8*; Standard Test Methods for Tension Testing of Metallic Materials. ASTM International: West Conshohocken, PA, USA, 2013.

243. Steglich, D.; Brocks, W.; Bohlen, J.; Barlat, F. Modelling direction-dependent hardening in magnesium sheet forming simulations. *Int. J. Mater. Form.* **2011**, *4*, 243–253. [CrossRef]

244. Yang, Y.F.; He, Z.R.; Ma, J.; Yang, H.; Min, J.Y.; Zang, S.L.; Li, H. Evolving asymmetric and anisotropic hardening of CP-Ti sheets under monotonic and reverse loading: Characterization and modeling. *Int. J. Plast.* **2022**, *159*, 103445. [CrossRef]

245. Boger, R.K.; Wagoner, R.H.; Barlat, F.; Lee, M.G.; Chung, K. Continuous, large strain, tension/compression testing of sheet material. *Int. J. Plast.* **2005**, *21*, 2319–2343. [CrossRef]

246. Kuwabara, T.; Kumano, Y.; Ziegelheim, J.; Kurosaki, I. Tension–compression asymmetry of phosphor bronze for electronic parts and its effect on bending behavior. *Int. J. Plast.* **2009**, *25*, 1759–1776. [CrossRef]

247. Cao, J.; Lee, W.; Cheng, H.S.; Seniw, M.; Wang, H.P.; Chung, K. Experimental and numerical investigation of combined isotropic-kinematic hardening behavior of sheet metals. *Int. J. Plast.* **2009**, *25*, 942–972. [CrossRef]

248. Hou, Y.; Min, J.; Guo, N.; Lin, J.; Carsley, J.E.; Stoughton, T.B.; Traphöner, H.; Clausmeyer, T.; Tekkaya, A.E. Investigation of evolving yield surfaces of dual-phase steels. *J. Mater. Process. Technol.* **2021**, *287*, 116314. [CrossRef]

249. Hou, Y.; Zhang, X.; Min, J.; Lee, M.-g. Plastic deformation of ultra-thin pure titanium sheet subject to tension-compression loadings. In *IOP Conference Series: Materials Science and Engineering*; IOP Publishing: Bristol, England, 2022; Volume 1270, p. 012020. [CrossRef]

250. Abedini, A.; Butcher, C.; Rahmaan, T.; Worswick, M.J. Evaluation and calibration of anisotropic yield criteria in shear Loading: Constraints to eliminate numerical artefacts. *Int. J. Solids Struct.* **2018**, *151*, 118–134. [CrossRef]

251. Bouvier, S.; Haddadi, H.; Levee, P.; Teodosiu, C. Simple shear tests: Experimental techniques and characterization of the plastic anisotropy of rolled sheets at large strains. *J. Mater. Process. Technol.* **2006**, *172*, 96–103. [CrossRef]

252. *ASTM-B831-93*; Standard Test Method for Shear Testing of Thin Aluminum Alloy Products. ASTM International: West Conshohocken, PA, USA, 2004.

253. Merklein, M.; Biasutti, M. Forward and reverse simple shear test experiments for material modeling in forming simulations. In Proceedings of the 10th International Conference on Technology of Plasticity, ICTP, Aachen, Germany, 25–30 September 2011; pp. 702–707.

254. Beese, A.M.; Mohr, D. Effect of stress triaxiality and Lode angle on the kinetics of strain-induced austenite-to-martensite transformation. *Acta Mater.* **2011**, *59*, 2589–2600. [CrossRef]

255. An, Y.G.; Vegter, H.; Heijne, J. Development of simple shear test for the measurement of work hardening. *J. Mater. Process. Technol.* **2009**, *209*, 4248–4254. [CrossRef]

256. Zillmann, B.; Clausmeyer, T.; Bargmann, S.; Lampke, T.; Wagner, M.-X.; Halle, T. Validation of simple shear tests for parameter identification considering the evolution of plastic anisotropy. *Tech. Mechanik. Sci. J. Fundam. Appl. Eng. Mech.* **2012**, *32*, 622–630.

257. Marciniak, Z. Influence of the sign change of the load on the strain hardening curve of a copper test subject to torsion. *Arch. Mech. Stosow.* **1961**, *13*, 743–751.

258. Tekkaya, A.; Pöhlandt, K.; Lange, K. Determining stress-strain curves of sheet metal in the plane torsion test. *CIRP Ann.* **1982**, *31*, 171–174. [CrossRef]

259. Brosius, A.; Yin, Q.; Güner, A.; Tekkaya, A. A new shear test for sheet metal characterization. *Steel Res. Int.* **2011**, *82*, 323–328. [CrossRef]

260. Yin, Q.; Tekkaya, A.E.; Traphoner, H. Determining cyclic flow curves using the in-plane torsion test. *CIRP Ann. -Manuf. Technol.* **2015**, *64*, 261–264. [CrossRef]

261. Traphöner, H.; Clausmeyer, T.; Tekkaya, A.E. Material characterization for plane and curved sheets using the in-plane torsion test—An overview. *J. Mater. Process. Technol.* **2018**, *257*, 278–287. [CrossRef]

262. Atkinson, M. Accurate determination of biaxial stress-strain relationships from hydraulic bulging tests of sheet metals. *Int. J. Mech. Sci.* **1997**, *39*, 761–769. [CrossRef]
263. Zhang, S.; Leotoing, L.; Guines, D.; Thuillier, S.; Zang, S.-L. Calibration of anisotropic yield criterion with conventional tests or biaxial test. *Int. J. Mech. Sci.* **2014**, *85*, 142–151. [CrossRef]
264. *ISO16808*; Metallic Materials-Sheet and Strip-Determination of Biaxial Stress-Strain Curve by Means of Bulge Test with Optical Measuring Systems. ISO: Geneva, Switzerland, 2014.
265. Siegert, K.; Jäger, S.; Vulcan, M. Pneumatic bulging of magnesium AZ 31 sheet metals at elevated temperatures. *CIRP Ann.* **2003**, *52*, 241–244. [CrossRef]
266. Nasser, A.; Yadav, A.; Pathak, P.; Altan, T. Determination of the flow stress of five AHSS sheet materials (DP600, DP780, DP780-CR, DP780-HY and TRIP780) using the uniaxial tensile and the biaxial Viscous Pressure Bulge (VPB) tests. *J. Mater. Process. Technol.* **2010**, *210*, 429–436. [CrossRef]
267. Yoshida, K. Evaluation of stress and strain measurement accuracy in hydraulic bulge test with the aid of finite-element analysis. *ISIJ Int.* **2013**, *53*, 86–95. [CrossRef]
268. Min, J.; Stoughton, T.B.; Carsley, J.E.; Carlson, B.E.; Lin, J.P.; Gao, X.L. Accurate characterization of biaxial stress-strain response of sheet metal from bulge testing. *Int. J. Plast.* **2017**, *94*, 192–213. [CrossRef]
269. Lafilé, V.; Galpin, B.; Mahéo, L.; Roth, C.C.; Grolleau, V. Toward the use of small size bulge tests: Numerical and experimental study at small bulge diameter to sheet thickness ratios. *J. Mater. Process. Technol.* **2021**, *291*, 117019. [CrossRef]
270. Lazarescu, L.; Nicodim, I.P.; Comsa, D.S.; Banabic, D. A procedure for the evaluation of flow stress of sheet metal by hydraulic bulge test using elliptical dies. In *Key Engineering Materials*; Trans Tech Publications Ltd: Zurich, Switzerland, 2012; pp. 107–112.
271. Williams, B.W.; Boyle, K.P. Characterization of anisotropic yield surfaces for titanium sheet using hydrostatic bulging with elliptical dies. *Int. J. Mech. Sci.* **2016**, *114*, 315–329. [CrossRef]
272. Lenzen, M.; Merklein, M. Improvement of Numerical Modelling Considering Plane Strain Material Characterization with an Elliptic Hydraulic Bulge Test. *J. Manuf. Mater. Process.* **2018**, *2*, 6. [CrossRef]
273. Rossi, M.; Lattanzi, A.; Morichelli, L.; Martins, J.M.P.; Thuillier, S.; Andrade-Campos, A.; Coppieters, S. Testing methodologies for the calibration of advanced plasticity models for sheet metals: A review. *Strain* **2022**, *58*, e12426. [CrossRef]
274. He, Z.; Zhang, K.; Lin, Y.; Yuan, S. An accurate determination method for constitutive model of anisotropic tubular materials with DIC-based controlled biaxial tensile test. *Int. J. Mech. Sci.* **2020**, *181*, 105715. [CrossRef]
275. Kuwabara, T.; Sugawara, F. Multiaxial tube expansion test method for measurement of sheet metal deformation behavior under biaxial tension for a large strain range. *Int. J. Plast.* **2013**, *45*, 103–118. [CrossRef]
276. Nazari Tiji, S.A.; Park, T.; Asgharzadeh, A.; Kim, H.; Athale, M.; Kim, J.H.; Pourboghrat, F. Characterization of yield stress surface and strain-rate potential for tubular materials using multiaxial tube expansion test method. *Int. J. Plast.* **2020**, *133*, 102838. [CrossRef]
277. Kuwabara, T. Advances in experiments on metal sheets and tubes in support of constitutive modeling and forming simulations. *Int. J. Plast.* **2007**, *23*, 385–419. [CrossRef]
278. Müller, W.; Pöhlandt, K. New experiments for determining yield loci of sheet metal. *J. Mater. Process. Technol.* **1996**, *60*, 643–648. [CrossRef]
279. Kuwabara, T.; Van Bael, A.; Iizuka, E. Measurement and analysis of yield locus and work hardening characteristics of steel sheets wtih different r-values. *Acta Mater.* **2002**, *50*, 3717–3729. [CrossRef]
280. Kuwabara, T.; Ikeda, S.; Kuroda, K. Measurement and analysis of differential work hardening in cold-rolled steel sheet under biaxial tension. *J. Mater. Process. Technol.* **1998**, *80–81*, 517–523. [CrossRef]
281. Hanabusa, Y.; Takizawa, H.; Kuwabara, T. Numerical verification of a biaxial tensile test method using a cruciform specimen. *J. Mater. Process. Technol.* **2013**, *213*, 961–970. [CrossRef]
282. *ISO16842*; Metallic Materials-Sheet and Strip-Biaxial Tensile Testing Method Using a Cruciform Test Piece. ISO: Geneva, Switzerland, 2014.
283. Liu, W.; Guines, D.; Leotoing, L.; Ragneau, E. Identification of sheet metal hardening for large strains with an in-plane biaxial tensile test and a dedicated cross specimen. *Int. J. Mech. Sci.* **2015**, *101–102*, 387–398. [CrossRef]
284. Zhang, R.; Shao, Z.; Shi, Z.; Dean, T.A.; Lin, J. Effect of cruciform specimen design on strain paths and fracture location in equi-biaxial tension. *J. Mater. Process. Technol.* **2021**, *289*, 116932. [CrossRef]
285. Mitukiewicz, G.; Głogowski, M. Cruciform specimen to obtain higher plastic deformation in a gauge region. *J. Mater. Process. Technol.* **2016**, *227*, 11–15. [CrossRef]
286. Hou, Y.; Min, J.; Lin, J.; Carsley, J.E.; Stoughton, T.B. Cruciform specimen design for large plastic strain during biaxial tensile testing. In *Journal of Physics: Conference Series*; IOP Publishing: Bristol, England, 2018; p. 012160.
287. Hou, Y.; Min, J.; Lin, J.; Carsley, J.E.; Stoughton, T.B. Plastic instabilities in AA5754-O under various stress states. In *IOP Conference Series: Materials Science and Engineering*; IOP Publishing: Bristol, England, 2018; p. 012050.
288. Haddag, B.; Balan, T.; Abed-Meraim, F. Investigation of advanced strain-path dependent material models for sheet metal forming simulations. *Int. J. Plast.* **2007**, *23*, 951–979. [CrossRef]
289. Zang, S.L.; Guo, C.; Thuillier, S.; Lee, M.G. A model of one-surface cyclic plasticity and its application to springback prediction. *Int. J. Mech. Sci.* **2011**, *53*, 425–435. [CrossRef]

290. Hérault, D.; Thuillier, S.; Lee, S.-Y.; Manach, P.-Y.; Barlat, F. Calibration of a strain path change model for a dual phase steel. *Int. J. Mech. Sci.* **2021**, *194*, 106217. [CrossRef]

291. Lin, J.; Hou, Y.; Min, J.; Tang, H.; Carsley, J.E.; Stoughton, T.B. Effect of constitutive model on springback prediction of MP980 and AA6022-T4. *Int. J. Mater. Form.* **2020**, *13*, 1–13. [CrossRef]

292. Liu, Z.; Hou, Y.; He, R.; Ye, Y.; Niu, C.; Min, J. Machine learning for extending capability of mechanical characterization to improve springback prediction of a quenching and partitioning steel. *J. Mater. Process. Technol.* **2022**, *308*, 117737. [CrossRef]

293. Yoon, J.W.; Barlat, F.; Gracio, J.J.; Rauch, E. Anisotropic strain hardening behavior in simple shear for cube textured aluminum alloy sheets. *Int. J. Plast.* **2005**, *21*, 2426–2447. [CrossRef]

294. Choi, J.S.; Lee, J.W.; Kim, J.H.; Barlat, F.; Lee, M.G.; Kim, D. Measurement and modeling of simple shear deformation under load reversal: Application to advanced high strength steels. *Int. J. Mech. Sci.* **2015**, *98*, 144–156. [CrossRef]

295. Yoshida, F.; Urabe, M.; Toropov, V.V. Identification of material parameters in constitutive model for sheet metals from cyclic bending tests. *Int. J. Mech. Sci.* **1998**, *40*, 237–249. [CrossRef]

296. Yoshida, F.; Urabe, M.; Hino, R.; Toropov, V.V. Inverse approach to identification of material parameters of cyclic elasto-plasticity for component layers of a bimetallic sheet. *Int. J. Plast.* **2003**, *19*, 2149–2170. [CrossRef]

297. Eggertsen, P.A.; Mattiasson, K. On the modelling of the bending–unbending behaviour for accurate springback predictions. *Int. J. Mech. Sci.* **2009**, *51*, 547–563. [CrossRef]

298. Zang, S.-l.; Lee, M.-G.; Sun, L.; Kim, J.H. Measurement of the Bauschinger behavior of sheet metals by three-point bending springback test with pre-strained strips. *Int. J. Plast.* **2014**, *59*, 84–107. [CrossRef]

299. Choi, J.H.; Zang, S.L.; Lee, M.G.; Kim, J.H.; Barlat, F. Determining the coefficients of a homogeneous anisotropic hardening model for ultrathin steel sheets. *Int. J. Mech. Sci.* **2019**, *157–158*, 428–438. [CrossRef]

300. Ha, J.; Lee, M.G.; Barlat, F. Strain hardening response and modeling of EDDQ and DP780 steel sheet under non-linear strain path. *Mech. Mater.* **2013**, *64*, 11–26. [CrossRef]

301. Wen, W.; Borodachenkova, M.; Tomé, C.; Vincze, G.; Rauch, E.; Barlat, F.; Grácio, J. Mechanical behavior of Mg subjected to strain path changes: Experiments and modeling. *Int. J. Plast.* **2015**, *73*, 171–183. [CrossRef]

302. Zaman, S.B.; Barlat, F.; Kim, J.-H. Deformation-induced anisotropy of uniaxially prestrained steel sheets. *Int. J. Solids Struct.* **2018**, *134*, 20–29. [CrossRef]

303. Wi, M.S.; Lee, S.Y.; Kim, J.H.; Kim, J.M.; Barlat, F. Experimental and theoretical plasticity analyses of steel materials deformed under a nonlinear strain path. *Int. J. Mech. Sci.* **2020**, *182*, 105770. [CrossRef]

304. Lee, S.Y.; Kim, J.M.; Kim, J.H.; Barlat, F. Validation of homogeneous anisotropic hardening model using non-linear strain path experiments. *Int. J. Mech. Sci.* **2020**, *183*, 105769. [CrossRef]

305. Andrade-Campos, A.; Coppieters, S.; Strano, M. Optimization and inverse analysis in metal forming: Scientific state-of-the-art and recent trends. *Int. J. Mater. Form.* **2022**, *15*, 1–23. [CrossRef]

306. Pierron, F.; Grédiac, M. Towards Material Testing 2.0. A review of test design for identification of constitutive parameters from full-field measurements. *Strain* **2021**, *57*, e12370. [CrossRef]

307. Kim, J.H.; Serpantie, A.; Barlat, F.; Pierron, F.; Lee, M.G. Characterization of the post-necking strain hardening behavior using the virtual fields method. *Int. J. Solids Struct.* **2013**, *50*, 3829–3842. [CrossRef]

308. Zhao, K.; Wang, L.; Chang, Y.; Yan, J. Identification of post-necking stress-strain curve for sheet metals by inverse method. *Mech. Mater.* **2016**, *92*, 107–118. [CrossRef]

309. Pham, Q.T.; Nguyen-Thoi, T.; Ha, J.; Kim, Y.-S. Hybrid fitting-numerical method for determining strain-hardening behavior of sheet metals. *Mech. Mater.* **2021**, *161*, 104031. [CrossRef]

310. Lou, Y.; Zhang, S.; Yoon, J.W. Strength modeling of sheet metals from shear to plane strain tension. *Int. J. Plast.* **2020**, *134*, 102813. [CrossRef]

311. Zhang, C.; Lou, Y.; Zhang, S.; Clausmeyer, T.; Tekkaya, A.E.; Fu, L.; Chen, Q.; Zhang, Q. Large strain flow curve identification for sheet metals under complex stress states. *Mech. Mater.* **2021**, *161*, 103997. [CrossRef]

312. Grédiac, M.; Pierron, F. Applying the Virtual Fields Method to the identification of elasto-plastic constitutive parameters. *Int. J. Plast.* **2006**, *22*, 602–627. [CrossRef]

313. Rossi, M.; Pierron, F.; Štamborská, M. Application of the virtual fields method to large strain anisotropic plasticity. *Int. J. Solids Struct.* **2016**, *97–98*, 322–335. [CrossRef]

314. Kim, C.; Lee, M.-G. Finite element-based virtual fields method with pseudo-real deformation fields for identifying constitutive parameters. *Int. J. Solids Struct.* **2021**, *233*, 111204. [CrossRef]

315. Martins, J.M.P.; Andrade-Campos, A.; Thuillier, S. Calibration of anisotropic plasticity models using a biaxial test and the virtual fields method. *Int. J. Solids Struct.* **2019**, *172–173*, 21–37. [CrossRef]

316. Kim, J.H.; Barlat, F.; Pierron, F.; Lee, M.G. Determination of Anisotropic Plastic Constitutive Parameters Using the Virtual Fields Method. *Exp. Mech.* **2014**, *54*, 1189–1204. [CrossRef]

317. Zhang, Y.; Van Bael, A.; Andrade-Campos, A.; Coppieters, S. Parameter identifiability analysis: Mitigating the non-uniqueness issue in the inverse identification of an anisotropic yield function. *Int. J. Solids Struct.* **2022**, *243*, 111543. [CrossRef]

318. Martins, J.M.P.; Andrade-Campos, A.; Thuillier, S. Comparison of inverse identification strategies for constitutive mechanical models using full-field measurements. *Int. J. Mech. Sci.* **2018**, *145*, 330–345. [CrossRef]

319. Park, N.; Huh, H.; Yoon, J.W. Anisotropic fracture forming limit diagram considering non-directionality of the equi-biaxial fracture strain. *Int. J. Solids Struct.* **2018**, *151*, 181–194. [CrossRef]

320. Goodwin, G.M. Application of strain analysis to sheet metal forming problems in the press shop. *SAE Trans.* **1968**, *77*, 380–387.

321. Marciniak, Z.; Kuczyński, K. Limit strains in the processes of stretch-forming sheet metal. *Int. J. Mech. Sci.* **1967**, *9*, 609–620. [CrossRef]

322. Raghavan, K. A simple technique to generate in-plane forming limit curves and selected applications. *Metall. Mater. Trans. A* **1995**, *26*, 2075–2084. [CrossRef]

323. Zhang, S.; Leotoing, L.; Guines, D.; Thuillier, S. Potential of the cross biaxial test for anisotropy characterization based on heterogeneous strain field. *Exp. Mech.* **2015**, *55*, 817–835. [CrossRef]

324. Shao, Z.; Li, N.; Lin, J.; Dean, T. Development of a new biaxial testing system for generating forming limit diagrams for sheet metals under hot stamping conditions. *Exp. Mech.* **2016**, *56*, 1489–1500. [CrossRef]

325. Paul, S.K. Prediction of complete forming limit diagram from tensile properties of various steel sheets by a nonlinear regression based approach. *J. Manuf. Process.* **2016**, *23*, 192–200. [CrossRef]

326. Zecevic, M.; Roemer, T.J.; Knezevic, M.; Korkolis, Y.P.; Kinsey, B.L. Residual Ductility and Microstructural Evolution in Continuous-Bending-under-Tension of AA-6022-T4. *Materials* **2016**, *9*, 130. [CrossRef]

327. Tamimi, S.; Sivaswamy, G.; Siddiq, M.A.; Rahimi, S.; Leacock, A.; Blackwell, P. Mechanical response and microstructure evolution of commercially pure titanium subjected to repetitive bending under tension. *Mater. Des.* **2020**, *193*, 108814. [CrossRef]

328. Tamimi, S.; Sivaswamy, G.; Pirgazi, H.; Amirkhiz, B.S.; Moturu, S.; Siddiq, M.A.; Kockelmann, W.; Blackwell, P. A new route for developing ultrafine-grained Al alloy strips using repetitive bending under tension. *Mater. Des.* **2021**, *206*, 109750. [CrossRef]

329. Ha, J.; Mayer, S.; Feng, Z.; Matukhno, N.; Knezevic, M.; Kinsey, B.L. Inducing <111> texture in AA5182-O through continuous-bending-under-tension and recovery heat treatment processes to influence r-values. *CIRP Ann.* **2022**, *71*, 249–252. [CrossRef]

330. Laukonis, J.V.; Ghosh, A.K. Effects of strain path changes on the formability of sheet metals. *Metall. Mater. Trans. A.* **1978**, *9*, 1849–1856. [CrossRef]

331. Da Rocha, A.B.; Barlat, F.; Jalinier, J. Prediction of the forming limit diagrams of anisotropic sheets in linear and non-linear loading. *Mater. Sci. Eng.* **1985**, *68*, 151–164. [CrossRef]

332. Stoughton, T.B.; Zhu, X. Review of theoretical models of the strain-based FLD and their relevance to the stress-based FLD. *Int. J. Plast.* **2004**, *20*, 1463–1486. [CrossRef]

333. Kleemola, H.J.; Pelkkikangas, M.T. Effect of predeformation and strain path on the forming limits of steel, copper and brass. *Sheet Metal Industries.* **1977**, *64*, 591–599.

334. Arrieux, R.; Bedrin, C.; Boivin, M. Determination of an intrinsic forming limit stress diagram for isotropic metal sheets. In Proceedings of the 12th Biennial Congress of the IDDRG, Legian Bali, Bali, Indonesia, 15 August–5 September 2021; pp. 61–71.

335. Stoughton, T.B.; Yoon, J.W. Path independent forming limits in strain and stress spaces. *Int. J. Solids Struct.* **2012**, *49*, 3616–3625. [CrossRef]

336. Hsu, E.; Carsley, J.E.; Verma, R. Development of forming limit diagrams of aluminum and magnesium sheet alloys at elevated temperatures. *J. Mater. Eng. Perform.* **2008**, *17*, 288–296. [CrossRef]

337. Zhang, R.; Shao, Z.; Lin, J. A review on modelling techniques for formability prediction of sheet metal forming. *Int. J. Lightweight Mater. Manuf.* **2018**, *1*, 115–125. [CrossRef]

338. Aretz, H. Numerical analysis of diffuse and localized necking in orthotropic sheet metals. *Int. J. Plast.* **2007**, *23*, 798–840. [CrossRef]

339. Hosford, W.F.; Duncan, J.L. Sheet metal forming: A review. *JOM* **1999**, *51*, 39–44. [CrossRef]

340. Banabic, D.; Barlat, F.; Cazacu, O.; Kuwabara, T. Advances in anisotropy and formability. *Int. J. Mater. Form.* **2010**, *3*, 165–189. [CrossRef]

341. Ozturk, F.; Dilmec, M.; Turkoz, M.; Ece, R.E.; Halkaci, H.S. Grid marking and measurement methods for sheet metal formability. In Proceedings of the 5th International Conference and Exhibition on Design and Production of MACHINES and DIES/MOLDS, Kusadasi, Turkey, 18–21 June 2009; pp. 41–49.

342. Bandyopadhyay, K.; Basak, S.; Panda, S.; Saha, P. Use of stress based forming limit diagram to predict formability in two-stage forming of tailor welded blanks. *Mater. Des.* **2015**, *67*, 558–570. [CrossRef]

343. Sajun Prasad, K.; Panda, S.K.; Kar, S.K.; Sen, M.; Murty, S.; Sharma, S.C. Microstructures, forming limit and failure analyses of inconel 718 sheets for fabrication of aerospace components. *J. Mater. Eng. Perform.* **2017**, *26*, 1513–1530. [CrossRef]

344. Omar, A.; Harisankar, K.; Tewari, A.; Narasimhan, K. Study of fracture behaviour and strain path during tube hydrforming process. In *Journal of Physics: Conference Series*; IOP Publishing: Bristol, England, 2016; p. 032105.

345. Bhargava, M.; Tewari, A.; Mishra, S.K. Forming limit diagram of Advanced High Strength Steels (AHSS) based on strain-path diagram. *Mater. Des.* **2015**, *85*, 149–155. [CrossRef]

346. Sutton, M.A.; Orteu, J.J.; Schreier, H. *Image Correlation for Shape, Motion and Deformation Measurements: Basic Concepts, Theory and Applications*; Springer: New York, NY, USA, 2009. [CrossRef]

347. Khoo, S.-W.; Karuppanan, S.; Tan, C.-S. A review of surface deformation and strain measurement using two-dimensional digital image correlation. *Metrol. Meas. Syst.* **2016**, *23*, 461–480. [CrossRef]

348. McCormick, N.; Lord, J. Digital image correlation. *Mater. Today* **2010**, *13*, 52–54. [CrossRef]

349. Erichsen, A. A new test for thin sheets. *Stahl Und Eisen* **1914**, *34*, 879–882.

350. Olsen, T. Machines for ductility testing. *Proceeding Am. Soc. Mater.* **1920**, *20*, 398–403.

351. Hecker, S.S. A cup test for assessing stretchability. *METALS ENGNG QUART.; U.S.A.; DA* **1974**, *14*, 30–36.

352. Kotkunde, N.; Srinivasan, S.; Krishna, G.; Gupta, A.K.; Singh, S.K. Influence of material models on theoretical forming limit diagram prediction for Ti–6Al–4V alloy under warm condition. *Trans. Nonferrous Met. Soc. China* **2016**, *26*, 736–746. [CrossRef]

353. Jovignot, C. Method and testing device for the study the fracture of the sheet metals. *Rev. De Metall.* **1930**, *27*, 287–291.

354. Nakazima, K.; Kikuma, T.; Hasuka, K. *Study on the Formability of Steel Sheets*; Yamata Technical Report, No. 264; Scientific Research Publishing: Wuhan, China, 1968; pp. 8517–8530.

355. *ASTM E2218-15*; Standard Test Method for Determining Forming Limit Curves. ASTM International: West Conshohocken, PA, USA, 2015.

356. *ISO 12004-2*; Metallic Materials–Sheet and Strip–Determination of Forming-Limit Curves–Part 2: Determination of Forming-Limit Curves in the Laboratory. ISO: Geneva, Switzerland, 2008.

357. Zhang, L.; Min, J.Y.; Carsley, J.E.; Stoughton, T.B.; Lin, J.P. Experimental and theoretical investigation on the role of friction in Nakazima testing. *Int. J. Mech. Sci.* **2017**, *133*, 217–226. [CrossRef]

358. Basak, S.; Prasad, K.S.; Sidpara, A.M.; Panda, S.K. Single point incremental forming of AA6061 thin sheet: Calibration of ductile fracture models incorporating anisotropy and post forming analyses. *Int. J. Mater. Form.* **2019**, *12*, 623–642. [CrossRef]

359. Ma, B.L.; Wan, M.; Cai, Z.Y.; Yuan, W.N.; Li, C.; Wu, X.D.; Liu, W. Investigation on the forming limits of 5754-O aluminum alloy sheet with the numerical Marciniak–Kuczynski approach. *Int. J. Mech. Sci.* **2018**, *142–143*, 420–431. [CrossRef]

360. Volk, W.; Groche, P.; Brosius, A.; Ghiotti, A.; Kinsey, B.L.; Liewald, M.; Madej, L.; Min, J.; Yanagimoto, J. Models and modelling for process limits in metal forming. *CIRP Ann.* **2019**, *68*, 775–798. [CrossRef]

361. Min, J.; Stoughton, T.B.; Carsley, J.E.; Lin, J. Comparison of DIC methods of determining forming limit strains. *Procedia Manuf.* **2017**, *7*, 668–674. [CrossRef]

362. Zhang, L.; Lin, J.; Sun, L.; Wang, C.; Wang, L. *A New Method for Determination of Forming Limit Diagram Based on Digital Image Correlation*; SAE Technical Paper: Detroit, MI, USA, 2013.

363. Volk, W.; Hora, P. New algorithm for a robust user-independent evaluation of beginning instability for the experimental FLC determination. *Int. J. Mater. Form.* **2010**, *4*, 339–346. [CrossRef]

364. Merklein, M.; Kuppert, A.; Geiger, M. Time dependent determination of forming limit diagrams. *CIRP Ann.* **2010**, *59*, 295–298. [CrossRef]

365. Hotz, W.; Merklein, M.; Kuppert, A.; Friebe, H.; Klein, M. Time dependent FLC determination comparison of different algorithms to detect the onset of unstable necking before fracture. In *Key Engineering Materials*; Trans Tech Publications Ltd: Zurich, Switzerland, 2013; pp. 397–404.

366. Li, J.; Carsley, J.E.; Stoughton, T.B.; Hector Jr, L.G.; Hu, S.J. Forming limit analysis for two-stage forming of 5182-O aluminum sheet with intermediate annealing. *Int. J. Plast.* **2013**, *45*, 21–43. [CrossRef]

367. Wang, K.; Carsley, J.E.; He, B.; Li, J.; Zhang, L. Measuring forming limit strains with digital image correlation analysis. *J. Mater. Process. Technol.* **2014**, *214*, 1120–1130. [CrossRef]

368. Martínez-Donaire, A.; García-Lomas, F.; Vallellano, C. New approaches to detect the onset of localised necking in sheets under through-thickness strain gradients. *Mater. Des.* **2014**, *57*, 135–145. [CrossRef]

369. Min, J.; Stoughton, T.; Carsley, J.; Lin, J. A Method of Detecting the Onset of Localized Necking Based on Surface Geometry Measurements. *Exp. Mech.* **2017**, *57*, 521–535. [CrossRef]

370. Min, J.; Stoughton, T.B.; Carsley, J.E.; Lin, J. An improved curvature method of detecting the onset of localized necking in Marciniak tests and its extension to Nakazima tests. *Int. J. Mech. Sci.* **2017**, *123*, 238–252. [CrossRef]

371. Basak, S.; Panda, S.K. Implementation of Yld96 anisotropy plasticity theory for estimation of polar effective plastic strain based failure limit of pre-strained thin steels. *Thin-Walled Struct.* **2018**, *126*, 26–37. [CrossRef]

372. Hill, R. On discontinuous plastic states, with special reference to localized necking in thin sheets. *J. Mech. Phys. Solids* **1952**, *1*, 19–30. [CrossRef]

373. Swift, H.W. Plastic instability under plane stress. *J. Mech. Phys. Solids* **1952**, *1*, 1–18. [CrossRef]

374. Aretz, H. An extension of Hill's localized necking model. *Int. J. Eng. Sci.* **2010**, *48*, 312–331. [CrossRef]

375. Sing, W.; Rao, K. Prediction of sheet-metal formability using tensile-test results. *J. Mater. Process. Technol.* **1993**, *37*, 37–51. [CrossRef]

376. Chung, K.; Ahn, K.; Yoo, D.-H.; Chung, K.-H.; Seo, M.-H.; Park, S.-H. Formability of TWIP (twinning induced plasticity) automotive sheets. *Int. J. Plast.* **2011**, *27*, 52–81. [CrossRef]

377. Hora, P.; Tong, L.; Reissner, J. A prediction method for ductile sheet metal failure in FE-simulation. In *NUMISHEET*; Ohio State University: Colombus, OH, USA, 1996; pp. 252–256.

378. Hora, P.; Tong, L.; Berisha, B. Modified maximum force criterion, a model for the theoretical prediction of forming limit curves. *Int. J. Mater. Form.* **2013**, *6*, 267–279. [CrossRef]

379. Hora, P.; Merklein, M.; Tong, L.; Lechler, J. Numerical and experimental evaluation of thermal dependent FLC (FLC-T). In Proceedings of the Int. Deep Drawing Research Group IDDRG, Tisza, M.(Edtr.): Proceedings of the IDDRG 2007 Conference, Gyor, Hungary, 21–23 May 2007; pp. 23–30.

380. Stören, S.; Rice, J. Localized necking in thin sheets. *J. Mech. Phys. Solids* **1975**, *23*, 421–441. [CrossRef]

381. Hashiguchi, K.; Protasov, A. Localized necking analysis by the subloading surface model with tangential-strain rate and anisotropy. *Int. J. Plast.* **2004**, *20*, 1909–1930. [CrossRef]

382. Zhu, X.; Weinmann, K.; Chandra, A. A unified bifurcation analysis of sheet metal forming limits. *J. Eng. Mater. Technol.* **2001**, *123*, 329–333. [CrossRef]

383. Min, J.Y.; Lin, J.P.; Li, J.Y.; Bao, W.H. Investigation on hot forming limits of high strength steel 22MnB5. *Comput. Mater. Sci* **2010**, *49*, 326–332. [CrossRef]

384. Hutchinson, J.; Neale, K. Sheet necking-II. Time-independent behavior. In *Mechanics of Sheet Metal Forming*; Springer: Berlin, Germany, 1978; pp. 127–153. [CrossRef]

385. Hutchinson, J.; Neale, K.; Needleman, A. Sheet necking—I. Validity of plane stress assumptions of the long-wavelength approximation. In *Mechanics of Sheet Metal Forming*; Springer: Berlin, Germany, 1978; pp. 111–126. [CrossRef]

386. Kotkunde, N.; Krishna, G.; Shenoy, S.K.; Gupta, A.K.; Singh, S.K. Experimental and theoretical investigation of forming limit diagram for Ti-6Al-4 V alloy at warm condition. *Int. J. Mater. Form.* **2017**, *10*, 255–266. [CrossRef]

387. Date, P.; Padmanabhan, K. On the prediction of the forming-limit diagram of sheet metals. *Int. J. Mech. Sci.* **1992**, *34*, 363–374. [CrossRef]

388. Needleman, A.; Triantafyllidis, N. Void growth and local necking in biaxially stretched sheets. *J. Eng. Mater. Technol.* **1978**, *100*, 164–169. [CrossRef]

389. Melander, A. A new model of the forming limit diagram applied to experiments on four copper-base alloys. *Mater. Sci. Eng.* **1983**, *58*, 63–88. [CrossRef]

390. Parmar, A.; Mellor, P.; Chakrabarty, J. A new model for the prediction of instability and limit strains in thin sheet metal. *Int. J. Mech. Sci.* **1977**, *19*, 389–398. [CrossRef]

391. Wang, Y.; Majlessi, S.; Ning, J.; Aifantis, E. The strain gradient approach for deformation localization and forming limit diagrams. *J. Mech. Behav. Mater.* **1996**, *7*, 265–278. [CrossRef]

392. Hashemi, R.; Assempour, A.; Abad, E.M.K. Implementation of the forming limit stress diagram to obtain suitable load path in tube hydroforming considering M–K model. *Mater. Des.* **2009**, *30*, 3545–3553. [CrossRef]

393. Bong, H.J.; Barlat, F.; Lee, M.G.; Ahn, D.C. The forming limit diagram of ferritic stainless steel sheets: Experiments and modeling. *Int. J. Mech. Sci.* **2012**, *64*, 1–10. [CrossRef]

394. Chan, K.; Koss, D.; Ghosh, A. Localized necking of sheet at negative minor strains. *Metall. Trans. A* **1984**, *15*, 323–329. [CrossRef]

395. Panich, S.; Barlat, F.; Uthaisangsuk, V.; Suranuntchai, S.; Jirathearanat, S. Experimental and theoretical formability analysis using strain and stress based forming limit diagram for advanced high strength steels. *Mater. Des.* **2013**, *51*, 756–766. [CrossRef]

396. Abedrabbo, N.; Pourboghrat, F.; Carsley, J. Forming of aluminum alloys at elevated temperatures–Part 2: Numerical modeling and experimental verification. *Int. J. Plast.* **2006**, *22*, 342–373. [CrossRef]

397. Nicolaou, P.; Semiatin, S.; Ghosh, A. An analysis of the effect of cavity nucleation rate and cavity coalescence on the tensile behavior of superplastic materials. *Metall. Mater. Trans. A* **2000**, *31*, 1425–1434. [CrossRef]

398. Lin, J. *Fundamentals of Materials Modelling for Metals Processing Technologies: Theories and Applications*; World Scientific Publishing Company: Toh Tuck, Singapore, 2015.

399. Lin, J.; Mohamed, M.; Balint, D.; Dean, T. The development of continuum damage mechanics-based theories for predicting forming limit diagrams for hot stamping applications. *Int. J. Damage Mech.* **2014**, *23*, 684–701. [CrossRef]

400. Shao, Z.; Li, N.; Lin, J.; Dean, T. Formability evaluation for sheet metals under hot stamping conditions by a novel biaxial testing system and a new materials model. *Int. J. Mech. Sci.* **2017**, *120*, 149–158. [CrossRef]

401. Brunet, M.; Morestin, F. Experimental and analytical necking studies of anisotropic sheet metals. *J. Mater. Process. Technol.* **2001**, *112*, 214–226. [CrossRef]

402. Chen, Z.; Dong, X. The GTN damage model based on Hill'48 anisotropic yield criterion and its application in sheet metal forming. *Comput. Mater. Sci* **2009**, *44*, 1013–1021. [CrossRef]

403. Chow, C.; Yu, L.; Demeri, M. A unified damage approach for predicting forming limit diagrams. *J. Eng. Mater. Technol.* **1997**, *119*, 346–353. [CrossRef]

404. Chow, C.; Yang, X. Prediction of the forming limit diagram on the basis of the damage criterion under non-proportional loading. *Proc. Inst. Mech. Eng. Part C: J. Mech. Eng. Sci.* **2001**, *215*, 405–414. [CrossRef]

405. Chow, C.; Yang, X.; Chu, E. Prediction of forming limit diagram based on damage coupled kinematic-isotropic hardening model under nonproportional loading. *J. Eng. Mater. Technol.* **2002**, *124*, 259–265. [CrossRef]

406. Keeler, S.; Brazier, W.G. Relationship between laboratory material characterization and press-shop formability. *Microalloying.* **1975**, *75*, 517–530.

407. Bleck, W.; Deng, Z.; Papamantellos, K.; Gusek, C.O. A comparative study of the forming-limit diagram models for sheet steels. *J. Mater. Process. Technol.* **1998**, *83*, 223–230. [CrossRef]

408. Slota, J.; Spišák, E. Comparison of the forming-limit diagram (FLD) models for drawing quality (DQ) steel sheets. *Metalurgija* **2005**, *44*, 249–253.

409. Djavanroodi, F.; Derogar, A. Experimental and numerical evaluation of forming limit diagram for Ti6Al4V titanium and Al6061-T6 aluminum alloys sheets. *Mater. Des.* **2010**, *31*, 4866–4875. [CrossRef]

410. Jones, S.; Gillis, P. An analysis of biaxial stretching of a flat sheet. *Metall. Trans. A* **1984**, *15*, 133–138. [CrossRef]

411. Choi, W.; Gillis, P.P.; Jones, S. Calculation of the forming limit diagram. *Metall. Trans. A* **1989**, *20*, 1975–1987. [CrossRef]

412. Elangovan, K.; Narayanan, C.S.; Narayanasamy, R. Modelling of forming limit diagram of perforated commercial pure aluminium sheets using artificial neural network. *Comput. Mater. Sci* **2010**, *47*, 1072–1078. [CrossRef]

413. Kotkunde, N.; Deole, A.D.; Gupta, A.K. Prediction of forming limit diagram for Ti-6Al-4V alloy using artificial neural network. *Procedia Mater. Sci.* **2014**, *6*, 341–346. [CrossRef]

414. Wu, P.; Neale, K.; Van der Giessen, E. On crystal plasticity FLD analysis. *Proc. R. Soc. London. Ser. A: Math. Phys. Eng. Sci.* **1997**, *453*, 1831–1848. [CrossRef]

415. Savoie, J.; Jain, M.; Carr, A.; Wu, P.; Neale, K.; Zhou, Y.; Jonas, J. Predictions of forming limit diagrams using crystal plasticity models. *Mater. Sci. Eng. A* **1998**, *257*, 128–133. [CrossRef]

416. McGinty, R.D.; McDowell, D.L. Application of multiscale crystal plasticity models to forming limit diagrams. *J. Eng. Mater. Technol.* **2004**, *126*, 285–291. [CrossRef]

417. Inal, K.; Neale, K.; Aboutajeddine, A. Forming limit comparisons for FCC and BCC sheets. *Int. J. Plast.* **2005**, *21*, 1255–1266. [CrossRef]

418. Neil, C.J.; Agnew, S.R. Crystal plasticity-based forming limit prediction for non-cubic metals: Application to Mg alloy AZ31B. *Int. J. Plast.* **2009**, *25*, 379–398. [CrossRef]

419. Wang, H.; Wu, P.; Boyle, K.; Neale, K. On crystal plasticity formability analysis for magnesium alloy sheets. *Int. J. Solids Struct.* **2011**, *48*, 1000–1010. [CrossRef]

420. Kim, J.H.; Lee, M.G.; Kang, J.H.; Oh, C.S.; Barlat, F. Crystal plasticity finite element analysis of ferritic stainless steel for sheet formability prediction. *Int. J. Plast.* **2017**, *93*, 26–45. [CrossRef]

421. Ragab, A.; Saleh, C.A. Effect of void growth on predicting forming limit strains for planar isotropic sheet metals. *Mech. Mater.* **2000**, *32*, 71–84. [CrossRef]

422. Bong, H.J. Surface roughening of ferritic stainless steel sheets and its application to the forming limit diagram. *Steel Res. Int. Speciai Ed.* **2012**, *83*, 975–978. [CrossRef]

423. Karafillis, A.; Boyce, M. A general anisotropic yield criterion using bounds and a transformation weighting tensor. *J. Mech. Phys. Solids* **1993**, *41*, 1859–1886. [CrossRef]

424. Barlat, F.; Brem, J.; Lege, D.; Chung, K. Characterization of the formability for aluminum alloy and steel sheets. In *Studies in Applied Mechanics*; Elsevier: Amsterdam, The Netherlands, 1997; Volume 45, pp. 265–272.

425. Bong, H.J.; Barlat, F.; Ahn, D.C.; Kim, H.Y.; Lee, M.G. Formability of austenitic and ferritic stainless steels at warm forming temperature. *Int. J. Mech. Sci.* **2013**, *75*, 94–109. [CrossRef]

426. Nguyen, N.-T.; Seo, O.S.; Lee, C.A.; Lee, M.-G.; Kim, J.-h.; Kim, H.Y. Mechanical behavior of AZ31B Mg alloy sheets under monotonic and cyclic loadings at room and moderately elevated temperatures. *Materials* **2014**, *7*, 1271–1295. [CrossRef] [PubMed]

427. Srivastava, A.; Bower, A.F.; Hector, L.G.; Carsley, J.E.; Zhang, L.; Abu-Farha, F. A multiscale approach to modeling formability of dual-phase steels. *Modell. Simul. Mater. Sci. Eng.* **2016**, *24*, 025011. [CrossRef]

428. Nagra, J.S.; Brahme, A.; Mishra, R.; Lebensohn, R.A.; Inal, K. An efficient full-field crystal plasticity-based M–K framework to study the effect of 3D microstructural features on the formability of polycrystalline materials. *Modell. Simul. Mater. Sci. Eng.* **2018**, *26*, 075002. [CrossRef]

429. Wu, P.; MacEwen, S.; Lloyd, D.; Neale, K. A mesoscopic approach for predicting sheet metal formability. *Modell. Simul. Mater. Sci. Eng.* **2004**, *12*, 511. [CrossRef]

430. Zhou, Y.; Neale, K. Predictions of forming limit diagrams using a rate-sensitive crystal plasticity model. *Int. J. Mech. Sci.* **1995**, *37*, 1–20. [CrossRef]

431. Yoshida, K.; Ishizaka, T.; Kuroda, M.; Ikawa, S. The effects of texture on formability of aluminum alloy sheets. *Acta Mater.* **2007**, *55*, 4499–4506. [CrossRef]

432. Tadano, Y.; Yoshida, K.; Kuroda, M. Plastic flow localization analysis of heterogeneous materials using homogenization-based finite element method. *Int. J. Mech. Sci.* **2013**, *72*, 63–74. [CrossRef]

433. Guedes, J.; Kikuchi, N. Preprocessing and postprocessing for materials based on the homogenization method with adaptive finite element methods. *Comput. Methods Appl. Mech. Eng.* **1990**, *83*, 143–198. [CrossRef]

434. Hajian, M.; Assempour, A. Experimental and numerical determination of forming limit diagram for 1010 steel sheet: A crystal plasticity approach. *Int. J. Adv. Manuf. Technol.* **2015**, *76*, 1757–1767. [CrossRef]

435. Hajian, M.; Assempour, A.; Akbarzadeh, A. Experimental investigation and crystal plasticity–based prediction of AA1050 sheet formability. *Proc. Inst. Mech. Eng. Part B: J. Eng. Manuf.* **2017**, *231*, 1341–1349. [CrossRef]

436. Mohammed, B.; Park, T.; Kim, H.; Pourboghrat, F.; Esmaeilpour, R. The forming limit curve for multiphase advanced high strength steels based on crystal plasticity finite element modeling. *Mater. Sci. Eng. A* **2018**, *725*, 250–266. [CrossRef]

437. Bong, H.J.; Lee, J.; Hu, X.; Sun, X.; Lee, M.-G. Predicting forming limit diagrams for magnesium alloys using crystal plasticity finite elements. *Int. J. Plast.* **2020**, *126*, 102630. [CrossRef]

438. Gupta, A.; Bettaieb, M.B.; Abed-Meraim, F.; Kalidindi, S.R. Computationally efficient predictions of crystal plasticity based forming limit diagrams using a spectral database. *Int. J. Plast.* **2018**, *103*, 168–187. [CrossRef]

439. Kalidindi, S.R. Data science and cyberinfrastructure: Critical enablers for accelerated development of hierarchical materials. *Int. Mater. Rev.* **2015**, *60*, 150–168. [CrossRef]

440. Alharbi, H.F.; Kalidindi, S.R. Crystal plasticity finite element simulations using a database of discrete Fourier transforms. *Int. J. Plast.* **2015**, *66*, 71–84. [CrossRef]

441. Joseph, D.S.; Chakraborty, P.; Ghosh, S. Wavelet transformation based multi-time scaling method for crystal plasticity FE simulations under cyclic loading. *Comput. Methods Appl. Mech. Eng.* **2010**, *199*, 2177–2194. [CrossRef]

442. Chakraborty, P.; Joseph, D.S.; Ghosh, S. Wavelet transformation based multi-time scale crystal plasticity FEM for cyclic deformation in titanium alloys under dwell load. *Finite Elem. Anal. Des.* **2011**, *47*, 610–618. [CrossRef]

443. Eghtesad, A.; Germaschewski, K.; Lebensohn, R.A.; Knezevic, M. A multi-GPU implementation of a full-field crystal plasticity solver for efficient modeling of high-resolution microstructures. *Comput. Phys. Commun.* **2020**, *254*, 107231. [CrossRef]

444. Mellbin, Y.; Hallberg, H.; Ristinmaa, M. Accelerating crystal plasticity simulations using GPU multiprocessors. *Int. J. Numer. Methods Eng.* **2014**, *100*, 111–135. [CrossRef]

445. Inal, A.K. *Numerical Simulation of Sheet Metal Forming Processes and Localized Deformation Phenomena for FCC Polycrystals= Simulation Numérique de la Mise en Forme des Métaux et les Phénomènes de Localisation pour les Polycristaux CFC*; National Library of Canada: Ottawa, ON, Canada, 2003.

446. Chollet, F. *Deep Learning mit Python und Keras: Das Praxis-Handbuch vom Entwickler der Keras-Bibliothek*; MITP-Verlags GmbH & Co. K: Frechen, Germany, 2018.

447. Ali, U.; Muhammad, W.; Brahme, A.; Skiba, O.; Inal, K. Application of artificial neural networks in micromechanics for polycrystalline metals. *Int. J. Plast.* **2019**, *120*, 205–219. [CrossRef]

448. Yuan, M.; Paradiso, S.; Meredig, B.; Niezgoda, S.R. Machine learning–based reduce order crystal plasticity modeling for ICME applications. *Integr. Mater. Manuf. Innov.* **2018**, *7*, 214–230. [CrossRef]

449. Miyazawa, Y.; Briffod, F.; Shiraiwa, T.; Enoki, M. Prediction of cyclic stress–strain property of steels by crystal plasticity simulations and machine learning. *Materials* **2019**, *12*, 3668. [CrossRef]

450. Pandey, A.; Pokharel, R. Machine learning based surrogate modeling approach for mapping crystal deformation in three dimensions. *Scr. Mater.* **2021**, *193*, 1–5. [CrossRef]

451. Acar, P. Machine learning reinforced crystal plasticity modeling under experimental uncertainty. *AIAA J.* **2020**, *58*, 3569–3576. [CrossRef]

452. Ibragimova, O.; Brahme, A.; Muhammad, W.; Connolly, D.; Lévesque, J.; Inal, K. A convolutional neural network based crystal plasticity finite element framework to predict localised deformation in metals. *Int. J. Plast.* **2022**, *157*, 103374. [CrossRef]